

2016-01-01

Characterization Of High Intensity Turbulent Flows Through Time Resolved Particle Image Velocimetry In A Backward Facing Step Combustor

Martin De La Torre

University of Texas at El Paso, made2@miners.utep.edu

Follow this and additional works at: https://digitalcommons.utep.edu/open_etd



Part of the [Engineering Commons](#)

Recommended Citation

De La Torre, Martin, "Characterization Of High Intensity Turbulent Flows Through Time Resolved Particle Image Velocimetry In A Backward Facing Step Combustor" (2016). *Open Access Theses & Dissertations*. 634.

https://digitalcommons.utep.edu/open_etd/634

This is brought to you for free and open access by DigitalCommons@UTEP. It has been accepted for inclusion in Open Access Theses & Dissertations by an authorized administrator of DigitalCommons@UTEP. For more information, please contact lweber@utep.edu.

CHARACTERIZATION OF HIGH INTENSITY TURBULENT FLOWS
THROUGH TIME RESOLVED PARTICLE IMAGE VELOCIMETRY IN A
BACKWARD FACING STEP COMBUSTOR

MARTIN ALEJANDRO DE LA TORRE
Doctoral Program in Mechanical Engineering

APPROVED:

Ahsan R. Choudhuri, Ph.D., Chair

Norman D. Love, Ph.D., Co-Chair

Evgeny Shafirovich, Ph.D.

Chunqiang Li, Ph.D.

Charles Ambler, Ph.D.
Dean of the Graduate School

Copyright ©

by

Martin de la Torre

2016

Dedication

To my family, and my patient wife who've been there for me through all the good and the bad.

CHARACTERIZATION OF HIGH INTENSITY TURBULENT FLOWS
THROUGH TIME RESOLVED PARTICLE IMAGE VELOCIMETRY IN A
BACKWARD FACING STEP COMBUSTOR

by

MARTIN ALEJANDRO DE LA TORRE, MSME

DISSERTATION

Presented to the Faculty of the Graduate School of
The University of Texas at El Paso
in Partial Fulfillment
of the Requirements
for the Degree of

DOCTOR OF PHILOSOPHY

Department of Mechanical Engineering
THE UNIVERSITY OF TEXAS AT EL PASO

December 2016

Acknowledgements

I would like to extend my deepest gratitude to the University of Texas at El Paso's Mechanical Engineering faculty and staff for their support, guidance, and mentorship provided throughout my Ph.D. experience. I would like to give special thanks to Dr. Choudhuri and Dr. Norman Love for their guidance, mentorship, and advice, that led to the completion of the presented work, to my colleague and friend Arturo Acosta-Zamora for helping me in the completion of the experimentations needed to generate the presented results, and to the Center for Space Exploration and Technology Research's (cSETR) faculty and staff. I would also like to acknowledge Marco Quiroz and Arif Hossain for their contributions in the design of the experimental setup. Financial support was provided by NASA under award No(s) NNX09AV09A and W911NF-13-1-0156 via the Army Research Office (ARO).

Abstract

The fundamental understanding of turbulent premixed combustion has taken place as one of the major research topics of interest in industry thanks to advancements in kHz level laser diagnostics such as in Particle Image Velocimetry (PIV) and Planar Laser Induced Fluorescence (PLIF). Because of said advancements in this technology researchers and the scientific community are now able to expand their understanding of flame studies at high turbulence conditions to acquire a better understanding, and improve models used in turbine design, scram/ram jets, rocket engines, and emissions control. This surge of new technologies has made this topic a high priority one for The Air Force Office of Scientific Research (AFSOR). While there have been many studies aiming to provide useful data in this research field, there are still many uncertainties associated with the fundamentals of turbulent pre-mixed combustion, especially at the conditions investigated in this study ($Re_T \gg 1$, $Da \geq 1$, $Ka > 1$, $u/S_L \gg 1$, $\delta_L/\eta > 1$). As of today designers rely on the design-test-modify method, which is not only time consuming but also expensive. It is because of this that the research community is searching for a reliable and effective numerical model in order to design next generation combustors. The models used in this application need a detailed experimental analysis of the fundamentals of turbulent flame structure and a wide range of experimental data in order to be valid the design models, but few studies at these flame conditions are available making this the main drive for this work. The main goal of this study is to establish the limits and capabilities to reach different flame regime boundaries under Mach Number (M) $> .3$ and (Re_t) $> 10^3$ of CH_4 – air premixed flames, of a backward facing step combustor. This study provides the global characteristics of a backward facing step high intensity turbulent flows through high speed flow visualization. It also determines the capability of the experimental setup to reach the thickened flame regime, while generating the components of the flow's turbulent intensity and

turbulent kinetic energy.

Table of Contents

Acknowledgements	v
Abstract	vi
Table of Contents	viii
List of Tables	x
List of Figures	xi
Chapter 1: Introduction	1
1.1 Objective	2
Chapter 2: Theory and Literature Review	4
2.1 Flow Over Backward Facing Step	4
2.2 Turbulent Flow	6
2.2.1 Statistical Description	7
2.2.2 Turbulent Intensity	9
2.2.3 Turbulent Kinetic Energy	9
2.2.4 Turbulent Length Scale	10
2.2.5 Grid Induced Turbulence	11
2.3 Optical Diagnostics	13
2.3.1 Particle Imaging Velocity (PIV)	14
2.3.2 Planar Laser Induced Fluorescence (PLIF)	17
2.4 Combustion	22
2.4.1 Premixed Laminar Flames	25
2.4.2 Laminar Flame Speed (S_L)	26
2.4.3 Laminar Flame Thickness	28
2.5 Flame Regimes	28
2.5.1 Wrinkled Flame Regime	31
2.5.2 Corrugated Flame Regime	31
2.5.3 Thickened Flame Regime	31
2.5.4 Thickened Flame Regime	32

2.6 Laser Diagnostics in Turbulent Combustion Studies.....	33
Chapter 3: Experimental Setup	37
3.1 System description	37
3.2 Exhaust Design	43
3.4 Combustion Chamber Cooling	45
3.5 Control System.....	48
3.8 Test Setup Summary	52
Chapter 4: Methodology	54
4.1 Particle Image Velocimetry (PIV)	61
4.1.1 Seeding Particles	61
4.1.2 Laser Type	62
4.1.3 Image Acquisition.....	62
4.1.4 Cross-Correlation.....	63
4.2 PIV Post Processing Techniques	64
4.2.1 Image Balancing	64
4.2.2 Image Masking.....	65
4.2.3 Adaptive PIV	66
Chapter 5: Results and Discussion.....	77
5.1 Flow Characterization.....	77
Chapter 6: Conclusions and Future Investigation.....	97
6.1 Concluding Remarks.....	97
References.....	100
Vita	107

List of Tables

Table 2.1: Flow regimes and their Reynolds number range	6
Table 2.2 A summary of relevant research to the presented work regarding laser diagnostics....	34
Table 3.1 System Requirements	37
Table 3.2: Components in combustor and their factor of safety	38
Table 3.3: Comparison between theoretical and CFD results.....	45
Table 3.2: DAC controlled instrumentation.....	49
Table 3.3: A summarization of the subsystems that make up the high turbulent intensity system	52
Table 4.1: Test matrix utilized for the presented work.....	55
Table 4.2: Blockage ratio (BR), and hole diameter (HD) of the tested perforated plates	55
Table 5.1: Summarized flow data. Grid 1 through 4 from top to bottom.	95
Table 5.2: Grid parameters on the Borghi-Peters diagram	95

List of Figures

Figure 2.1: Schematic of different separation zones in a backward facing step [2]	5
Figure 2.2: CFD result validation with experimental data [5]	5
Figure 2.3: Variation in velocity during turbulent flow [8]	7
Figure 2.4: Average and fluctuation components of an instantaneous velocity measurement [8] .	8
Figure 2.5: The “energy cascade” proposed by Kolmogorov [10].....	10
Figure 2.6: Statistically homogeneous isotropic turbulence [12]	12
Figure 2.7: Visual representation of grid induced turbulence in a duct [12]	13
Figure 2.8: Schematic of experimental arrangement for PIV [19].	15
Figure 2.9: (a) Fluorescence technique basic principle. (b) Energy Distribution	18
Figure 2.10: 1D radical pool of a methane/air flame with normalized molar fraction with respect to the max of each species	20
Figure 2.11: Effects of unburnt gas temperature, equivalence ratio, and pressure on different species concentrations.....	21
Figure 2.12: Concentration and temperature profile of a) premixed, b) diffusion flames.....	23
Figure 2.13: Simplified hydrocarbon/air oxidation mechanism	25
Figure 2.14: Temperature and species concentration profiles of a premixed laminar flame [34].	26
Figure 2.15: Laminar flame speed of methane/air at 298K and 1 atm pressure [39]	27
Figure 2.16: Illustration of the flame structure where δx is the flame thickness, defined by the steepest tangent to the temperature profile [47].....	28
Figure 2.17: Flame regime diagram by Borghi and modified by Peters.....	30
Figure 2.18: Different flame regimes and the graphical illustrations of flame front characteristics [51].....	30

Figure 2.19: a) Thickened flame regime on the Borghi diagram.....	32
Figure 2.20: Distributed Flame Regime (Broken Reaction Zones) location on the Borghi-Peters diagram	33
Figure 3.1: Exploded model of the combustor subsystem and its components	39
Figure 3.2: Cross-sectional view of the combustor showing 2D plane used in simulations	39
Figure 3.3: Flow schematic of the combustion system and detailed pilot flame flow schematic.	41
Figure 3.4: Combustion chamber showing location of pilot flame	42
Figure 3.5: Coil wiring diagram.....	42
Figure 3.6: Initial conceptual model of exhaust section with spray nozzle diagram	43
Figure 3.7: Temperature contours in exhaust simulation.....	45
Figure 3.8: CAD model of heat exchanger and dynalene tank (left) and physical setup (right) ..	47
Figure 3.9: Additional schematic of heat exchanger used for cooling	47
Figure 3.10: Temperature vs time plots for critical thickness and largest quartz window	48
Figure 3.11: Main control box	50
Figure 3.12: Electrical schematic of main control box	50
Figure 3.13: LabVIEW control panel interface	51
Figure 3.14: DAQ assist block diagram.....	51
Figure 4.1: A simplified flow schematic of the presented work taking Figure 3.3 as a base line	54
Figure 4.2: PIV beam path into the combustor and raised laser head.....	56
Figure 4.3: PIV process.....	58
Figure 4.4: Sample image of a calibration target used to define the PIV scale factor	59
Figure 4.5: Sample image of the seeded flow with the mill metric scale displayed. Red line outlines the step location and white lines delineates the light sheet location.	60

Figure 4.6: High speed camera used for the presented work	63
Figure 4.7: Raw image, image balance map, and light balanced image	65
Figure 4.8: Masked raw seeded flow image for PIV analysis	66
Figure 4.9: Sample PIV vector map of Grid 1 at 12CFM 70psi	68
Figure 4.10: Sample turbulence intensity scalar map of Grid 1 at 12CFM 70psi	69
Figure 4.11: Sample PIV vorticity scalar map of Grid 1 at 12CFM 70psi	70
Figure 4.12: Sample image of the interrogation line on the vector statistics map.....	71
Figure 4.13: Sample plot of the interrogation line on the onset of the combustor step	72
Figure 4.14: Sample POD snapshot.....	73
Figure 4.15: Sample POD snapshot projection.....	74
Figure 4.16: Sample instantaneous velocity measurements	75
Figure 4.17: Location of the extract points	76
Figure 5.1: Vector map at 12, 25, and 50 CFM	78
Figure 5.2: Velocity vector field map at 12, 25, and 50 CFM,.....	79
Figure 5.3: Location of the interrogation line where the vector statistics are calculated (12, 25, 50 CFM).....	81
Figure 5.4: Velocity components found along the interrogation line (12, 25, 50 CFM)	82
Figure 5.5: u_{RMS} and v_{RMS} components at the interrogation line location (12 CFM).....	83
Figure 5.6: Turbulence intensity contour plot (12, 25, 50 CFM)	84
Figure 5.7: Turbulence intensity contour plot with modified scale (12, 25 CFM, Grid 1).....	86
Figure 5.8: Vorticity levels found on the interrogation line at the different flow conditions.....	88
Figure 5.9: Vorticity contour plot and location of interrogation line (12, 25, 50 CFM)	88
Figure 5.10: POD projection to velocity vector field (12 CFM)	90

Figure 5.11: POD projection to velocity vector field at the different flow conditions	91
Figure 5.12: $u(t)$ and $v(t)$ at an interrogation point at 12 CFM.....	92
Figure 5.13: $u(t)$ and $v(t)$ at an interrogation point at 25 CFM.....	92
Figure 5.14: $u(t)$ and $v(t)$ at an interrogation point at 50 CFM.....	93
Figure 5.15: TKE contour plots at the different flow conditions.....	94
Figure 5.16: Location of the different grids on the Borghi-Peters diagram.....	96

Chapter 1: Introduction

The fundamental understanding of turbulent premixed combustion has taken place as one of the major research topics of interest in the industry thanks to advancements in the kHz level laser diagnostics such as in Particle Image Velocimetry (PIV) and Planar Laser Induced Fluorescence (PLIF). Because of said advancements in this technology researchers and the scientific community are now able to expand their understanding of flame studies at high turbulence conditions to acquire a better understanding, and improve models used in turbine design, scram/ram jets, rocket engines, and emissions control. This surge of new technologies has made this topic a high priority one for The Army Research Office (ARO). While there have been many studies aiming to provide useful data in this research field, there are still many uncertainties associated with the fundamentals of turbulent pre-mixed combustion, especially at the conditions investigated in this study ($Re_T \gg 1$, $Da \geq 1$, $Ka > 1$, $u/S_L \gg 1$, $\delta_L/\eta > 1$). As of today designers rely on the design-test-modify method, which is not only time consuming but also expensive. It is because of this that the research community is searching for a reliable and effective numerical model in order to design next generation combustors. The models used in this application need a detailed experimental analysis of the fundamentals of turbulent flame structure and a wide range of experimental data in order to be valid the design models, but few studies at these flame conditions are available making this the main drive for this work.

The development of high repetition rate laser diagnostic techniques such as (PIV) and (LIF) enable the study of turbulent flow and turbulent combustion to a level that was not available before. Unlike other techniques readily available, these non-intrusive techniques provide a way to study high-speed flows with minimal disturbance to the flow field. A safe and reliable combustion

system capable of providing the desired high-turbulent flows needed has been developed in order to:

- Study global characteristics of backward-facing, step stabilized premixed flames in compressible and high turbulence flow using high speed flow visualization techniques

- Study flow-field and flame characteristics using Time Resolved Stereo Particle Image Velocimetry (TR-PIV) and OH/CH Planar Laser Induced Florescence (PLIF) Imaging

The main goal of this study is to utilize previous studies made and establish the limits of flame regime boundaries under Mach Number (M) $>.3$ and (Re_t) $> 10^3$ of CH_4 – air premixed flames. The study will also investigate flame characteristics and its effect on the flow field by means of PIV and high-speed visualization techniques.

1.1 Objective

The Center for Space Exploration and Technology Research (cSETR) at the University of Texas at El Paso specializes in propulsion and combustion research. Of the many instruments available in the center, is a 10 kHz Particle Image Velocimetry (PIV) and a 3 kHz Planer Laser Induced Fluorescence (PLIF) system. The facility also has 3 kHz high speed imaging system and a compressor system, capable of providing the airflow needed to reach the desired flow conditions. The studies conducted in this work are experiments supported by the Army Research Office (ARO) and a collaboration with Princeton University. The main overall objectives of this project are proposed as following:

- To study the global characteristics of a backward facing step high intensity turbulent flow using high speed flow visualization technology.
- To study flow and determine the flame zone characteristics using Time Resolved Particle Image Velocimetry (TR-PIV)
- To generate components of turbulent intensity and turbulent kinetic energy.
- To define the effects of bulk velocity parameters, turbulence parameters and recirculation zone characteristics that affect flame location, shape, fluctuation, reaction zone and local displacement speed.

The goal of the presented work is to utilize previous studies made and establish the limits of flame regime boundaries under Mach Number (M)>.3 and $(Re_t) > 10^3$ of CH_4 – air premixed flames using the Borghi-Peters diagram as a guideline. This study will generate the components of turbulent intensity and turbulent kinetic energy and define the effects of bulk velocity parameters, turbulence parameters, and recirculation zone characteristics that influence flame behaviors

Chapter 2: Theory and Literature Review

In order to achieve the objective of the proposed work, and to fully characterize the turbulent flow that occurs during experimentation, it becomes necessary to provide a thorough literature review along with the theories being utilized to accomplish this.

2.1 Flow Over Backward Facing Step

The flow over a backward facing step is a well-studied phenomenon in fluid mechanics, and its flow characteristics are used in this study to stabilize a highly turbulent flame, by using the low velocity zone, or recirculating zone, formed at the onset of the step. Extensive experimental and numerical work has been done on backward facing step flow problems, and due to its geometric simplicity this problem has been used for numerical validation for computational fluid dynamics (CFD) [1]. Biswas et al [2] and Armaly et al [3] have conducted extensive studies on flow over the backward facing step geometry both, experimentally and numerically. These studies helped the understanding of this phenomenon under high velocity flows that generate a much more turbulent flow conditions. Yuan and So [4] conducted a more detailed study where more characterization parameters in simple flow over this geometry were used. With an inlet velocity of U_∞ and an entry length of h followed by a flow expansion to a length of H , the fluid behavior when going through this geometry is depicted in Figure 2.1 where the different flow structures can be identified. For the present study, the ones of interest include the recirculation region, used as flame anchoring mechanism, and the separation shear layer, which strongly influences flame behavior.

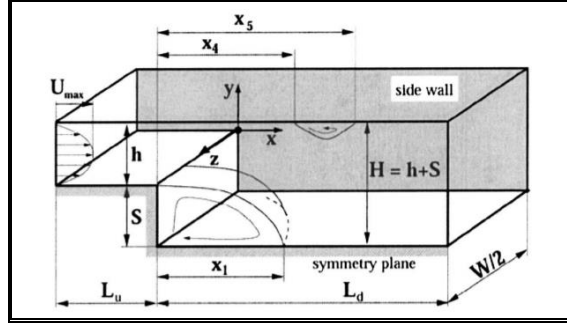


Figure 2.1: Schematic of different separation zones in a backward facing step [2]

For the present study, CFD analysis has been conducted in a previous work [5] in order to characterize and attempt to predict the flow structures present in the combustor design (recirculation, reattachment length, length scales, etc). Figure 2.2 shows the validation of the data in a 2D backward facing step channel with an expansion ratio of 2:1 by using the separation length with respect to Reynolds number. It is seen how the “CFD Project” compares to results acquired by other researchers with a good match. The experimental geometry and boundary conditions can be found in more detail here, [5].

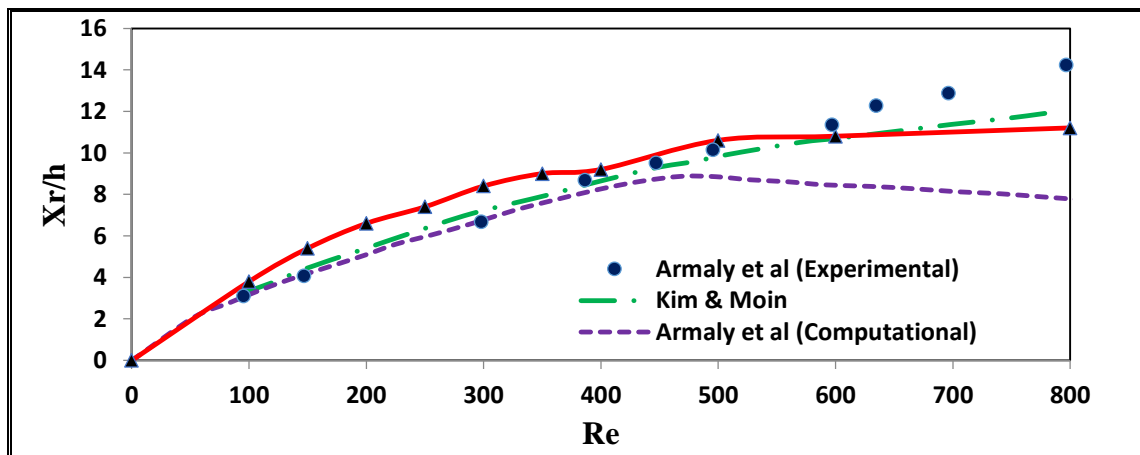


Figure 2.2: CFD result validation with experimental data [5]

2.2 Turbulent Flow

In fluid mechanics, a turbulent flow is characteristic of its unpredictability, unsteadiness, and chaotic nature. It is often found in engineering applications and it is of particular interest in combustion applications since it allows for a better mixing environment for the reactants. This important transport characteristic of turbulent flows is well demonstrated by Osborne Reynolds [6]. In this study dye is injected onto the centerline of a pipe where water is flowing through. Reynolds later established a single non-dimensionalized flow parameter known as the Reynolds number (Re) [7]. This parameter presents the ratios of the inertial forces to the viscous forces and its defined as

$$Re = \frac{UL}{\nu} \quad (2.1)$$

where U is the fluid velocity, L is the characteristic length, and ν is the kinematic viscosity. By using this non-dimensionalized parameter a flow can be characterized under the laminar, transitional, or turbulent range as shown in table 2.1

Table 2.1: Flow regimes and their Reynolds number range

Fluid Characterization	Reynolds Number Range
Laminar	$Re \leq 2300$
Transitional	$2300 < Re < 4000$
Turbulent	$Re \geq 4000$

The effectiveness of turbulence to transport and mixing is the main reason why this flow is highly desirable in some common engineering applications. As mentioned previously, in a combustion application the efficiency of heat and mass transfer, combustion and chemical reactions depend on the mixing process where turbulence plays a significant role, a rapid and efficient reactant mixture the combustion process also allows for lower pollutant emissions.

2.2.1 STATISTICAL DESCRIPTION

The characteristics and different aspects that describe a turbulent flow are described in through detail by the work of Pope [8]. In his work Pope describes how turbulent flows show a nonlinear behavior since the velocity field, $U(x,t)$, is random and unpredictable along with the fluctuations in temperature and pressure. Figure 2.3 presents a point measurement plot of velocity with respect to time of a turbulent flow.

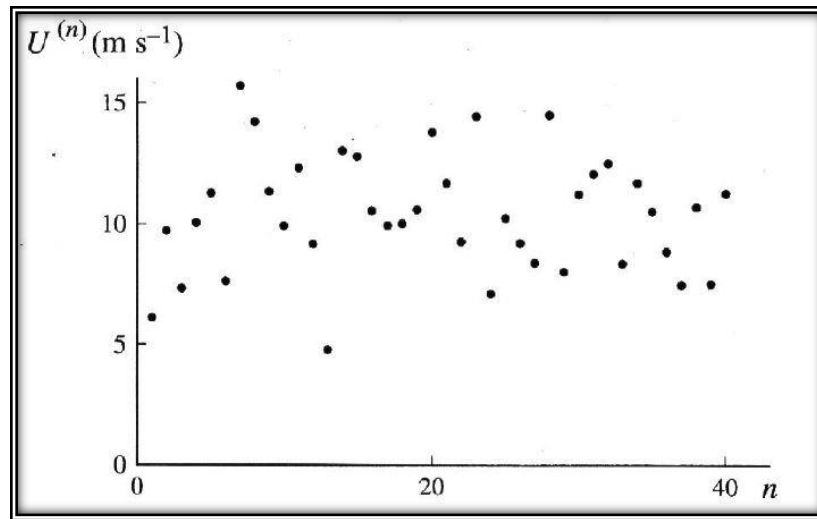


Figure 2.3: Variation in velocity during turbulent flow [8]

In order to ease the calculations involved with turbulent flows, the local flow parameters are decomposed into a mean and a fluctuating component and are defined as

$$u(t) = \bar{u} + u'(t) \quad (2.2)$$

$$u'(t) = u(t) - \bar{u} \quad (2.3)$$

Where $u(t)$ is the instantaneous velocity, \bar{u} is the mean velocity, and $u'(t)$ is the velocity fluctuation term. Figure 2.4 helps illustrate how the instantaneous velocity is decomposed into these two components.

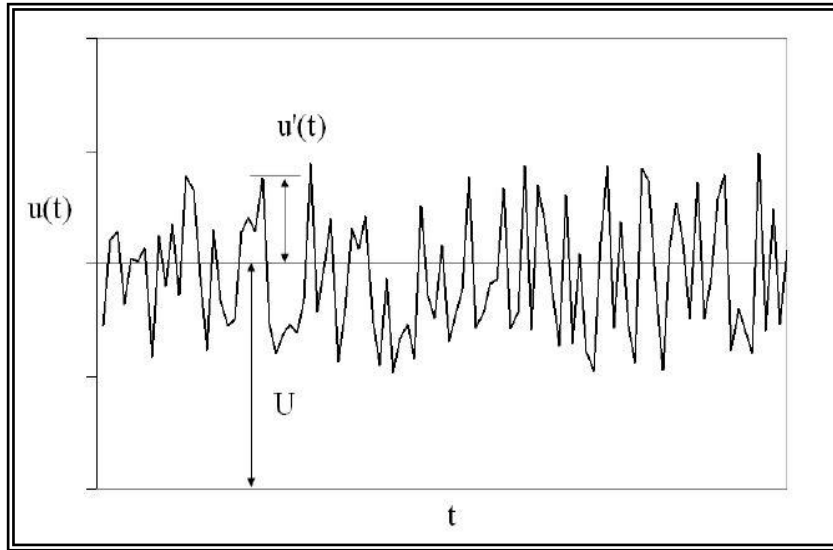


Figure 2.4: Average and fluctuation components of an instantaneous velocity measurement [8]

As seen in Figure 2.4, the velocity u varies randomly with respect to time. As a result, the Navier-Stokes equation cannot predict the velocity variability accurately. Due to this random variability in velocity, a probabilistic approach to solve turbulent flows is used. A more detailed discussion regarding turbulent flows can be found elsewhere [8]. The mean velocity \bar{u} can be

calculated by taking an average velocity measurement for a certain time interval that is much larger than the turbulent time scale [9]. From the velocity fluctuation, it is then possible to calculate the root mean square (R.M.S.) value of the turbulence component.

$$u_{rms} = sdev(u'(t)) = \sqrt{var(u'(t))} = \sqrt{u'(t)^2} \quad (2.4)$$

2.2.2 TURBULENT INTENSITY

The turbulent intensity is a parameter that helps define the turbulence level of a flow field and its commonly expressed as a percentage where a perfectly laminar flow has a turbulent intensity of 0% since the u_{rms} value would be 0. Turbulence intensity is defined as

$$I = \frac{u_{rms}}{\bar{u}} \quad (2.5)$$

Typical turbulence intensity of highly turbulent flow inside rotation machinery and inside complex geometries is around 5 to 20%.

2.2.3 TURBULENT KINETIC ENERGY

Turbulent kinetic energy (TKE) is a measurement of energy per unit mass due to the velocity of the flow. For a 3-dimensional flow field, if the R.M.S. of the velocity fluctuation of x, y and z direction are $\overline{u_x'^2}$, $\overline{u_y'^2}$ and $\overline{u_z'^2}$ respectively, then the TKE can be calculated by eqn. 2.6.

$$k = \frac{1}{2} \overline{u'_i u'_i} = \frac{1}{2} (\overline{u_x'^2} + \overline{u_y'^2} + \overline{u_z'^2}) = \frac{3}{2} \overline{u'^2} \quad (2.6)$$

From this definition the turbulent kinetic energy of the flow can be calculated through the u_{RMS} values [8].

2.2.4 TURBULENT LENGTH SCALE

When analyzing a turbulent flow, the characterization of energy modes and length scales is crucial to generate a map of the flow field. The turbulent length scale, l , helps characterize a turbulent field by defining the size of eddies containing the largest amount of energy, which are the largest eddies. These large eddies having the largest amount of energy, loose their energy to smaller eddies within them, until the smallest eddies dissipate simply in the form of heat and due to viscous forces. The interactions between the large scale eddies and the small scale ones can be described by Kolmogorov's hypothesis [10]. It is also referred to as the energy cascade principle depicted in Figure 2.5.

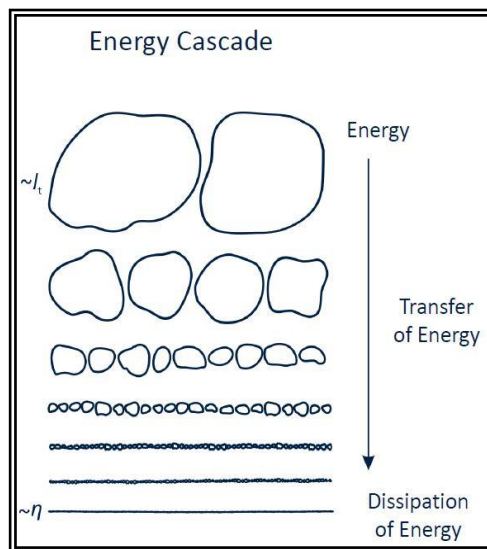


Figure 2.5: The “energy cascade” proposed by Kolmogorov [10]

The energy dissipation starts at the largest scale l , and it is gradually lost until the smallest scale η is reached. Once the energy reaches the dissipation of energy range, the smallest scales of length, time, and velocity can be calculated based on the viscosity of the fluid. The small scale parameters are defined as follows

$$\eta = \left(\frac{v^3}{\varepsilon}\right)^{\frac{1}{4}} \quad (2.7)$$

$$t_\eta = \left(\frac{v}{\varepsilon}\right)^{1/2} \quad (2.8)$$

$$u_\eta = (\varepsilon v)^{1/4} \quad (2.9)$$

$$\varepsilon \equiv \frac{u_0^3}{L} \quad (2.10)$$

Where ε represents the energy dissipation, which scales with the characteristic velocity u_0 , and length scale. Equations 2.7 – 2.10 lets us see how the smallest scales are defined by kinematic viscosity and the energy dissipation rate. Using equation 2.8, we can find the time interval used to average the velocity and calculate the mean and fluctuating velocity components of the flow.

2.2.5 GRID INDUCED TURBULENCE

The use of a grid, or a perforated plate, to induce turbulence in a cross-flow is used widely and its different features have been studied previously [11]. By implementing this perforated plate, grid, to the flow path, causes the flow to become more turbulent. The use of a grid creates

homogeneous turbulence which increases with time by $t = x/U_0$, and decreases along the x -direction relative to the point of injection while having an increase in the R.M.S. value along the x -direction 10% greater than the y -direction [8]. The behavior of this grid induced turbulence is analogous to freely evolving turbulence [12].

Isotropic-homogeneous turbulence is a property of certain turbulent flows and it is used to ease calculations. It assumes a flow is independent of orientation and position in space. This property implies that the average properties are independent of direction as shown in Figure 2.6.

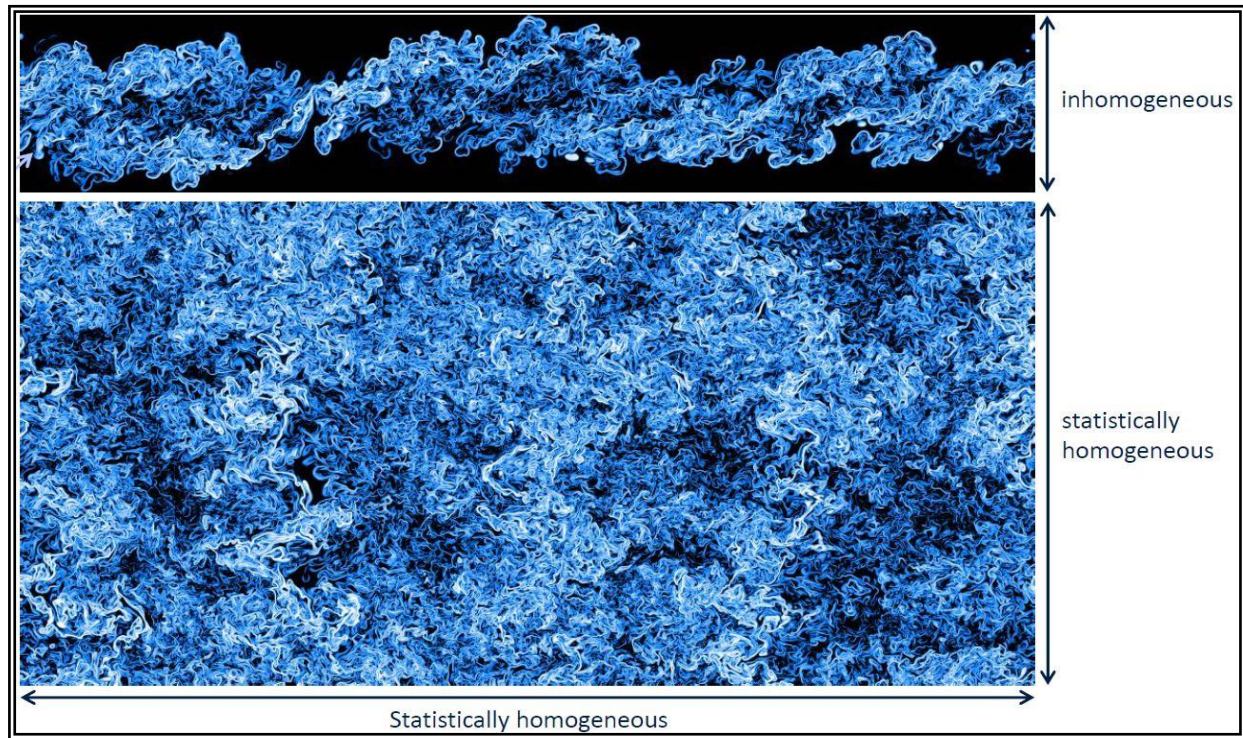


Figure 2.6: Statistically homogeneous isotropic turbulence [12]

Isotropic-homogeneous turbulence can be assumed if rotation and buoyancy are not important and there is no mean flow, therefore

$$\overline{u_1'^2} = \overline{u_2'^2} = \overline{u_3'^2} \quad (11)$$

$$\overline{u_i' u_j'} = 0 \quad (12)$$

By having a grid generating homogeneous isotropic turbulence, there is a transition to fully developed turbulence at the point where the flow first encounters the grid, and as the flow progresses it starts to decay starting with the smallest scale eddies as presented in Figure 2.7.

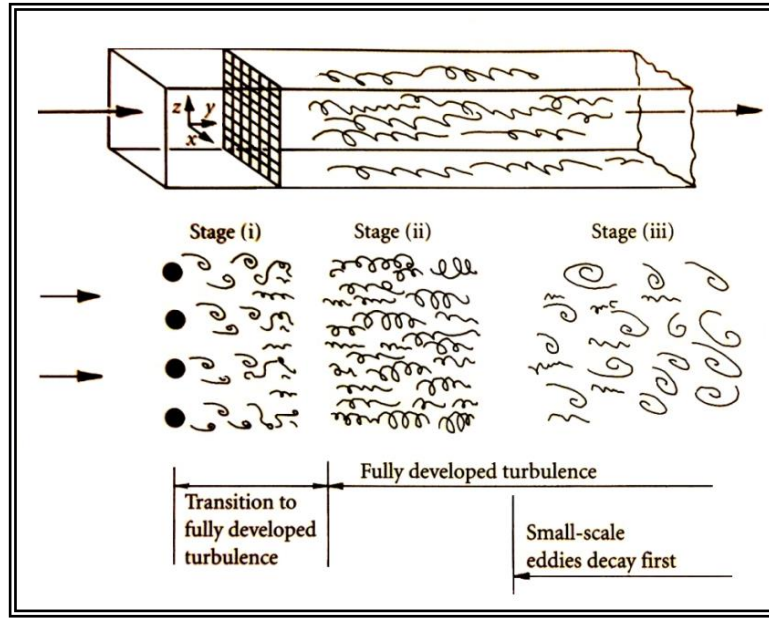


Figure 2.7: Visual representation of grid induced turbulence in a duct [12]

2.3 Optical Diagnostics

Laser imaging techniques provide a non-intrusive way of measuring flow parameters, combustion characteristics, emissions and resolve for most of their individual components. Optical diagnostics began as early as the 1800's, but were popularized in the early 20th century. Due to advancements in the technology, these techniques have been implemented to address problems that have been thought not possible due to lack in the needed laser power, firing rates, and cost.

Now these technologies are being used widely in turbulent combustion research [13]. There are a wide variety of imaging techniques and systems, and in the present study a PIV and LIF system are to be used. These systems are to be run separately, as well as simultaneously.

2.3.1 PARTICLE IMAGING VELOCITY (PIV)

Particle imaging velocimetry is a non-intrusive laser technique that allows the instantaneous velocity vector fields acquisition with good spatial resolution. Flow characteristics can be obtained using PIV, such as velocity vector fields, vorticity, strain and divergence of the flow, amongst many other. In order to be able to conduct a PIV experiment, three main components are required: a high-powered laser system, seeding particles or other flow tracer, and a high-speed CCD camera. These components provide researchers with experimental flexibility and allow for the application of a PIV analysis on a large variety of configurations. There have been significant developments in this technique [14 - 16] and it has become a powerful tool to study turbulent flows due to its flexibility, and the fact that the technique is non-intrusive, requiring only visual access to the area in question.

In order to acquire a velocity field, a particle displacement over a specified small finite separation of time, Δt is used. A correlation analysis is then used to extract the particle displacement Δx , and a first order velocity estimate is calculated as

$$u = \frac{\Delta x}{\Delta t} \quad (13)$$

where Δx is the average displacement of the particle in the fluid over the time interval $\Delta t = t_2 - t_1$ [15]. The t_1 and t_2 can be recorded in to same frame or in a separate frames. The success of the PIV imaging depends on the accurate coupling between the fluid and the particles. The number of particles per unit volume should be sufficiently low in order to preserve the original flow characteristics [17 - 18], but at the same time not too low as higher particle density increases the measurement's resolution. Such dilute condition is expressed in inequality 14 where d_p and ρ_p are the particle diameter and density, respectively and μ , v_r , δ_p are the fluid viscosity, average particle velocity and average distance between particles respectively.

$$\frac{\rho_p \pi d_p^4 v_r}{18 \pi \delta_p^3} < 1 \quad (14)$$

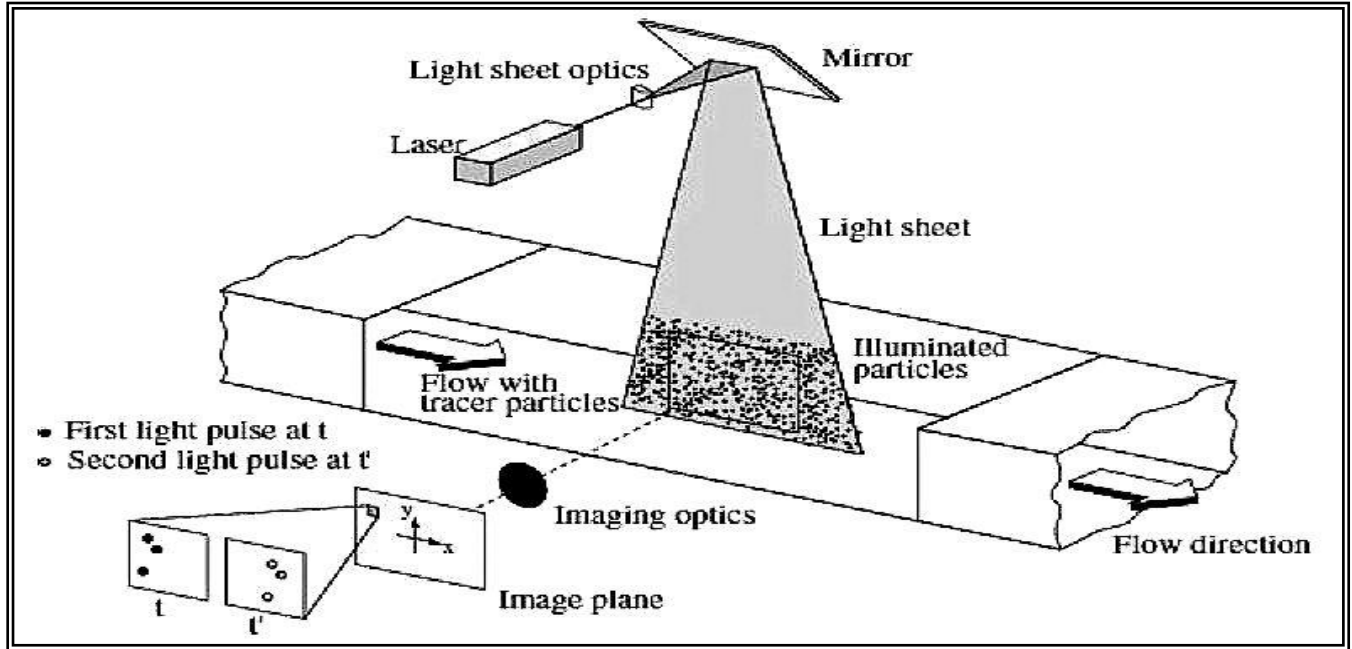


Figure 2.8: Schematic of experimental arrangement for PIV [19].

It is important to note that the laser beam is transformed into a light sheet as to illuminate a plane of interest. The laser sheet illuminates the tracer particles; the camera then picks up the

particle's light, and through software manipulation and post processing the flow is re-created. The image is then further post processed to extract the flow data from the image ensembles. It is very important to select the accurate particle size for a specific experimental setup. The size can be determined with the help of the Stokes number, St_{PIV} that is defined as τ_s/τ_{PIV} where τ_s is the particle relaxation time and τ_{PIV} is the small finite separation time between two observation or pulse separation time. In order to achieve negligible particle-fluid velocity difference over the pulse separation, St_{PIV} must be less than 1. Equation 15 represents the particle relaxation time. Moreover, the relative velocity error due to Brownian motion is shown in equation 16 where D is the diffusion coefficient, k is the Boltzman's constant, T is the absolute fluid temperature and u is the mean velocity of fluid [20].

$$\tau_s = d_p^2 \frac{\rho_p}{18\mu} \quad (15)$$

$$\varepsilon_B = \frac{1}{u} \sqrt{\left[\frac{2D}{\Delta t} \right]}, \text{ where } D = \frac{kT}{3\pi\mu d_p} \quad (16)$$

For the presented work a particle size of 1 micron made out of alumina were selected based on these parameters. The light plane is generated by a '*15-1000 Dual power*' 527nm Neodymium-doped Yttrium Lithium Fluoride (Nd-YLF) laser with a pulse energy of 15mJ/pulse. The maximum power output of this laser is 100W and the pulse duration is 150ns/CW which is shown in the experimental setup section. This laser generated a 75mm wide 0.1mm thick light sheet which is guided by a 45° angle of attack (AOA) line mirror into the laser sheet optics. The image plane is

captured by a '*Speed sense 9070*' CCD camera with a frame rate of 10 kHz. The image plane is 73mm x 35mm in dimension or 598 x 288 pixel.

2.3.2 PLANAR LASER INDUCED FLUORESCENCE (PLIF)

New advancements in laser diagnostics have led to the popularity in spectroscopy to analyze and measure the interaction between matter and light. The strength of this spectroscopy is measured as a function of wave length and optical frequency and is used to visualize selected molecules and radicals making it a popular selection for the study of combustion processes. As the name implies, when using the PLIF measuring technique a thin laser light sheet, which is usually tuned to excite the radicals/molecules of interest, is produced to illuminate a plane of the flame, this laser light causes the molecules to emit fluorescence radiation that can be then recorded using an Intensified Digital Camera (ICCD) which is usually accompanied with a band pass filter and an image intensifying unit to record select wavelengths.

There exist different types of lasers for different spectroscopy applications. Dye Lasers are a popular PLIF alternative due to their capability of being tunable to a wide range of wavelengths, particularly in the visible spectral range, near ultraviolet, and near infrared regions. As discussed earlier, in order to make the molecules/radicals of interest fluoresce, the molecules must be excited into a high energy level, and this is done using the laser source tuned to a wavelength that resonates between the excited state and a discrete lower state of the molecule. Figure 2.9 demonstrates a simplification of this technique.

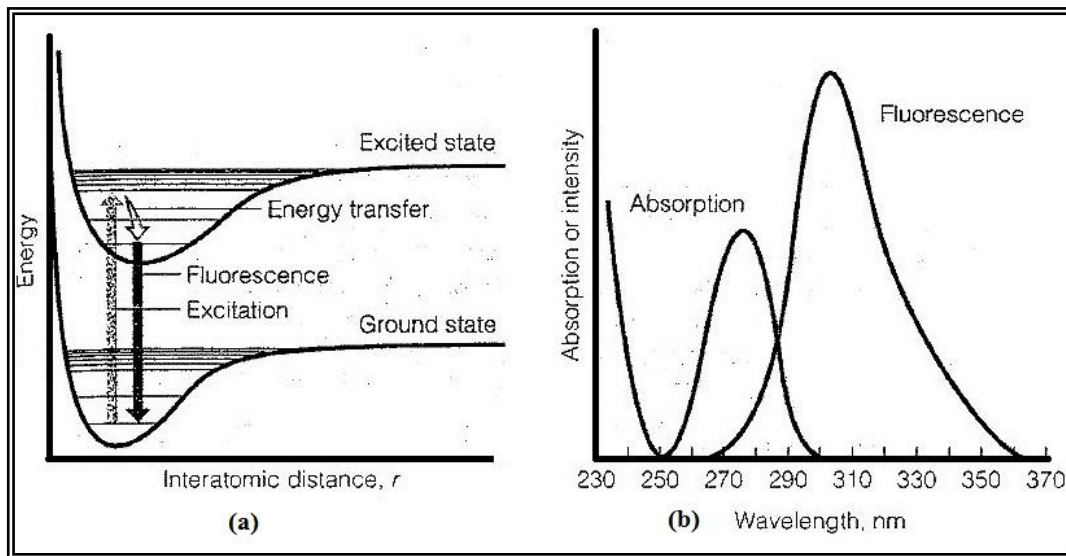


Figure 2.9: (a) Fluorescence technique basic principle. (b) Energy Distribution

From the figure it can be seen how the molecule is initially at a ground state. Once the laser energy is applied at a relevant wavelength, in the case of Figure 2.9 283 nm for the OH radical, the molecule is brought up to an excited state. Upon relaxation the molecule releases a fraction of the energy in the form of a photon, or light, which is what we call fluorescence light. Figure 2.9 b depicts how due to energy re-distribution the wavelength of fluorescence is shifted to a higher wavelength when compared to the absorption band.

PLIF has emerged as a popular combustion study technique due to its good temporal and spatial resolution, narrow line width, wavelength tunability, wide range of power options, and ultra-short pulse generation. It is of no surprise a popular tool to analyze and study reacting flows after its introduction in the early 80's [21 - 22]. With advancements in laser technology and image capturing devices, PLIF has come a long way allowing scientists and engineers to analyze at a higher frequency rate, this translates to having the capabilities of this technique available to

analyze higher velocity phenomena, and has demonstrated the qualitative time-averaged imaging of concentration, temperature, pressure, and velocity [23].

In order to perform quantitative measurements of a given species using the PLIF technique, the absorption and emission wavelengths of that specific molecule, and the rate of radiative decay, responsible for the fluorescence signal must be known. For some radicals the excitation and detection wavelength ranges have been well studied and documented while others remain to be further investigated and validated. In a typical PLIF system, a UV laser beam is tuned to excite and start this molecular transition. Similar to PIV a set of cylindrical and spherical lenses are used to turn the laser beam into a sheet exciting the selected molecules. The fluorescence of the selected particles is recorded usually by an intensified digital camera coupled with a band-pass filter for recording of the selected wavelength. The spatial resolution of this technique depends on the pixel size of the detector array, the image magnification factor, the size of the beam, the depth of field, and the energy of the beam. A synchronizing box and a trigger mechanism are used to drive the laser pulses in synchrony with the camera while keeping a suitable gate duration.

The LIF signal is commonly used in combustion research to trace the flame front. In the present work a methane/air flame is used so it is important to trace radicals that appear in the flame front area of the flame (OH, CH, CH₂O, CHO). Due to its high concentration, the OH radical is widely used as a flame front tracer. In this work the OH PLIF imaging is performed by using a high-energy laser routed through a dye laser system to shift the 532 nm pump laser radiation down to the desired 283nm.

It is common practice to investigate the radical pool of a fuel/oxidant mixture to get a better idea of what the radicals present in the reaction would be, as well as to get a better insight as to which radicals could perform better as “flame front tracers”. Figure 2.10 presents the radical pool of the 1D methane/air combustion process.

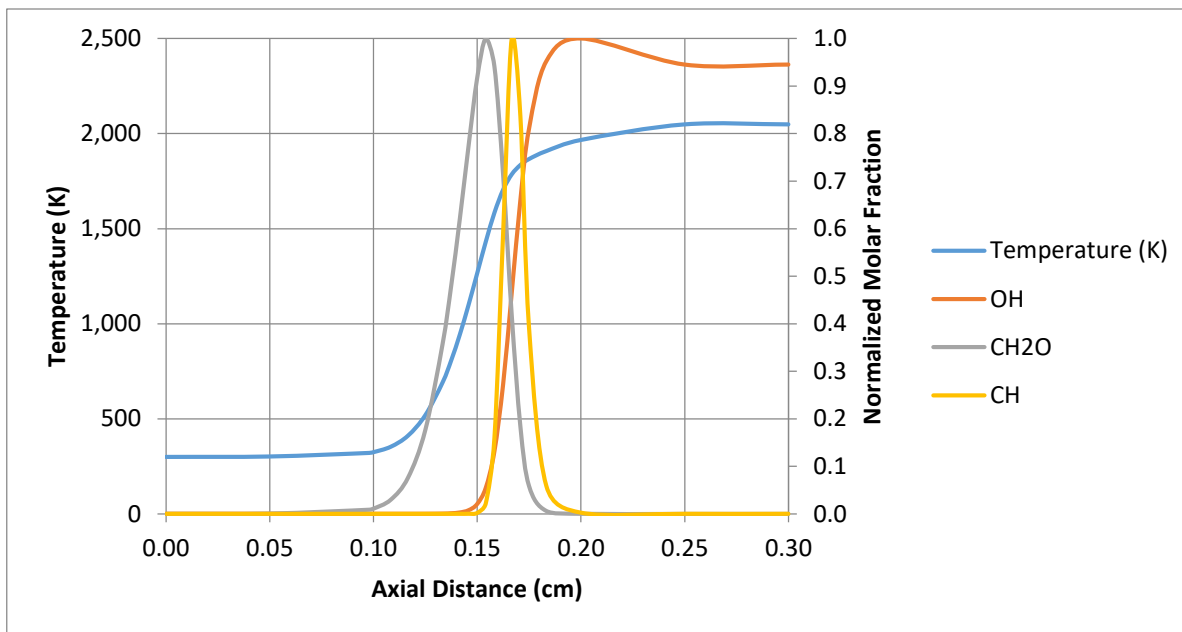


Figure 2.10: 1D radical pool of a methane/air flame with normalized molar fraction with respect to the max of each species

The analysis was conducted utilizing a popular methane oxidation mechanism with CHEMKIN software (GRI Mech 3.0). From figure 2.10 it is possible to get a good idea of what radicals to expect, even under turbulent conditions. In this analysis we include the hydroxyl (OH), formaldehyde (CH₂O), and the CH radical. All these molecules are considered to be flame front tracers as they appear at the beginning of the flame front, and in the case of CH, appear only on the flame front thickness. It is also possible to understand what kind signal should one expect when conducting PLIF measurements of these molecules. From Figure 2.10 we can see that the OH

radical has a strong molar fraction concentration past the highest temperature point. This would mean that the OH molecule would be expected to have a strong signal not only at the beginning of the flame front, but past it into the combustion products region. Unlike the OH radical the CH radical can be expected to have a brief existence within the flame front, meaning that the CH would be considered to be a better flame front tracer than OH.

Using CHEMKING with GRI Mech 3.0 we can also study the effect different relevant parameters may have on the radical's concentration as presented in Figure 2.11.

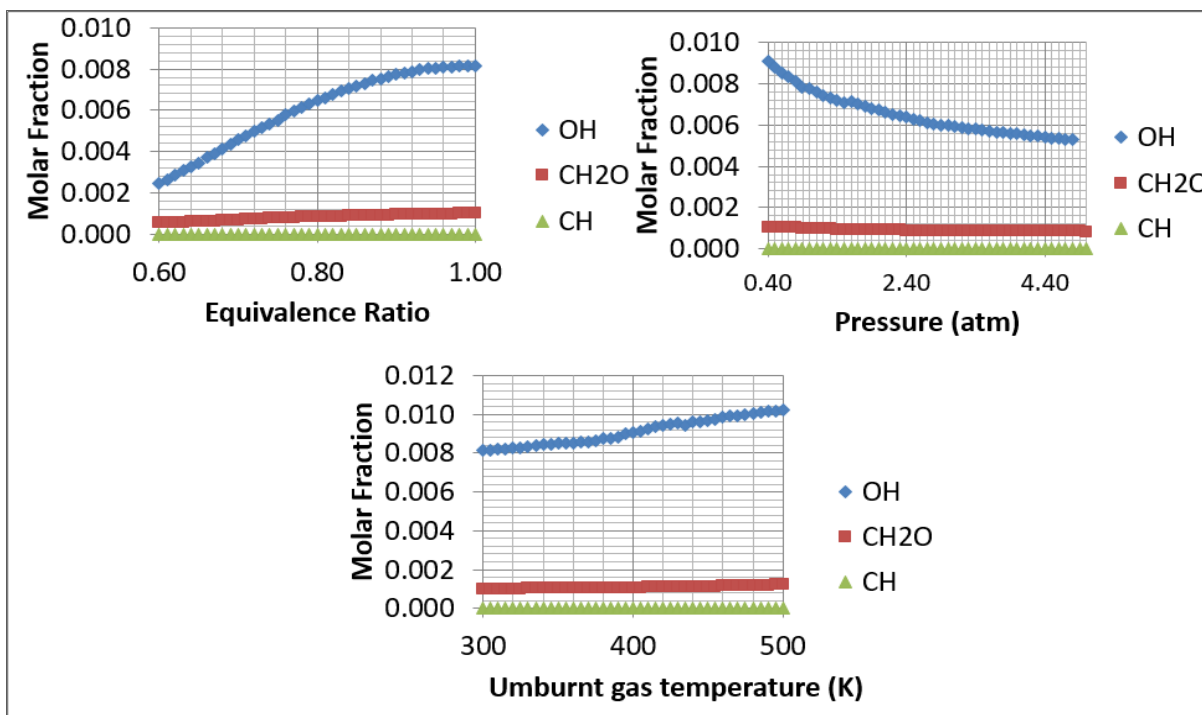


Figure 2.11: Effects of unburnt gas temperature, equivalence ratio, and pressure on different species concentrations.

In Figure 2.11 we investigate different parameters that can affect the concentrations of radicals of interest as flame front tracers. It is evident how the CH and CH₂O species remain relatively unchanged throughout the different conditions presented. It is also noted that they present a very small concentration throughout. It would then be expected that the CH and CH₂O spectral emissions to be weak, leading to a higher power rating on the light source being used.

We notice an increase in OH concentration as the equivalence ratio increases, a decrease in concentration as pressure increases and another increase as unburnt gas temperatures increases. The most important trend to notice is the considerably higher concentration OH has when compared with CH and CH₂O. Thanks to the high concentration at a wide range of conditions, OH is a popular species used to trace the flame front.

2.4 Combustion

Much like classifying flows using the Reynolds number, the work presented here has opted to classify the flames being studied using the Peters-Borghi Diagram. This diagram takes into account the turbulent nature of the flow and combines it with flame characteristics in order to define the flame regime.

Combustion is a rapid oxidation process generating heat or both, light and heat [24]. The flame is a three-dimensional thin reaction zone where a chemical reaction propagates through the unburned air-fuel mixture. This thin reaction zone, or flame, releases the heat caused by the chemical reactions happening within it, which in turn causes a rise of the temperature and pressure of the surrounding gas through diffusion and radiation, leading to the self-sustained nature of a flame. The combustion process can be characterized in two main types:

- Premixed combustion
- Non-premixed combustion

The main types of combustion are related to the state of “mixedness” the reactants are in, before entering the main reaction zone, or as it is known, the flame front. In the premixed combustion case the fuel and the oxidizer are mixed at the molecular level prior to entering the flame front. On the other hand, in a diffusion flame, the reaction occurs at the interface of the fuel and oxidizer and it is mainly driven by diffusion. Figure 2.12 illustrates the reaction rate with respect to the concentrations of fuel and oxidizer. A key difference between these two types of combustion is that in a diffusion type of flame the reaction and the mixing occur at the same time.

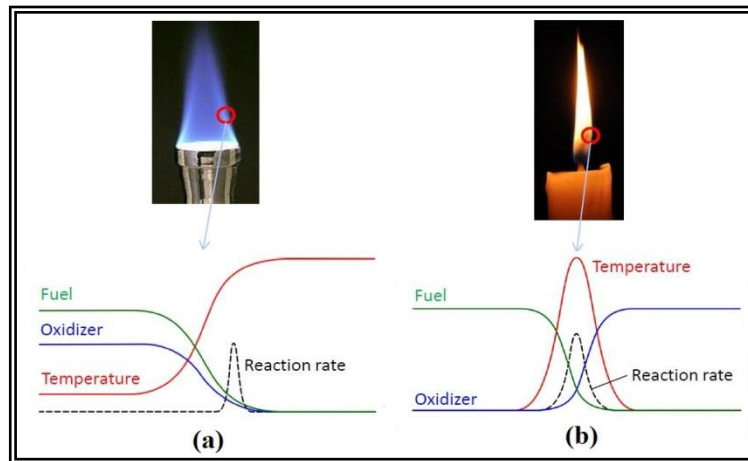
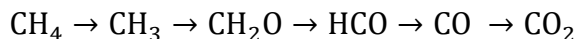


Figure 2.12: Concentration and temperature profile of a) premixed, b) diffusion flames [27]

For the present work, a premixed methane/air flame has been studied. Although the bulk products from hydrocarbon combustion result in carbon dioxide and water, the mechanisms that

lead to these products has been a topic of continuing research. In recent years researchers have been trying to describe combustion processes at the level of elementary chemical steps with detailed chemical kinetic mechanisms [25 - 32]. Some mechanisms contain thousands of elementary reaction stems with hundreds of different chemical intermediate species. For example, hydrogen combustion can be described utilizing 21 steps with 8 chemical species, combustion of carbon monoxide with 30 steps and 1 species, methane, methanol, ethane, ethylene, and acetylene combustion with 134 steps and 30 species, and propane, propene, allene, and propyne combustion with 177 steps and 37 species [33]. In order to avoid complexity, it is common practice to simplify the path of oxidation of hydrocarbons and only take into account the major contributors to its oxidation. In the case of methane the oxidation can be written as:



The basic combustion process can be described by the fuel and the oxidizer, known as the reactants, undergoing a chemical process while releasing heat to form the products. When all the carbon atoms in the fuel are converted to carbon dioxide and all the hydrogen converted into water then the process is known to be stoichiometric, that is, there is just enough air in the mixture to react with the methane present as to have no excess air once the combustion process is complete. Figure 2.13 presents a simplified oxidation path for any hydrocarbon and air where z is the stoichiometric coefficient of the oxidizer. This reaction yields five unknowns: z , a , b , c , and d . In the case of stoichiometric combustion, $d=0$ since there is no excess air left after the reaction takes place while the rest of the variables can be found by simply balancing the formula when $d=0$ yielding a balanced equation for stoichiometric methane/air combustion of:

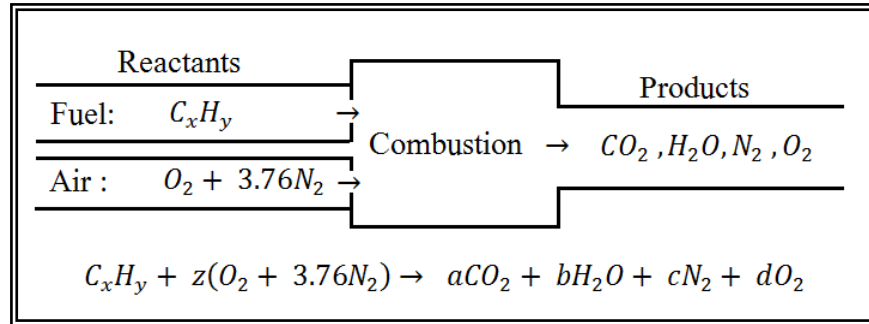
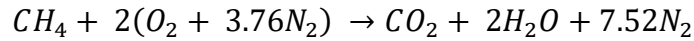


Figure 2.13: Simplified hydrocarbon/air oxidation mechanism

The variables may be found for any hydrocarbon if we set $x=a$, $y=2b$, $2z=2a+b$ and $3.76z=c$.

2.4.1 PREMIXED LAMINAR FLAMES

Now that a ground basis for combustion has been set, we may address one of the variables needed to define the flame regimes being generated, but first an introduction to the premixed laminar flames is provided. Friedman and Burke [34] identified two distinct zones in a premixed laminar flame, the preheat zone and the reaction zone. Figure 2.14 presents these two different zones of a laminar flame structure.

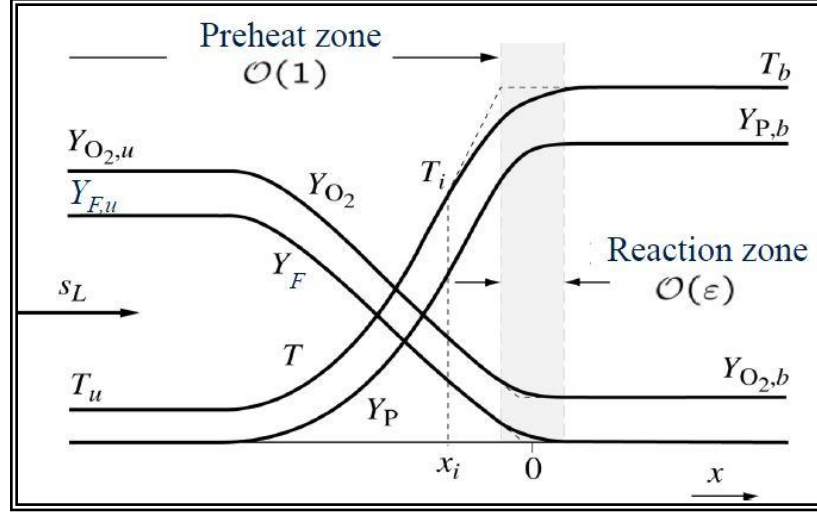


Figure 2.14: Temperature and species concentration profiles of a premixed laminar flame [34].

In Figure 2.14, it can be appreciated how the bulk of the heat release happens in the reaction zone by the high release of chemical energy and the high temperature gradient that happens in that zone. The reaction zone can be further divided into two sub-zones. The primary reaction zone where the fast chemistry happens causing a large temperature gradient giving rise to the self-propagating nature of the flame [35], and the secondary reaction zone where the slower chemical reactions take place dominated by three-body radical reactions.

2.4.2 LAMINAR FLAME SPEED (S_L)

As we have learned so far, the flame front is what makes up the flame, it is where the bulk of the chemical reaction takes place, and where the highest heat release takes place, giving rise to the self-propagating nature of a premixed laminar flame, therefore to characterize a flame we must pay close attention to the flame front. In order to characterize a laminar flame, or the laminar flame front, one needs to measure the laminar flame speed (S_L) and the flame thickness (δ). Laminar

flame speed is defined as the speed at which an un-stretched laminar flame front will propagate through a quiescent mixture of unburnt reactants, and it varies depending on the fuel equivalence ratio, pressure, and the unburnt reactants temperature. The laminar flame speed phenomena has been studied extensively and the methane/air flame speed at different conditions is well documented. Figure 2.15 presents the flame speed of methane/air at atmospheric pressure [36 - 38].

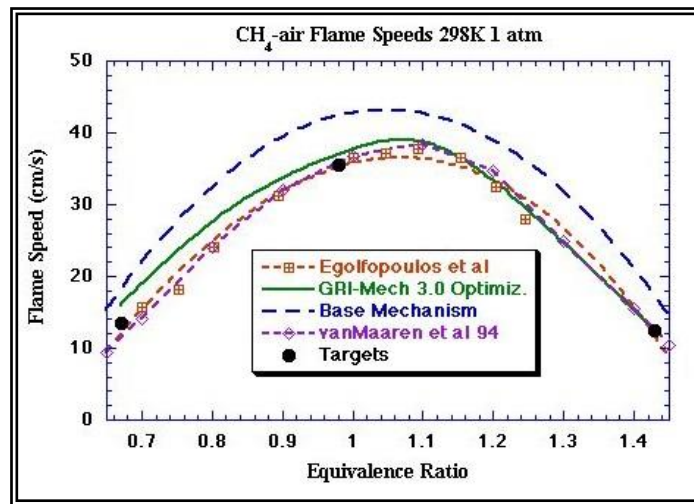


Figure 2.15: Laminar flame speed of methane/air at 298K and 1 atm pressure [39]

The effects of pressure and temperature have been extensively studied and it is well documented [40 - 46]. For the present work, the studies have been conducted at ambient temperature and pressure conditions. It can be seen how GRI Mech 3.0 exhibits a good agreement amongst different other researcher's results. For this study the S_L parameter is calculated using CHEMKIN software with GRI Mech 3.0.

2.4.3 LAMINAR FLAME THICKNESS

Similarly, to laminar flame speed, laminar flame thickness δ_L is a parameter needed to define the flame regime acquired during experimentation. Like the laminar flame speed, laminar flame thickness has been extensively studied. For the presented work the laminar flame thickness has been calculated according to Gottgens, Mauss, and Peter's study [47] along with CHEMKIN software. The flame thickness is calculated based on the steepest temperature gradient as presented on Figure 2.16 taken from [47].

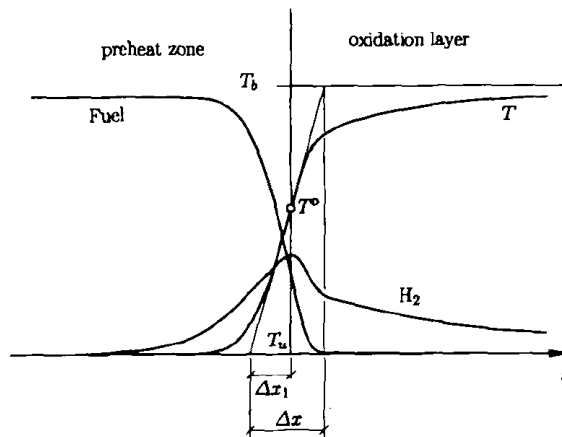


Figure 2.16: Illustration of the flame structure where Δx is the flame thickness, defined by the steepest tangent to the temperature profile [47]

2.5 Flame Regimes

In order to describe the different flame regimes, similarly to how we describe fluid flow as being turbulent, transitional, or laminar, we utilize dimensionless numbers. The most commonly used are under the assumption of the thermal diffusivity being equal to the mass diffusivity

(Schmidt number $Sc=1$), and they are the turbulent Reynolds number (Re_T), the Damkohler number (Da), and the Karlovitz number (Ka) as defined by the set of equations 17.

$$Re_T = \frac{u' L_T}{s_L \delta_L} \quad ; \quad Da = \frac{L_T s_L}{u' \delta_L} \quad ; \quad Ka = \left(\frac{L_T}{\delta_L} \right)^{-1/2} \left(\frac{u'}{s_L} \right)^{3/2} \quad (17)$$

Flames at a high turbulence Reynolds number are characterized as being highly fluctuating. The Damkohler number is the ratio between chemical time scales and turbulent time scales, and it determines which mechanisms dominate the flame propagation between chemistry and turbulence. The Karlovitz number relates the thickness of the reaction zone to the smallest scales of turbulent flow, and it can be used to measure the degree of flame stretch.

To characterize turbulent flames and its propagation, most theories rely on phenomenological reasoning and experimentations. The propagation properties of turbulent flames, unlike that of laminar ones, are also a function of flow parameters and the geometry of the combustor. There are various methods and theories that help define turbulent flame characteristics and a widely used diagram summarizing them and dividing them into different categories was proposed by Borghi, and later modified by Peters [48 - 49]. This flame regime diagram (Figure 2.17) characterizes the different flame regimes based on dimensionless parameters (Re_T , Da , Ka), turbulent parameters (u' , L_T), and flame parameters (S_L , δ_L). A summary of the different flame regimes described by the diagram is presented in Figure 18.

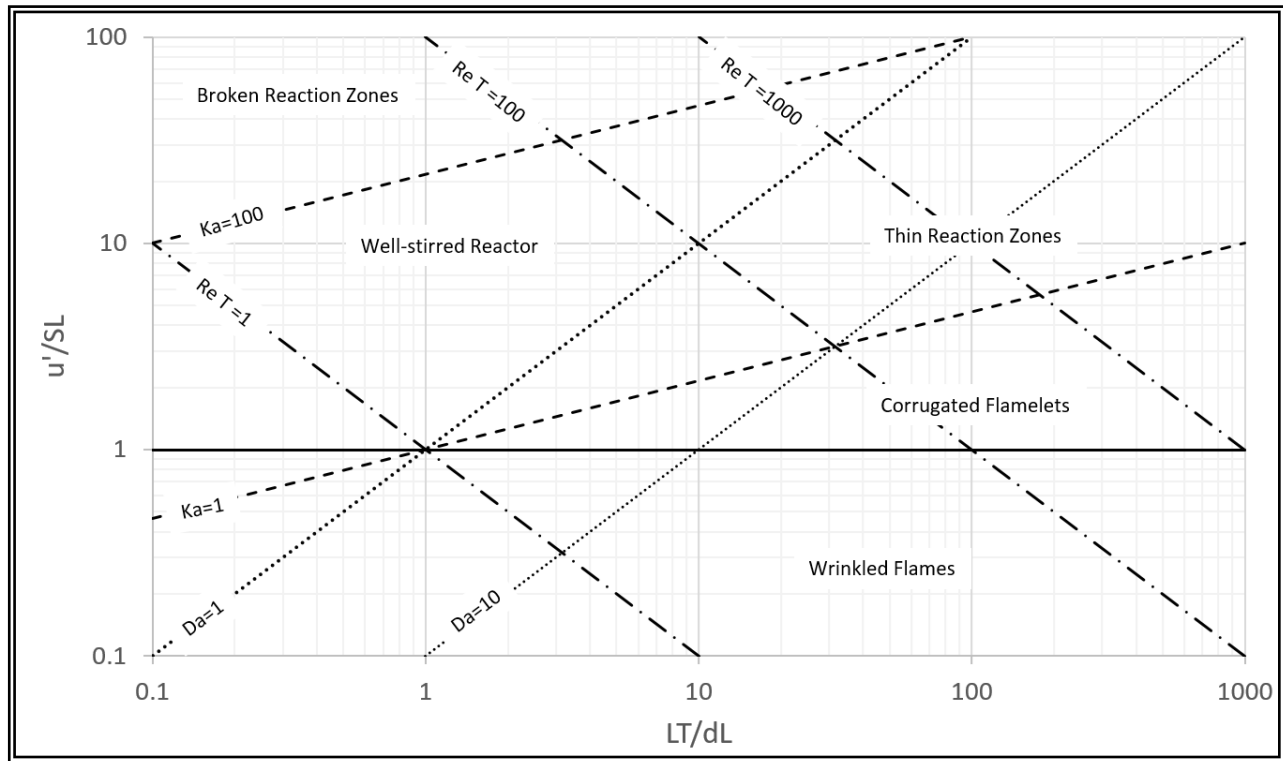


Figure 2.17: Flame regime diagram by Borghi and modified by Peters

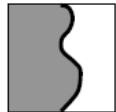

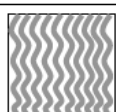
flame regime	Re_T	Da	Ka	u'/s_L	δ_L/η	graphical illustration of the flame front
wrinkled flame	> 1	> 1	< 1	< 1	< 1	
corrugated flame	> 1	> 1	< 1	> 1	< 1	
thickened flame (thin reaction zones)	$\gg 1$	≥ 1	> 1	$\gg 1$	> 1	
distributed flame (well-stirred reactor)	> 1	< 1	> 1	> 1	> 1	

Figure 2.18: Different flame regimes and the graphical illustrations of flame front characteristics [51]

2.5.1 WRINKLED FLAME REGIME

Delimited by the turbulent parameters presented in Figure 2.17, in the corrugated flame regime, the turbulent flame speed is much faster than the turbulent time scale, while the integral length scale is much larger than the flame thickness. This allows for the most energetic larger eddies in the flow to interact with the flame front causing it to become wrinkled.

2.5.2 CORRUGATED FLAME REGIME

When the turbulence intensity is higher than the flame speed, the flame speed is no longer able to damp out the energy from the turbulent flow reaching the flame front causing a break up of it. Breakup occurs due to the fact that $Ka < 1$, this means that the flame thickness is still smaller than the smaller eddies found in the flow while the turbulence intensity has increased. This intense turbulence results in small flame pockets breaking up.

2.5.3 THICKENED FLAME REGIME

The thickened flame regime or the thin reaction zone regime is characterized by $\frac{u'}{S_L} \gg 1$, $Re_T \gg 1$ and $Ka > 1$. Having a large Karlovitz number, entails that the smallest scale eddies, the Kolmogorov scale, is smaller than the flame thickness. Under these conditions the flame is no longer laminar and the small scale eddies are able to enter and stretch the flame front as postulated by Zimount [50] and explained by Borghi [51] and more recently by Peters [52]. Peters describes this thickened flame zone as highly stretched and divided into an inner sub-layer of some thickness, where the majority of the reactions take place, and a pre-heated zone. The stretching of the flame zone then leads to an increase in flame speed and thermal diffusion. The main purpose of this study

is to reach a thickened flame regime and investigate the flow's turbulent characteristics pertaining to the experimental setup and investigate the capabilities of the system. Presented in Figure 2.19, the location of the flame regime on the Borghi-Peters diagram is presented. The results of this study will also provide parameters needed to improve simulations of this flame regime.

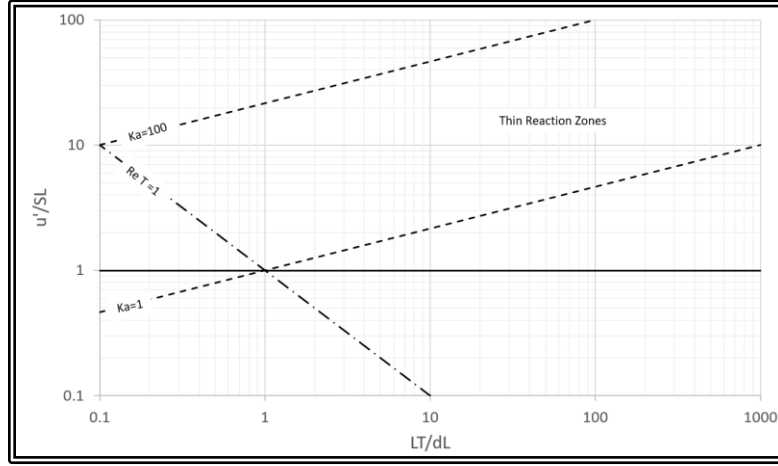


Figure 2.19: a) Thickened flame regime on the Borghi diagram

2.5.4 DISTRIBUTED FLAME REGIME

The distributed flame regime, also referred to the well-stirred reactor flame regime is characterized by $Da \gg 1$, $\frac{u'}{S_L} > 1$, $Re_T > 1$ and $Ka > 1$. Due to the high value of Damkholer number, the mixing time scale is smaller than the chemical time scale, thus the combustion process is controlled by the chemical kinetics and because of this the classical flame front does not exist. This type of combustions is often used to investigate the effects of turbulence has on chemical kinetics. Figure 2.20 shows the DNS of well-stirred reaction.

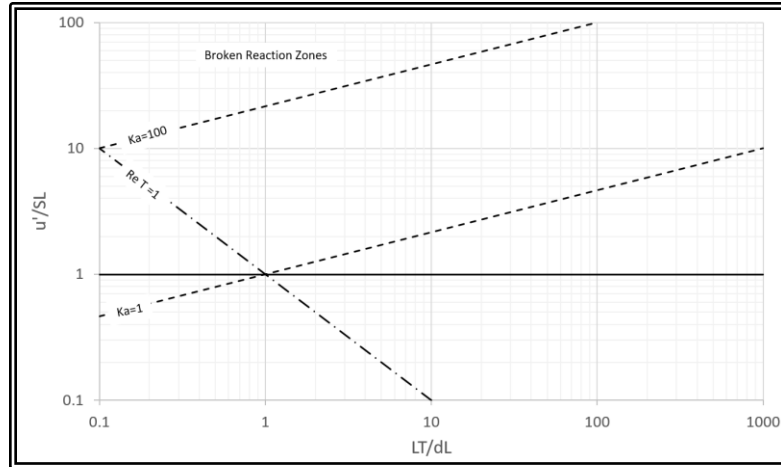


Figure 2.20: Distributed Flame Regime (Broken Reaction Zones) location on the Borghi-Peters diagram

2.6 Laser Diagnostics in Turbulent Combustion Studies

Table 2.2 summarizes the extensive research that has been conducted on flame studies utilizing laser diagnostics [53 - 65]. The table provides a select amount of studies from 2005 to 2016, and provides the title of the research study along with relevant research goals that align to the interests of the presented work.

Table 2.2 A summary of relevant research to the presented work regarding laser diagnostics.

Publication	Goal of the research
Simultaneous CH-OH PLIF and stereoscopic PIV measurements of turbulent premixed flames (2005)	Investigate local flame structures of turbulent premixed flames in the corrugated flame regime.
Measurement of Conditional Velocities in Turbulent Premixed Flames by Simultaneous OH PLIF and PIV (2006)	Turbulent flux of the mean reaction progress variable (corrugated flame regime).
Simultaneous OH-PLIF and PIV measurements in a gas turbine model combustor (2008)	Stabilization mechanisms of swirl-stabilized flames
Simultaneous high-speed PIV and OH PLIF measurements and modal analysis for investigating flame-flow interaction in a low swirl flame (2012)	Investigation of flame/flow interactions in detail (laminar flamelet regime)
Premixed flame propagation in turbulent flow by means of stereoscopic PIV and dual plane OH-PLIF at sustained kHz repetition rates (2013)	Measure local three-dimensional displacement velocity of an unstabilized, freely propagating flames passing through a premixed flow of methane air

Fiber-coupled, 10kHz simultaneous OH planar laser-induced fluorescence/particle-image velocimetry (2013)	Development of a dual system through optic fiber system.
Flame front/turbulence interaction for syngas fuels in the thin reaction zone regime: turbulent and stretched laminar flame speeds at elevated pressures and temperatures (2013)	Experimentation of different fuels to characterize turbulent flame speeds and stretch laminar flame speeds in the thin reaction zone. Recirculation-stabilized flames were used
3 kHz PIV/OH-PLIF measurements in a gas turbine combustor at elevated pressure I.Boxx, C. Slabaugh, P. Kute, R.P. Lucht, W. Meier (2014)	Studied the feasibility of acquiring simultaneous PIV/OH-PLIF measurements at multi kHz rates (3kHz)
High-speed tomographic PIV and OH PLIF measurements in turbulent reactive flows Bruno Coriton, Adam M. Steinberg, Jonathan H. Frank (2014)	Demonstrate feasibility of high-speed tomographic PIV measurements at high kHz levels
Simultaneous 5kHz OH-PLIF/PIV for the study of turbulent combustion engine conditions (2015)	Reported on experimental challenges under high thermal loads at 5kHz

Investigation on rapid consumption of fine scale unburned mixture islands in turbulent flame via 10 kHz simultaneous CH-OH PLIF and SPIV (2015)	Studied turbulent jet premixed flames on the corrugated flame regime
Characterization of multi-jet turbulent flames in cross flow using stereo-PIV and OH-PLIF Anthony Oswaldo Roque Ccacya, Luis Fernando Figueira da Silva (2015)	Study conducted to validate ground flares (smoke stacks) when flame liftoff and flame/surface interactions occur
Experimental study of the inverse diffusion flame using high repetition rate OH/acetone PLIF and PIV A.M. Elbaz, W.L. Roberts (2016)	Studied structure of methane inverse diffusion flames and its feasibility on domestic implementation

From Table 2.1, it can be seen that kHz level studies start making a more prominent appearance in 2013, and while there are studies conducted on the thin reaction flame regime, most studies land in the corrugated flame regime. It can also be appreciated the deep interest current research has on utilizing the laser technology to conduct flame and flow studies.

Based on the presented literature review, this study aims to contribute to the further understanding of the thin reaction flame regime by providing the critical values needed to evaluate the turbulence nature of the flow. An experimental setup has been built with the capability to reach the proposed flame regime at flowrates ranging from 9.5 to 102 m/s, or from $Ma=0.03$ to 0.3 , and is further discussed in the next chapter.

Chapter 3: Experimental Setup

3.1 System description

The design of the turbulent combustion system utilized for this work has been discussed previously [5]. As previously mentioned, the current system is to be operated with air and methane as reactants in order to study combustion at compressible flow rates ($M > .3$). The system requirements that drove the design of this system, can be seen in Table 3.1. The main combustor is shown in Figure 3.1, and consists of the following; combustion chamber, entrance and exhaust regions, mixing chamber, quartz windows, and modular backward-facing step. The other subsystems are discussed in detail in the following sections to provide an understanding behind the overall design of the high turbulent intensity system.

Table 3.1 System Requirements

System	Requirement
Combustion chamber	Optically accessible
	Grid turbulence generator
	Changeable step size (variable dimension)
	Max Pressure: 6 bar (87 psi)
Reactants	Air / CH ₄
Air	Pre-heated at 400-600 K (260 – 620 F)
	Velocity Mach > 0.3
	Flow rate: Max at 0.4 kg/s
CH ₄	Flow rate: Variable (max 0.07 kg/s)
Inlet pressures	100 - 600 kPa (14 - 87 psi)
U/S_L	5-10
L_T/δ	50-200

The design of the entrance and exhaust regions is based on a polynomial profile curve which allows for the entrance and exhaust of the combustor to follow a uniform ‘top hat’ velocity profile [66]. Extensive FEA and CFD modeling has been performed on this subsystem to validate the design and ensure it can meet the system requirements, while also maintaining the safety of those operating it. The FEA analyses were conducted under maximum chamber pressure of 6 bar and maximum temperature of 500K. Table 3.2 shows the subsystem components and their respective factor of safety (FOS), which shows that the probability of a failure mode to occur is at the windows, more specifically the top window. In order to address this, the thermal expansion is considered when choosing a gasket for the combustor windows and flanged unions. The chosen gasket material is a homogenous high temperature application graphite gasket sheet. This gasket material can withstand up to 6000K at a pressure of 10 bar, which is well above the maximum conditions the system will operate at. This gasket material also has a 40% compression ratio with 20% recovery factor, which offers the desired dimensions once thermal expansion is considered along the largest stainless steel to quartz interface. A perforated plate, or grid, is used to generate turbulence as described in Chapter 2. An exploded view depicting the combustor design is presented in Figure 3.1 and the placing of this grid is shown in Figure 3.2.

Table 3.2: Components in combustor and their factor of safety

Component	FOS
Window (thinnest)	3.5
Entrance/Exhaust section	11.8
Grid	16.8
Combustor	12

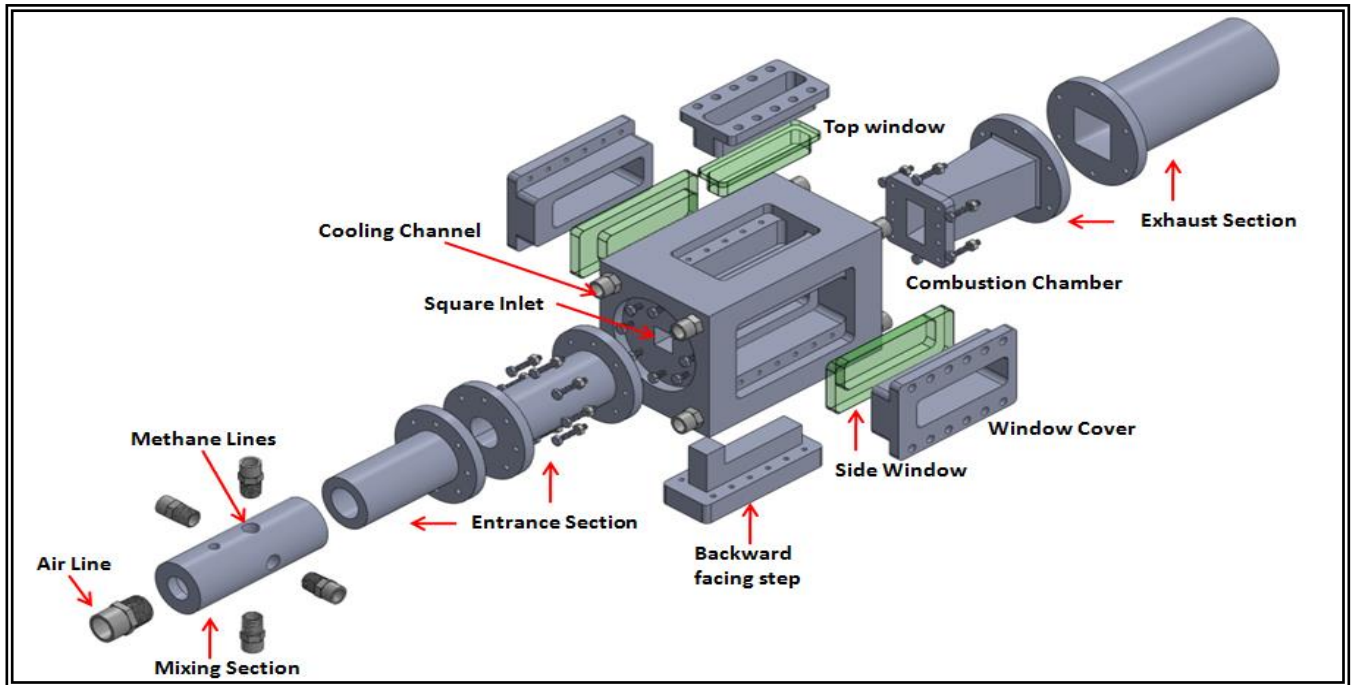


Figure 3.1: Exploded model of the combustor subsystem and its components

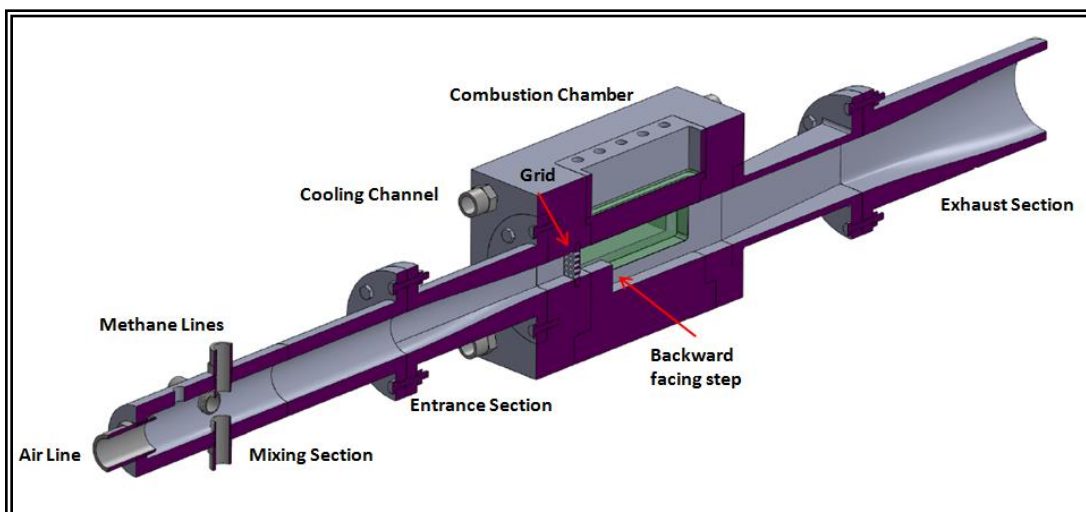


Figure 3.2: Cross-sectional view of the combustor showing 2D plane used in simulations

The combustor design is meant to be fully modular as to investigate different geometrical configurations that might be of interest. The design can accommodate for variable window thicknesses, different step geometries, different entrance sections, and different perforated plate configurations.

The main air line consists of 1" 316 Stainless Steel tubing which draws air from a compressor that can operate at 190 scfm and 140 psig. This flow rate allows the experiments to be conducted at near compressible air conditions. Sizing, pressure, density, and Mach number calculations were carried out using compressible flow theory [67]. An overall schematic of the system can be seen in Figure 3.3. It also shows the pilot flame subsystem, which will serve as the ignition source for the flame in the combustor, in greater detail. This pilot flame subsystem operates using a hydrogen-air premixed flame integrated into the modular step. The pilot flame is ignited using performance sparkplugs with modified electrodes which cause the electric arcs to be at the top of the step surface. The sparkplugs are powered by a 12V automotive grade battery and controlled with automotive grade coils wired to a TTL 5V signal generator. The fuel gases are delivered to the combustor from k-bottles at a regulated pressure of 70 psig. The flow is controlled utilizing quarter turn manual valves, solenoid valves, and manual metering valves. A Bank of calibrated digital flow meters is used to measure the flow rate. The combustor has been designed as to have a cooling system incorporated with dynalene as the working fluid. The exhaust is also cooled down to room temperature before entering the facilities exhaust system.

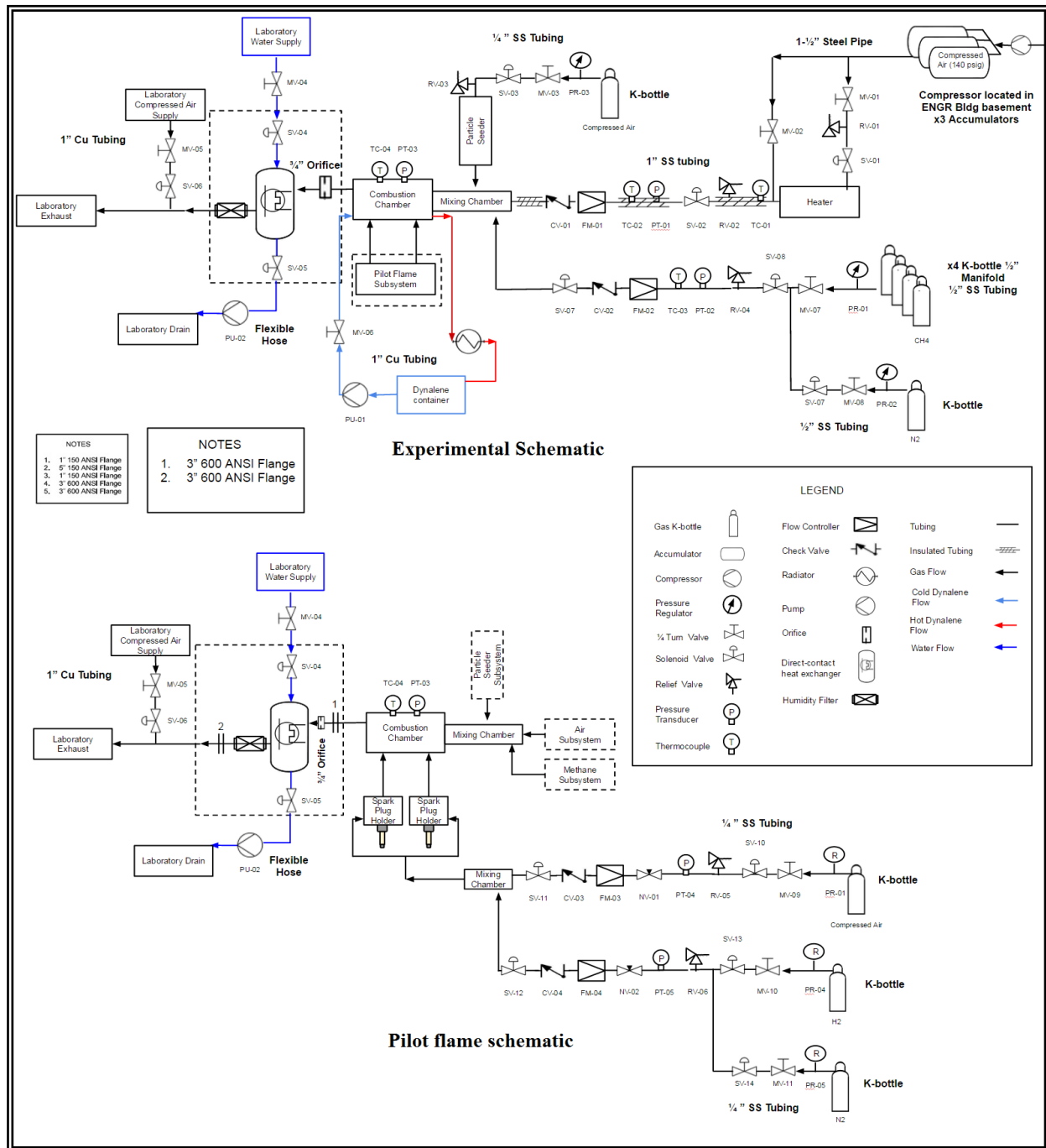


Figure 3.3: Flow schematic of the combustion system and detailed pilot flame flow schematic

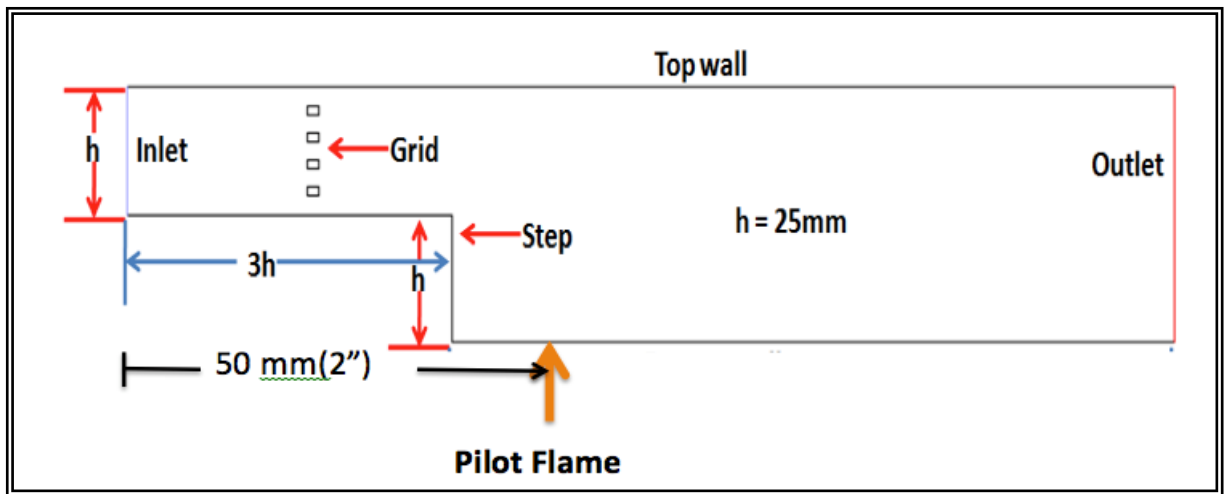


Figure 3.4: Combustion chamber showing location of pilot flame

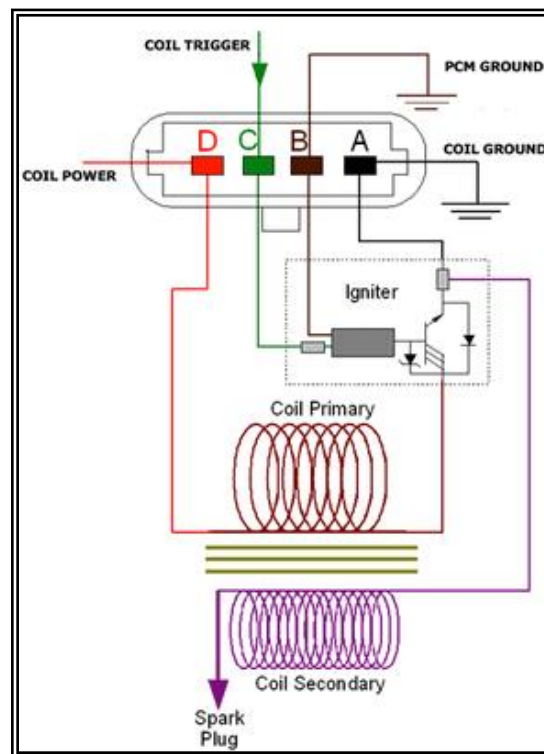


Figure 3.5: Coil wiring diagram

3.2 Exhaust Design

The exhaust design was developed to meet the temperature requirement of exhaust gases not exceeding temperatures of 80 °C. The exhaust fan inside the laboratory has a suction capability of 230 SCFM, which is above our maximum operating conditions. The exhaust temperature of the air is assumed to be 800K at maximum operating conditions based on preliminary combustion modeling [5]. The exhaust cooling method consists of water spraying inside a non-oxidizing tank, which acts as a heat exchanger. The water is sprayed with the use of a commercially available nozzles, with a 90° full cone spray angle (Figure 3.6). The water supplied by the water connections in the laboratory is 17±3 gallons per minute (gpm), and the water pressure is 70±5 psi. The spray nozzle is designed to supply 13 gpm of water at a supply pressure of 70 psi, and consists of a 0.31” orifice diameter.

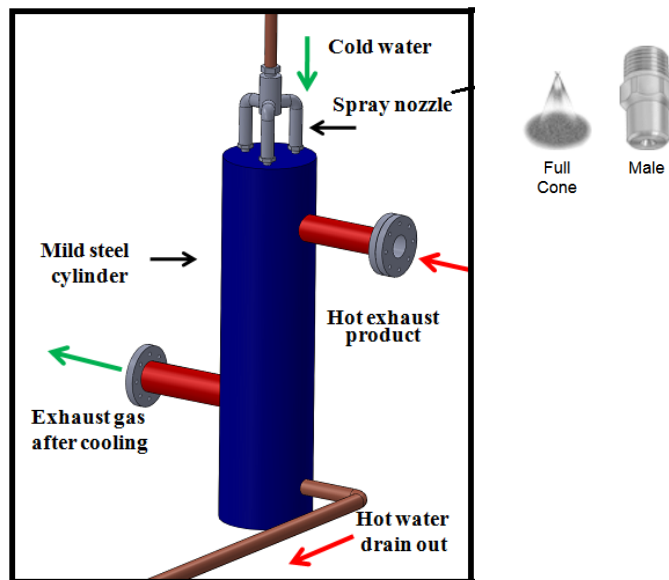


Figure 3.6: Initial conceptual model of exhaust section with spray nozzle diagram

The analysis for the exhaust cooling was done both theoretically and computationally, employing equations of heat transfer, and a multi-phase model. In order to find the amount of water needed, a system of equations is used and includes the mass fraction of liquid water and steam. The equations are solved using the properties of water and steam, as well as the initial temperature of 800K such that-

$$\dot{Q}_{exhaust} = \dot{Q}_{water} + \dot{Q}_{steam} \quad (3.1)$$

$$(\dot{m}c_p(T_{h2} - T_o))_{exhaust} = (\dot{m}_{liquid}c_p(T_o - T_{water}))_{water} + (\dot{m}c_p(T_{vapor} - T_{water}) + \dot{m}h)_{steam} \quad (3.2)$$

$$\dot{m}_{water} = \dot{m}_{liquid} + \dot{m}_{steam} \quad (3.3)$$

The computational model used the result of the mass of water from the previous equations at a temperature of 293K, and pressure of 70 psi. The total mass of the products of combustion at 800K and ambient pressure is used. A transient, multi-phase turbulent k-ε model was used to carry out the simulation with dimension of the spray nozzle and water tank as specified by the manufacturer. The model was run using ANSYS 14.1 Academic version with a total of 200000 elements. The results are shown in Figure 3.7, and the results of the computational temperature compared to the theoretical value are presented in Table 3.3. The minimum water flow rate required to cool the exhaust gas is 7.5 gpm, which is less than the maximum flow provided by the spray nozzle. A pump is used in order to drain the accumulated water out of the tank at a flow rate higher than the nozzle. A supplementary dilution line was also added to the exhaust in case an unburned mixture entered the exhaust.

Table 3.3: Comparison between theoretical and CFD results

Theoretical exhaust temperature	CFD mean temperature
333K	340K

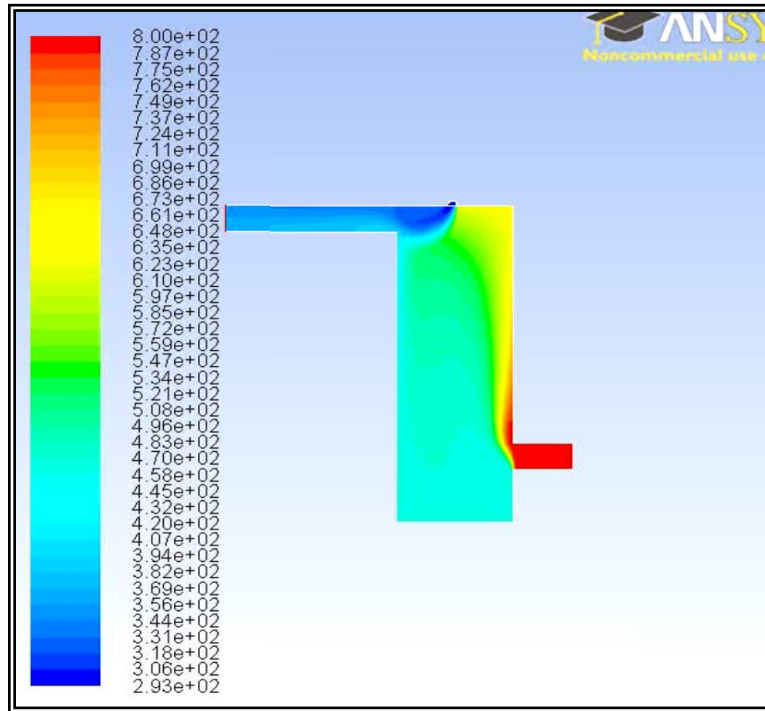


Figure 3.7: Temperature contours in exhaust simulation

3.4 Combustion Chamber Cooling

As temperature rises inside the combustor during experimentation, the structural integrity of the combustor subsystem is compromised, and running time becomes an important issue, and as discussed previously, the windows present the main form of failure. To address the rising temperature of the combustor body and keep the thermal expansion from happening, a heat

exchanger was rerouted to flow coolant through the combustor. Figure 3.8 illustrates the conceptual and actual setup of the heat exchanger. Figure 3.9 shows additional information about the heat exchanger which can supply a cooling load of 200kW. Cooling channels were manufactured into the combustor. These cooling channels are 9.5” long, have a 0.5” diameter and there are 4 channels in total. These channels flow dynalene HC-10, a non-toxic coolant, at a rate of 5.6 – 10 gpm. The properties of this coolant are obtained from the manufacturer. The temperatures at different critical points in the combustor were calculated using equations for transient heat transfer on a convective surface [68]. These calculations are used with the log mean temperature difference method (LMTD) calculations associated with the coolant flow inside the combustor channels.

$$\dot{q}_s(t) = h[T_\infty - T(0, t)] \quad (3.4)$$

$$\frac{T(x, t) - T_i}{T_\infty - T_i} = \operatorname{erfc}\left(\frac{x}{2\sqrt{\alpha t}}\right) - \exp\left(\frac{hx}{k} + \frac{h^2 \alpha t}{k^2}\right) \operatorname{erfc}\left(\frac{x}{2\sqrt{\alpha t}} + \frac{h\sqrt{\alpha t}}{k}\right) \quad (3.5)$$

$$\Delta T_{ln} = \frac{\Delta T_e - \Delta T_i}{\ln\left(\frac{\Delta T_e}{\Delta T_i}\right)} \quad (3.6)$$

These equations were solved for different flow conditions inside the combustor and inside the cooling channels to find a relationship between the coolant and the temperature at certain thicknesses of the combustor walls. Equation 3.5 is also applied to the quartz windows in order to calculate the difference in thermal expansion of the stainless steel and quartz interfaces [69].

$$\frac{\Delta L}{L_o} = \alpha \Delta T ; \quad \frac{\Delta A}{A_o} = 2\alpha \Delta T ; \quad \frac{\Delta V}{V_o} = 3\alpha \Delta T \quad (3.7)$$

Comparing the thermal expansion differences using the temperatures from Figure 3.10, the adequate gasket sizing was chosen to be 1/16" thickness.

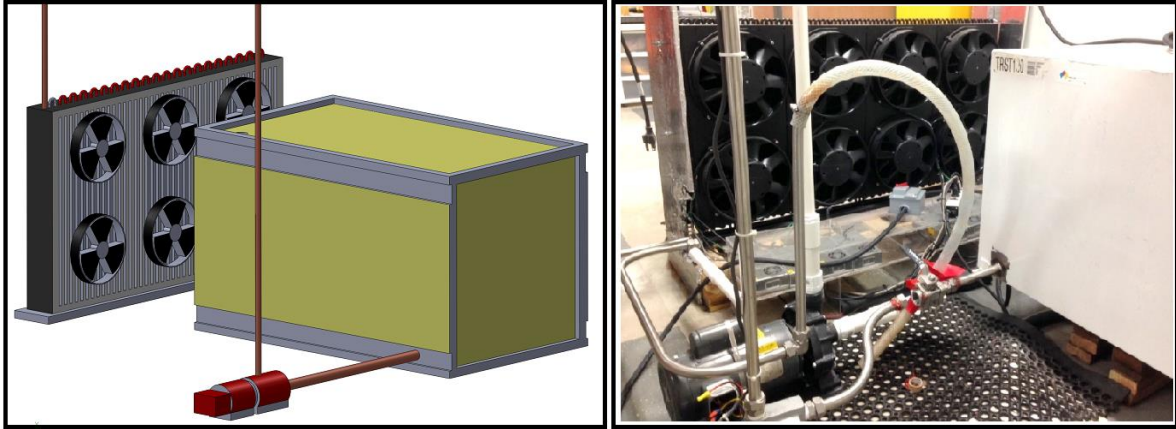


Figure 3.8: CAD model of heat exchanger and dynalene tank (left) and physical setup (right)

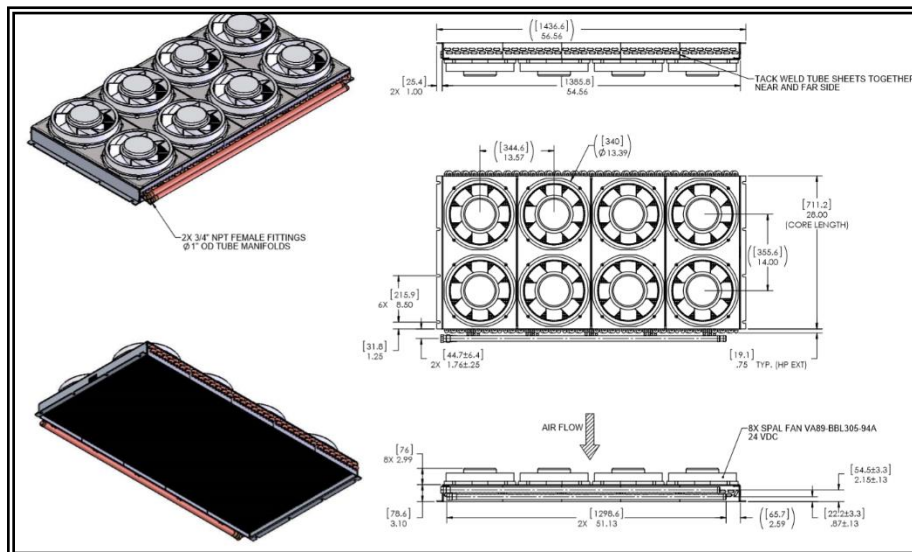


Figure 3.9: Additional schematic of heat exchanger used for cooling

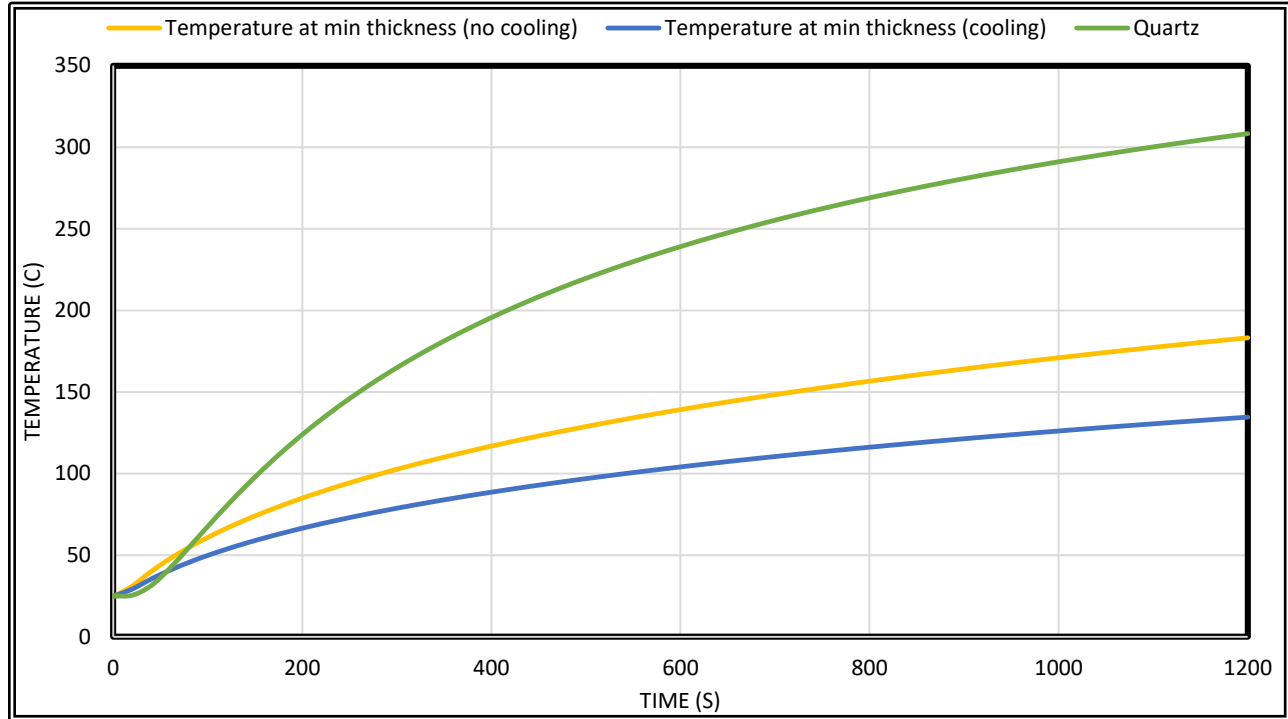


Figure 3.10: Temperature vs time plots for critical thickness and largest quartz window

Using the thermal expansion of stainless steel and quartz with Figure 3.10, the determined allowable temperature is 125 °C. The allowable run time is doubled when the combustor is being cooled with the dynalene.

3.5 Control System

The control system setup was designed with two objectives in mind; to be able to control all the instrumentation manually as well as automatically through the use of LabVIEW with National Instruments PCI cards, and to be efficient and simple to operate and record data. In order to achieve this, all instrumentation was wired into a single station consisting of:

- Main control box with connector blocks attached which controls:
 - AC valves

- DC valves
- Manual emergency stops
- Spark plug ignition
- DC power supplies for valves and instrumentation (thermocouples, transducers)
- LabVIEW designated CPU for running automated sequences
- Signal generator for pilot flame ignition

The control box is shown in Figure 3.11 and the corresponding electrical schematic is shown in Figure 3.12. There are two separate manual emergency stops in the control system; one for all gas controlling valves, and one for water controlling valves. The control box also consists of a double pole-double throw (DPDT) switch which serves as a manual override in case of a CPU or software malfunction. The LabVIEW program consists of four Data Acquisition assists to accommodate for the different signal each type of instrumentation requires. Table 3.4 presents what each DAQ assist controls. The LabVIEW interface and block diagram are shown in Figure 3.13 and 3.14 respectively.

Table 3.2: DAC controlled instrumentation

DAQ Assist	Instrumentation controlled/monitored
1	Pressure transducers, flowmeters, and thermocouples
2	Air/methane line valves
3	Air and methane proportional control valves
4	Pilot flame valves



Figure 3.11: Main control box

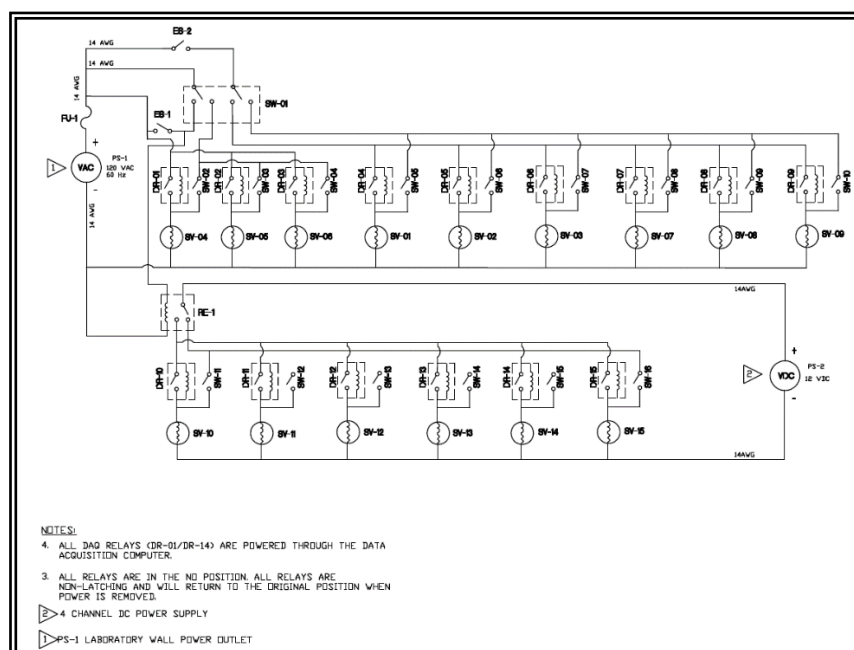


Figure 3.12: Electrical schematic of main control box

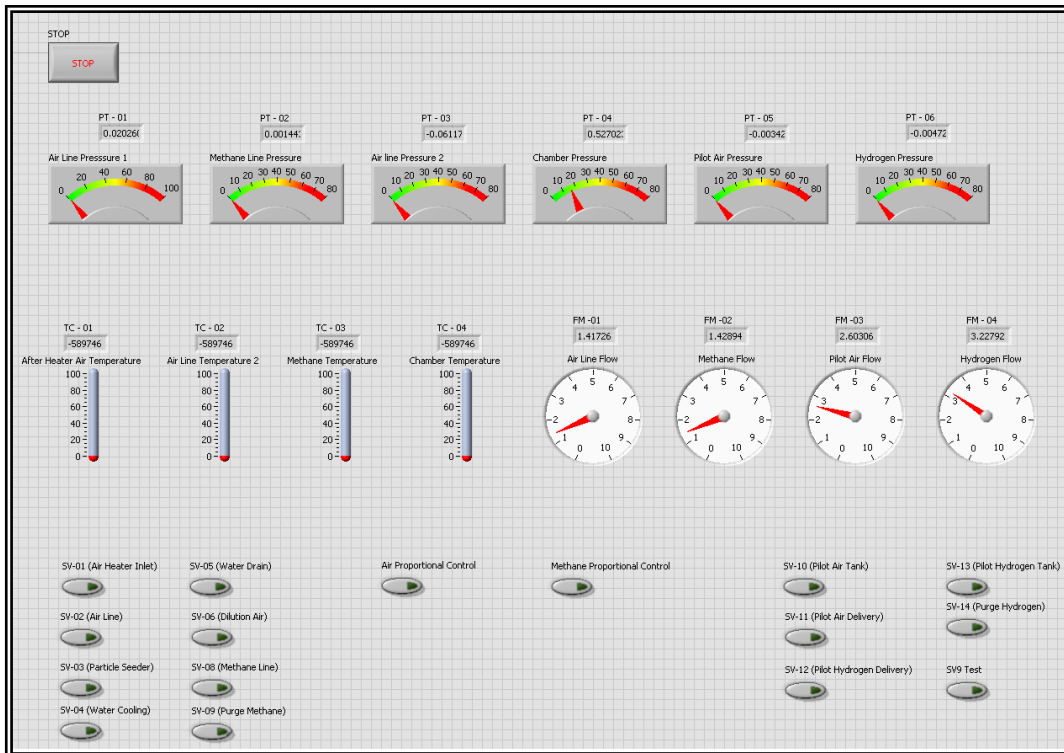


Figure 3.13: LabVIEW control panel interface

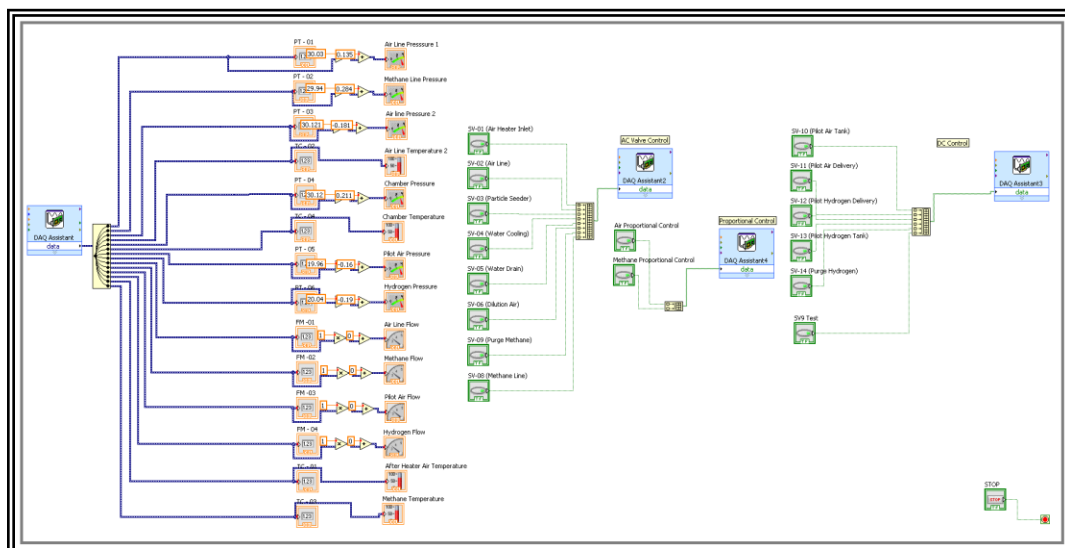


Figure 3.14: DAQ assist block diagram

3.8 Test Setup Summary

To summarize, the system can be described using Table 3.5. The subsystems and their function are explained.

Table 3.3: A summarization of the subsystems that make up the high turbulent intensity system

Subsystem	Function
Combustor	Provides optical access in order to employ flow diagnostic techniques and study the previously mentioned research topics
Main air line	Provides cold/preheated air to the combustor for premixed flame combustion
Pilot flame	Ignition source for the air and methane reactants inside the combustion chamber
Methane line	Provides methane to the combustor for premixed flame combustion
Exhaust	An exhaust which serves as an escape which cools the hot combustion products to a safe and acceptable temperature
Chamber cooling	Cools the combustor in order to prolong combustion run time for up to 13 minutes
Control system	Provides manual and automatic control of system instrumentation

PIV system	Laser diagnostics system used in the present work to characterize the turbulence scales of air at compressible conditions
PLIF system	Laser diagnostics system that allows the analysis of flame front characteristics.

Now that an understanding of the experimental setup used has been provided, the approach used to conduct the measurements to achieve the goals of the work presented will be overviewed.

Chapter 4: Methodology

The present work focuses on the study of turbulent structures in the flow field at near compressible flow conditions. Figure 4.1 presents the schematic diagram pertaining to the setup used for the current work.

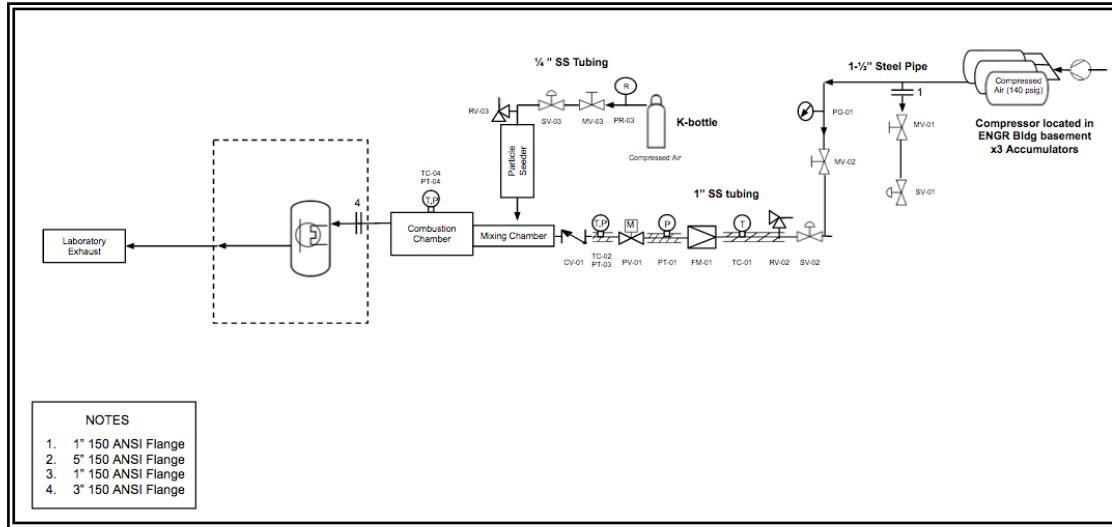






Figure 4.1: A simplified flow schematic of the presented work taking Figure 3.3 as a base line

A test matrix has been developed and different turbulence generators with different blockage ratios have been manufactured for testing. The selected hole diameters and blockage ratios will allow to conduct a study of the flow characteristics within the combustor and investigate the effects of hole diameter, blockage ratio, and flow rate on flow characteristics. Table 4.1 summarizes the test matrix utilized for this study, and Table 4.2 summarizes the turbulence generators utilized.

Table 4.1: Test matrix utilized for the presented work

Bulk V (CFM)	Air V (CFM)	Bulk u (m/s)	Mix Re	Ma	Air Re
13	12	10	15,000	.03	14,000
27	25	20	32,000	.06	30,000
54	50	39	64,000	.11	60,000

Table 4.2: Blockage ratio (BR), and hole diameter (HD) of the tested perforated plates

Grid #	BR	HD (mm)	HD (in)	
1	48%	1.5	1/16	
2	46%	3	1/8	
3	63%	1.5	1/16	
4	62%	3	1/8	

As discussed previously on the experimental setup sections and the introduction, particle image velocimetry has been used to characterize the flow and generate the components of turbulent intensity and turbulent kinetic energy. Before the tests are conducted, the laser being utilized as a light source, and the high speed CCD cameras are synchronized utilizing a BNC 575-8 timer box. For the present work, the post processing and cross correlating algorithms used are the ones included in the Dantec Dynamics' Dynamic Studio software.

In order to conduct the particle imaging velocimetry experiments, a '15-1000 Dual Power' Neodymium-doped Yttrium Lithium Fluoride (Nd-YLF) laser with a pulse energy of 15mJ was used. It is desired to have the light source perpendicular to the camera position, so the laser light enters the combustor from the top window. In order to achieve this the laser head is placed at an elevated position, and the light is re-directed at a 45^0 into the laser sheet optics. After the beam travels through the optics a 1 mm x 52 mm x 25 mm laser sheet is generated as depicted in Figure 4.2.

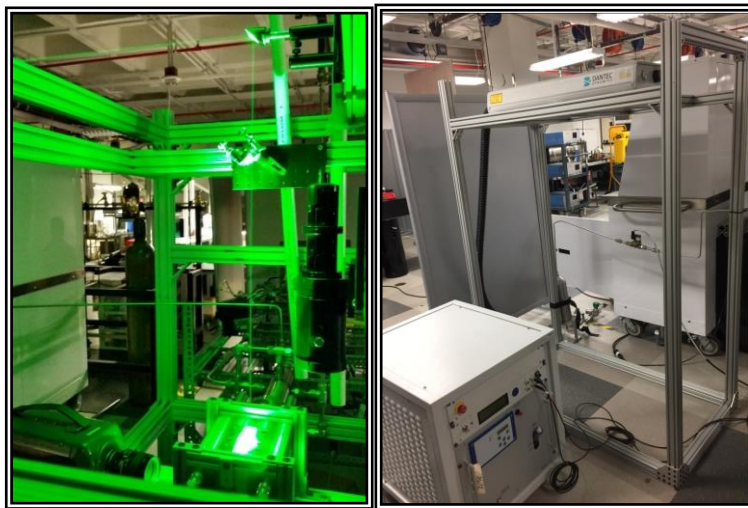


Figure 4.2: PIV beam path into the combustor and raised laser head

This laser sheet will illuminate the 1-micron alumina particles utilized to trace the flow, injected far upstream to where the introduction of particles does not affect the cross-flow development. The particles are sent using dry air as a carrying medium and the flow is controlled using a manual and solenoid valve as presented in Figure 4.1. The light scattered by the particles is then captured with a Speed Sense 9070 CCD high speed camera with a frame rate of 10kHz with a resolution of 598x288 pixels or an interrogation area of 73 x 35 mm at 12 bits. The camera and the laser pulses are synchronized through BNC cables connected to a BNC-575-8 timer box. The software used to synchronize the devices and post process the data is Dantec Dynamics' Dynamic Studio.

The main air line is controlled by three different valves. A quarter turn manual control valve is used to allow air to enter the main airline into the system from the compressor mentioned in chapter 3. The air passes through a 120 V AVCO E03/05 8P14 solenoid valve. After that the air flow is set using a manual valve. The flow is measured through an analog flow meter (Hedland variable area flowmeter) which has a flow measurement range of 25 – 250 scfm and a pressure range of 40 – 120 psi with $\pm 2\%$ accuracy. The location of the equipment on the main airline is presented in figure 4.1.

Figure 4.3 presents a typical PIV setup and the working steps taken from Dantec Dynamics' website.

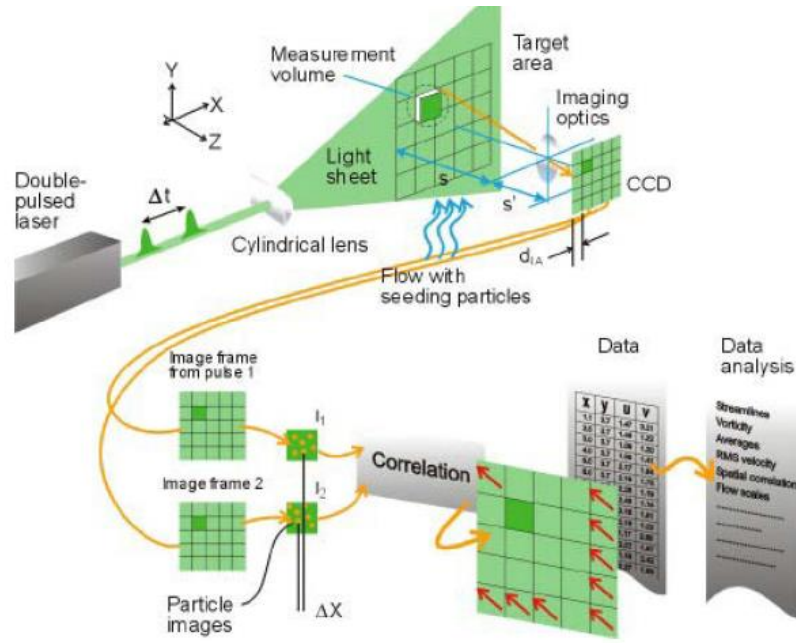


Figure 4.3: PIV process

It can be seen in Figure 4.3 what the steps are to generate the velocity fields through PIV using the most basic definition of velocity, distance traveled divided by time. The flow is seeded with light scattering particles. A double pulsed laser is used to generate two different light pulses separated by a known difference in time. The laser beam is sent through a cylindrical lens generating a light sheet that illuminates a plane in the area of interest. The light from the laser reflects off the particles and is recorded by a high speed camera. The camera and the laser are both synchronized as to have the camera collect the two instances generated by the two laser pulses. The two images are then post processed and divided into subsections called interrogation areas. Each interrogation area is then analyzed using a cross-correlation algorithm in order to find the average direction in which the particles are moving in each interrogation area. The software does a cross-correlation in all the interrogation areas the total image is sub-divided into and a vector field is then acquired from it. Once the velocity vector field is acquired, the data can undergo

further post-processing to acquire vorticity, turbulence intensity, amongst many other different analyses.

In order to form a correlation between pixel values, and physical dimensions the setup has to be calibrated using a scale that is positioned where the laser sheet is. The Dynamic studio utilizes a scale factor that is used to determine the converting factor from pixel into metric units. This factor represents the magnification of the lens system, which calls for the need of the physical size of a pixel element, or pixel pitch. The formula is:

$$\text{Dimension (mm/pixel)} = \text{Scale Factor (1/pixel)} * \text{Pixel Pitch (mm)}$$

Figure 4.4 presents a sample image used to measure the scale factor for the work presented here.

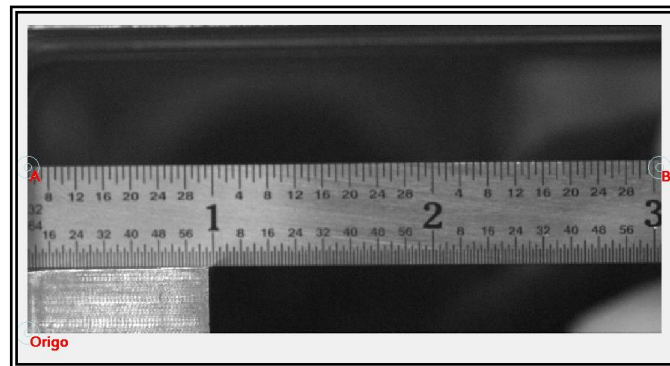


Figure 4.4: Sample image of a calibration target used to define the PIV scale factor

From Figure 4.4, the “Origo” marker determines the location of the origin used to make the vector field map calculations, and denotes the (0,0) position of the coordinate system used. The position can be freely picked, for the presented work, the origin was set at the lower left corner of the image. Markers A and B determine the scale factor. The markers are positioned at identifiable positions in the image where a known distance is being captured by the camera within the field of

interest, or interrogation area. Precision of the calculated scale factor is proportional with the distance between reference marks of A and B. This translates to better PIV resolution with a large distance between the reference markers. A raw sample image of the seeded flow is presented in Figure 4.5.

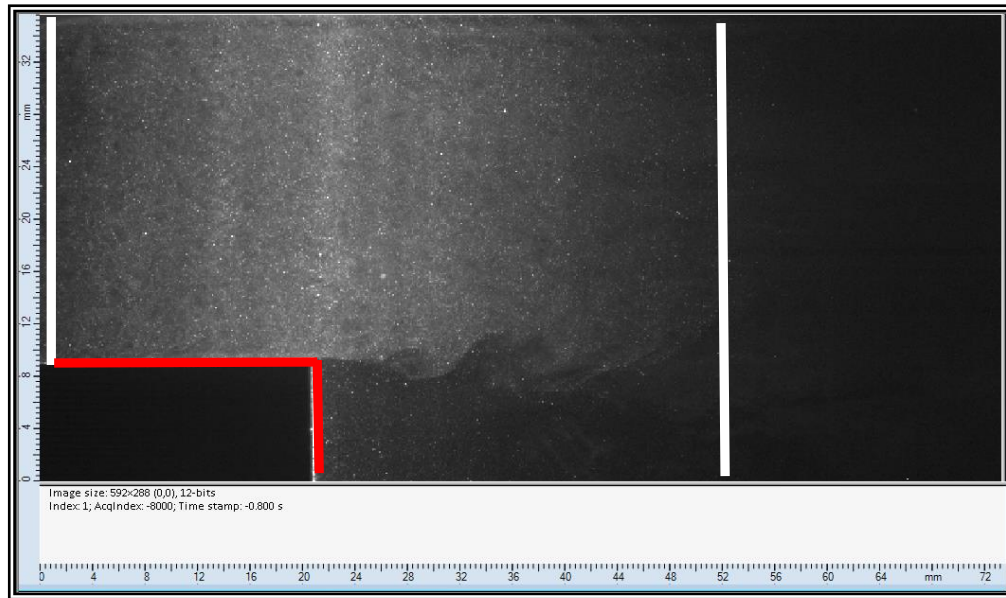


Figure 4.5: Sample image of the seeded flow with the mill metric scale displayed. Red line outlines the step location and white lines delineates the light sheet location.

The main air line is controlled by three different valves. A quarter turn manual control valve is used to allow air to enter the main airline into the system from the compressor mentioned in chapter 3. The air passes through a 120 V AVCO E03/05 8P14 solenoid valve. After that the air flow is set using a manual valve. The flow is measured through an analog flow meter (Hedland variable area flowmeter) which has a flow measurement range of 25 – 250 scfm and a pressure range of 40 – 120 psi with $\pm 2\%$ accuracy. The location of the equipment on the main air line is presented in figure 4.1.

4.1 Particle Image Velocimetry (PIV)

This section is dedicated to go into detail regarding PIV as it is used extensively throughout the combustion community to characterize the flow of interest. Due to its non-intrusive nature, PIV is a robust and efficient way to define and identify the flow characteristics of interest. While PIV is a complicated flow measuring technique, the main variables that influence the accuracy of the measurement are described in detail here.

4.1.1 SEEDING PARTICLES

Particle image velocimetry or PIV, is a non-intrusive technique used to indirectly measure flow fields through the use of particles entrained in the flow of interest. The measurement's indirect nature comes due to the fact that one is measuring the flow field by using the particles entrained in the flow and not the flow itself. The flow should be seeded with particles small enough to faithfully follow the flow, but large enough that they are able to refract the light from the light source that illuminates them [70].

A disadvantage of having solid particles as tracers, is that they must faithfully follow the flow and must generate the drag force needed to follow the fluid acceleration. Due to this reason, particle markers are a popular choice in PIV applications.

Durst [71] has calculated the optimum size of the seeding particles by solving equations of particle motion yielding the frequency response of particles of different sizes. The conclusions from Durst reveal that 1 μm particles are able to reach a frequency response of 10kHz while particles of 10 μm can reach frequency responses below 1kHz. For this work 1 μm particles are used as they are able to reach a frequency of the laser and camera frequency used of 10 kHz.

4.1.2 LASER TYPE

As discussed previously, there is a compromise when selecting seeding particle size. While smaller particles are better at faithfully following the flow, they are not good light scatters, and while larger particles are able to scatter light easily, they tend to lag behind the flow field's accelerations resulting in the particles not being able to follow the flow faithfully. The laser light source used can alleviate this compromise.

When conducting a PIV measurement, the illumination source should provide powerful enough to enhance the particle's ability to scatter light, and fast enough to be able to track the movement of the particles with enough resolution to provide accurate measurements. Because of these reasons the most popular choice for PIV applications are laser light sources. The Nd:YLF laser is amongst the most commonly used due to its high energy output, short pulse capabilities, and its light emission wavelength within the visible spectrum at 532 nm [72]. The "15-1000 Dual Power" laser is capable of providing the particles with enough laser power to have the 10kHz frequency response needed to address the highly turbulent nature of the flows encountered in the experimental setup.

4.1.3 IMAGE ACQUISITION

The camera used for the work presented was a Phantom high speed camera v310, paired with a Nikon 60 mm lens. This camera uses a charged coupled device (CCD) which is comprised of 1280 x 800 matrix of metal-oxide semiconductor (MOS) elements. The light scattered by the particles is focused through the lens onto the CCD and a voltage is generated when the light hits

the MOS elements. The camera has a 12 bit resolution. The camera lens is also fitted with a 532 nm light filter to reduce background light noise as presented in Figure 4.6.



Figure 4.6: High speed camera used for the presented work

4.1.4 CROSS-CORRELATION

Cross-correlation is a computational technique used to determine how similar two signal samples are for a given spatial shift. When the signals in the interrogation area are apart by a small difference in time, the images will shift in proportion to their velocity, but remain relatively unchanged. The PIV technique then uses the first image offset in proportion to the true flow velocity which allows the interrogation regions within the two image maps to line up and correlate with one another. The shift in both recorded images and the shift that happens over a known amount of time corresponds to the measured velocity.

The cross-correlation function for two discretely sampled images of the same size $f(i,j)$ and $g(i,j)$ is defined by equation 5.1 [73]:

$$\Phi_{fg}(m, n) = \sum_i \sum_j f(i, j) \times g(i + m, j + n) \quad (5.1)$$

The cross-correlation function is a measure of how closely the two interrogation areas from both of the images captured correlate with one another when offset by a number of pixels (m,n) . The highest number of $\Phi(m,n)$ is taken as the true correlation, and multiplied by the scale factor gives the direction in which, on average, the particles captured within the interrogation region are moving. As the maps need to be shifted by every possible value to determine the highest cross-correlation, a Fast Fourier Transform is used to reduce the computational power needed to post process the data.

4.2 PIV Post Processing Techniques

Now that the basic principles of how the PIV technique works has been covered, this section will describe what post processing was applied to the raw captured images to increase resolution, and condition the signal to give the most accurate vector maps possible.

4.2.1 IMAGE BALANCING

In order to correct the light sheet non-uniformities that affect the outcome of the analysis process, an image balance was applied to the raw image ensemble. This process found as part of the Dynamic Studio software helps with post processing the velocity vector fields by providing a sharper image of the particle locations for a better spatial resolution. The two step process first generates an image balance map that consists of factors determined from an ensemble of images

that is later applied to a set of images to correct for any strong light variations. Figure 4.7 presents the raw image, the image balance map and a sample of the image ensemble that has the image balance map applied to it.

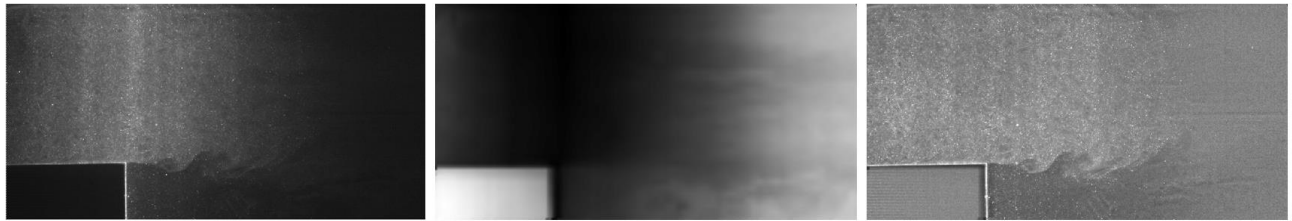


Figure 4.7: Raw image, image balance map, and light balanced image

It can be seen in Figure 4.7 how after the image balance map is applied to the raw ensemble of images, a higher contrast is achieved and the location of particles is easily distinguished.

4.2.2 IMAGE MASKING

In order to black out areas that are not of interest like walls, and to better define the area of interest for the analysis, an image masking is applied. This Dynamic Studio option allows the user to mask out areas that generate random noise, such as strong light reflections, and walls, for the PIV analysis. For the work presented here a masking was used to take advantage of the Adaptive PIV post processing option of “Wall Windowing” to further reduce the generation of spurious vectors. A sample of the masked image is presented in Figure 4.8.

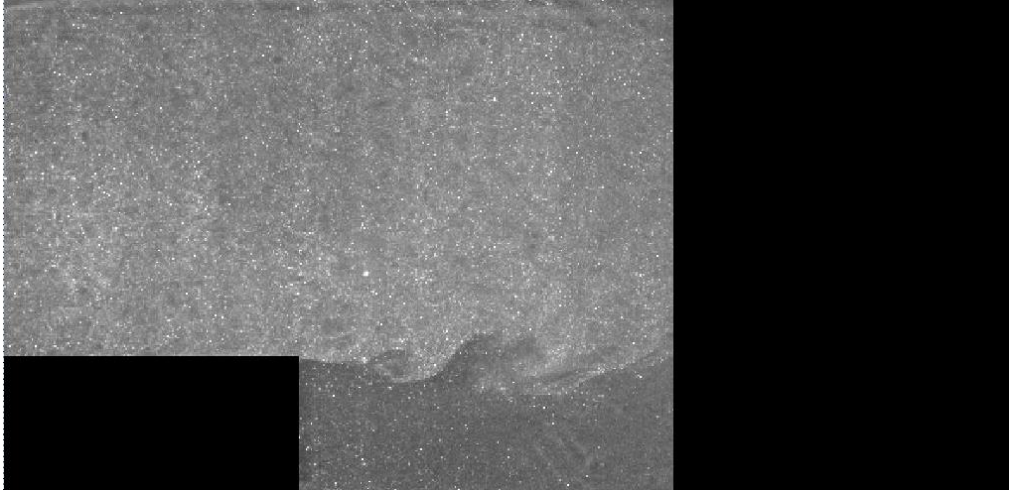


Figure 4.8: Masked raw seeded flow image for PIV analysis

4.2.3 ADAPTIVE PIV

The Dynamic Studio Adaptive PIV method is an automatic and adaptive method for calculating velocity vectors based on particle images. This method iteratively adjusts the size and shape of the individual interrogation areas in order to adapt to local seeding densities and flow gradients. This feature of this particular method comes in handy when trying to resolve the velocity vector field in the shear layer generated in the backward facing step used in the experimental setup. This method also includes options to apply widow functions, frequency filtering as well as validation in the form of Universal Outlier Detection.

For the presented work, a window size of 16×16 was used with a window step size of 4 and a maximum grid size of 64×64 . This means that the software will start off acquiring a correlation using the 64×64 interrogation size while subsequent iterations are allowed to reduce the interrogation size where particle density is high enough to justify it. This process can be

repeated until reaching a minimum grid size of 16×16 . The grid step size defines the spacing between the positions of the interrogation sizes when analyzing the image ensemble and the number of interrogation areas in between the minimum and the maximum defined.

The "Wall Windowing" function is a unique feature to adaptive PIV and it is used in the presented work. This function helps mitigate wall bias. Wall bias is derived due to the nature of how cross-correlation is carried out throughout the image ensemble. There are instances where the interrogation size extends past a wall, velocities and displacement of particles are biased by particles far from the walls that are generally moving faster than those closer to the wall. Wall windowing attempts to mitigate this effect by masking also the particles far from the wall, so remaining particles are symmetrically distributed around the center of the interrogation area.

In order to mitigate outliers from disturbing the iterations and velocity measurements, a peak validation was applied to the correlation. The validation is further supported with a Universal Outlier Detection algorithm which compares each vector being generated to its neighbors.

The adaptive nature of the Adaptive PIV comes very useful in the presented application due to the large velocity gradients present at the shear layer formed at the step edge of the experimental setup. The adaptivity of the PIV was set as to apply it based on particle density on the interrogation size with a particle detection limit of 5 and a desired number of particles of 10 on the interrogation area. The adaptivity of the velocity gradients was also applied with an absolute magnitude of the gradients of 0.1 and a second combined effect of all gradients of 0.2. Figure 4.9

presents a sample image at 12CFM, 70 psi. The color scale depicts the velocity going from 0 to 15 m/s.

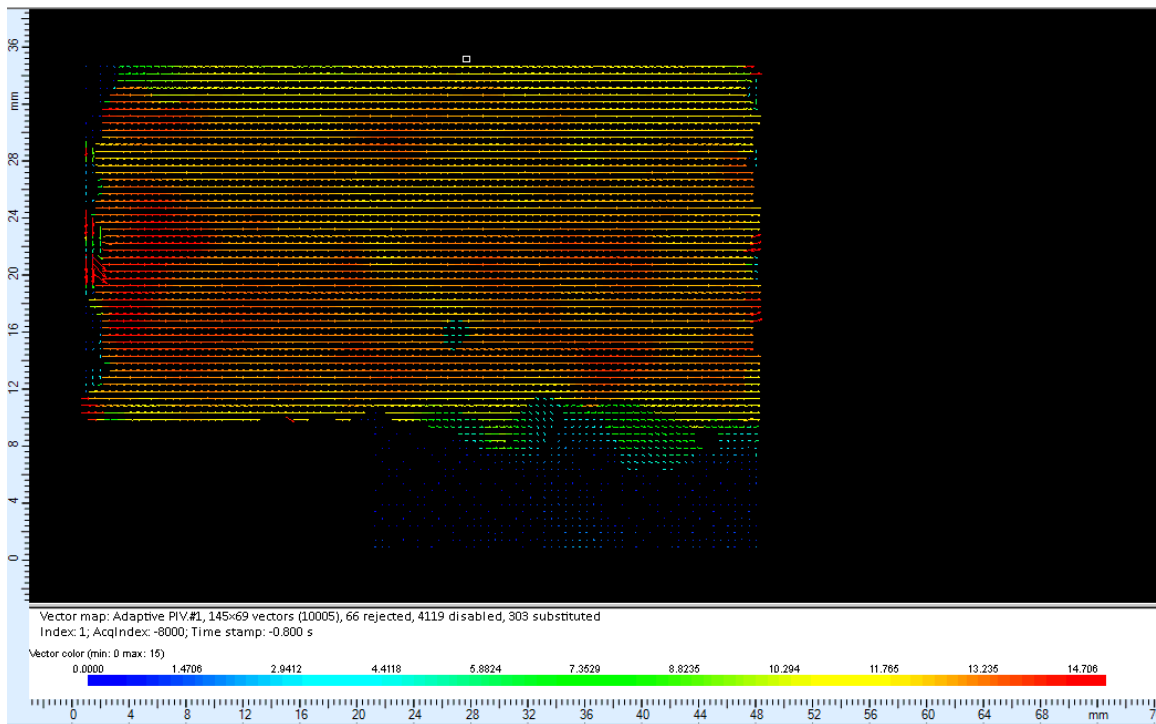


Figure 4.9: Sample PIV vector map of Grid 1 at 12CFM 70psi

Once the vector field map has been acquired it can be further analyzed to extract derived information from it.

The vector statistics tool allows for the calculation of statistics from the multiple vector maps acquired during post processing. While the graphical representation of the vector statistic map appears as the average vector field map, many additional statistical results are calculated as well. Another important tool utilized in this work is the scalar map tool. This function is used for on-screen display of a number of data types. Figure 4.10 presents the turbulence intensity scalar map derived from the results presented in Figure 4.9.

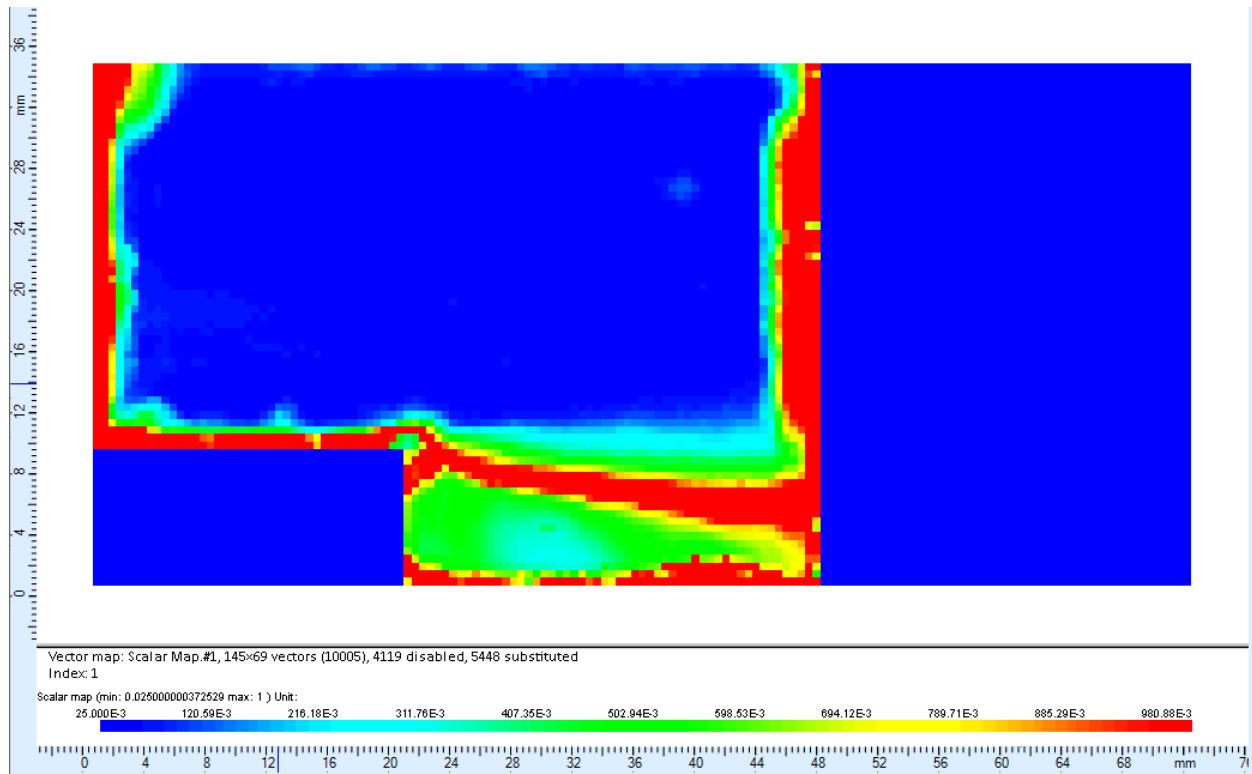


Figure 4.10: Sample turbulence intensity scalar map of Grid 1 at 12CFM 70psi

From Figure 4.10 it can be seen how the highest turbulence intensity is located in the recirculation region generated right after the step edge. This is important to note as a high level of turbulence is needed to mix the fresh fuel mixture with the burned gas mixture to keep the flame anchored in this area.

By taking the curl of the vector we get vorticity. Using this principle for planar data gradients a scalar map can be generated for vorticity levels found in the flow. The software uses the following formula to make the calculations on a 2D vector map.

$$\omega_z = \frac{\partial V}{\partial x} - \frac{\partial U}{\partial y} \quad (5.2)$$

Figure 4.11 presents a sample of a vorticity scalar map generated from the data acquired in Figure 4.9.

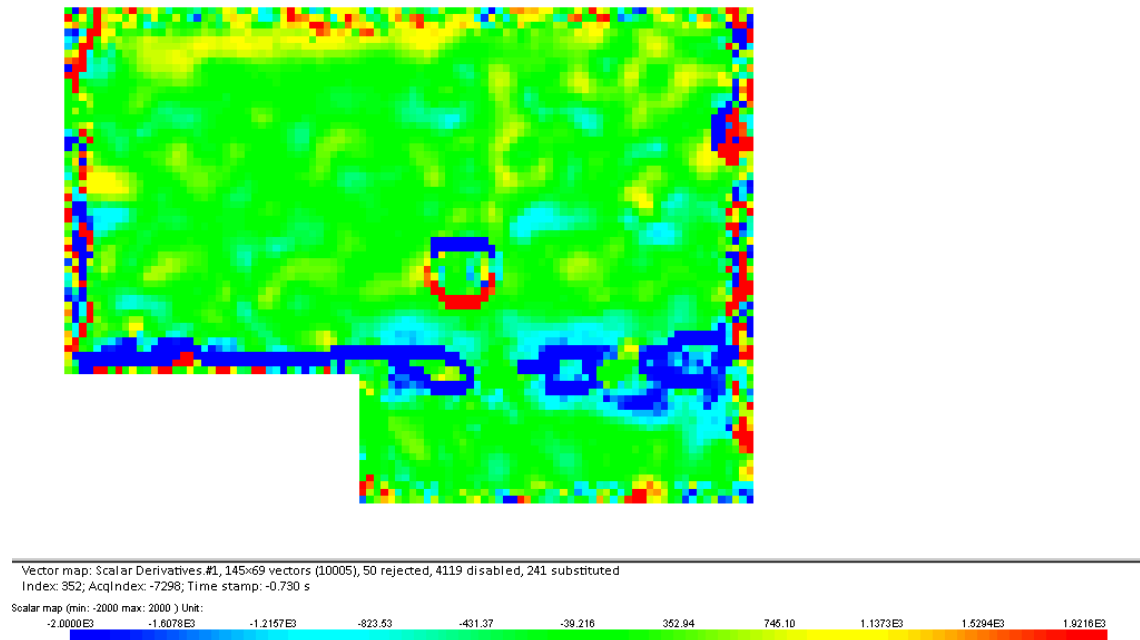


Figure 4.11: Sample PIV vorticity scalar map of Grid 1 at 12CFM 70psi

It is noticeable in Figure 4.11 how there is a strong vorticity generated at the shear layer. It is also possible to resolve eddies within the flow as it can be seen in Figure 4.11.

In order to extract the information from the vector field map we can interrogate the ensemble of vector maps with a static line. The line will then record the velocity at a variety of different points along the line. Figure 4.12 presents the interrogation line along the step edge where

the measurements for the presented work were taken. Figure 4.13 presents a sample plot acquired from the interrogation line presented in Figure 4.12. As discussed previously, while the image of the vector statistics map is the average vector field map, a wide variety of other statistical calculations are done on the ensemble of vector field maps.

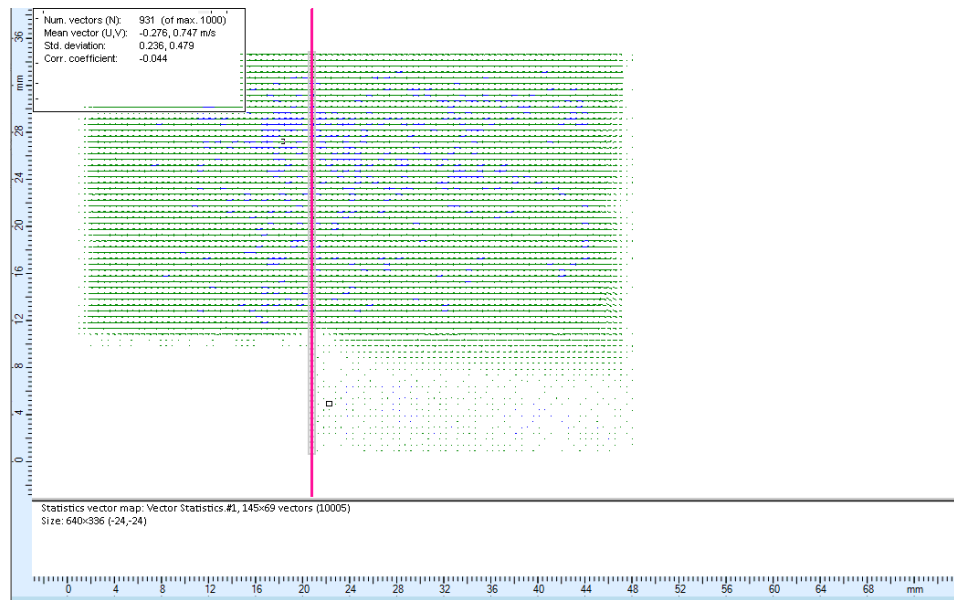


Figure 4.12: Sample image of the interrogation line on the vector statistics map

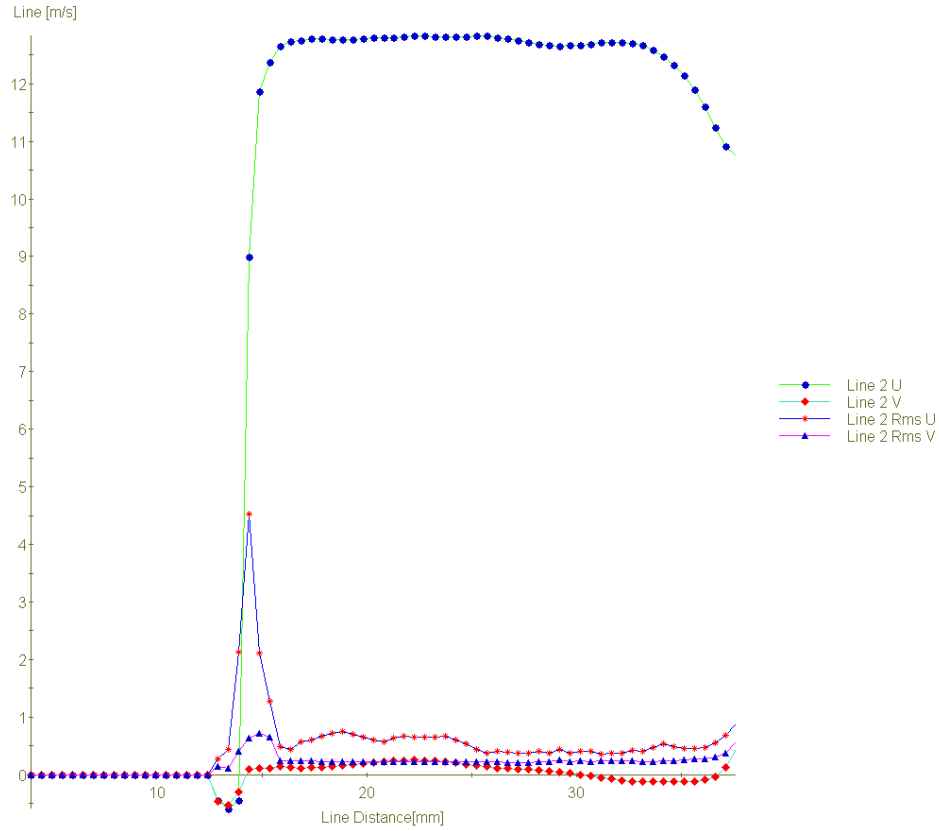


Figure 4.13: Sample plot of the interrogation line on the onset of the combustor step

Figure 4.13 presents a plot of data relevant to the current work. The blue point line presents the u velocity component, the red diamond line presents the v velocity component, the red dot line presents the u_{RMS} and the blue triangle line presents the v_{RMS} .

Another important analytical tool available is the Proper Orthogonal Decomposition (POD). POD is a powerful method that helps obtain low-dimensional approximate descriptions for multi-dimensional systems. The method uses model decomposition and provides a way to capture dominant components of a multi-dimensional system. First a snapshot is taken from a range of vector fields and outputs a graphical representation of the energy decomposition in the flow, from

highest to lowest energy modes. The mean velocity fields are considered the zero'th mode of the POD. Subtracting the mean from all the snapshots, the rest of the analysis operates on the fluctuating parts of the velocity components (u_{RMS} , v_{RMS} , w_{RMS}) where u , v , and w denote the fluctuating part of the velocity component [74]. Figure 4.14 presents a sample POD snapshot of the velocity vector field.

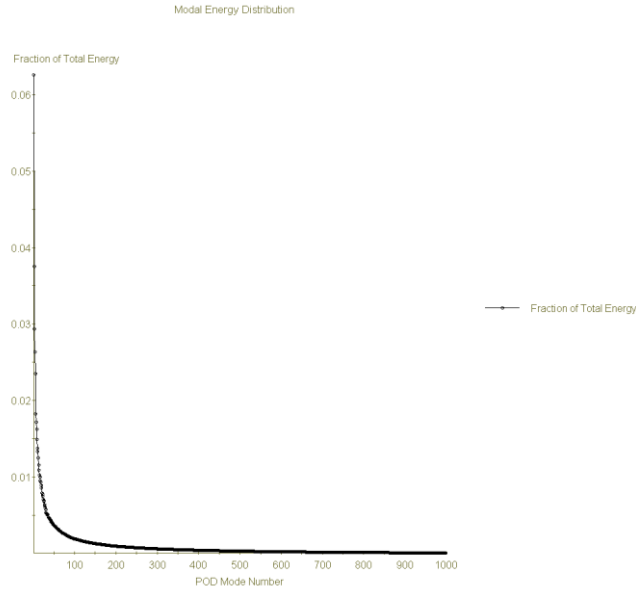


Figure 4.14: Sample POD snapshot

From Figure 4.14 it can be seen how the energy modes have been separated. The first three modes being the most influential while the rest can be considered to be noise. This snapshot is then projected onto the vector field maps to isolate the flow structures according to the chosen energy modes. Figure 4.15 presents a sample POD projection onto the vector field.

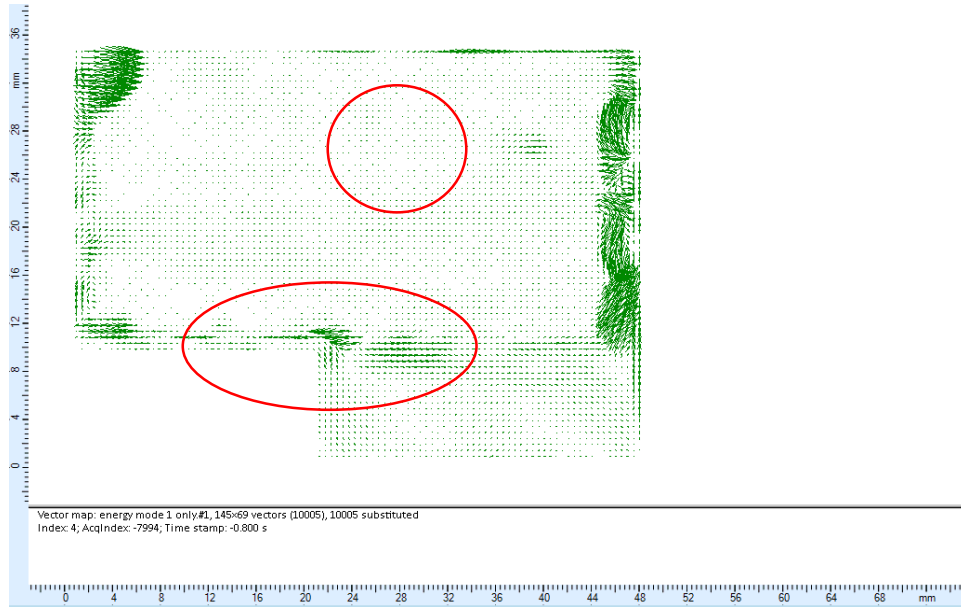


Figure 4.15: Sample POD snapshot projection

From a POD snapshot projection, it becomes possible to identify the highest energy containing flow structures. It can be seen in the image above how highest energy modes start developing about 36 mm downstream the perforated plate, and as expected a lot of high energy structures are developed in the shear layer region.

In order to better evaluate the instantaneous velocity fluctuation, or the $u(t)$ component, an extract function was used. This function in the Dynamics Studio software places a static interrogation spot that is able to acquire the instantaneous velocities that pass through it. For the present work the extract function was applied to an ensemble of 1000 velocity vector fields. A total of 5 extract points are placed along the interrogation line used to acquire the u_{RMS} and v_{RMS} out the vector statistics function. A sample plot of the extract points is presented in Figure 4.16.

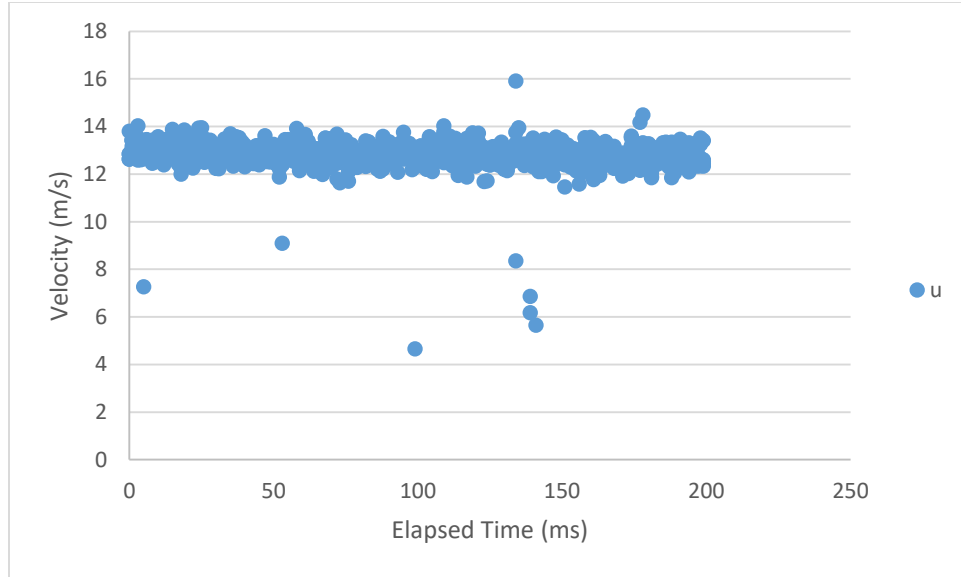


Figure 4.16: Sample instantaneous velocity measurements

As seen from Figure 4.16 the $u(t)$ is defined, from this data it can then be acquired the u_{RMS} and the v_{RMS} values needed to find the flame regime in the Borghi-Peters diagram. Figure 4.17 presents the location of the 5 different extract points utilized for this work.

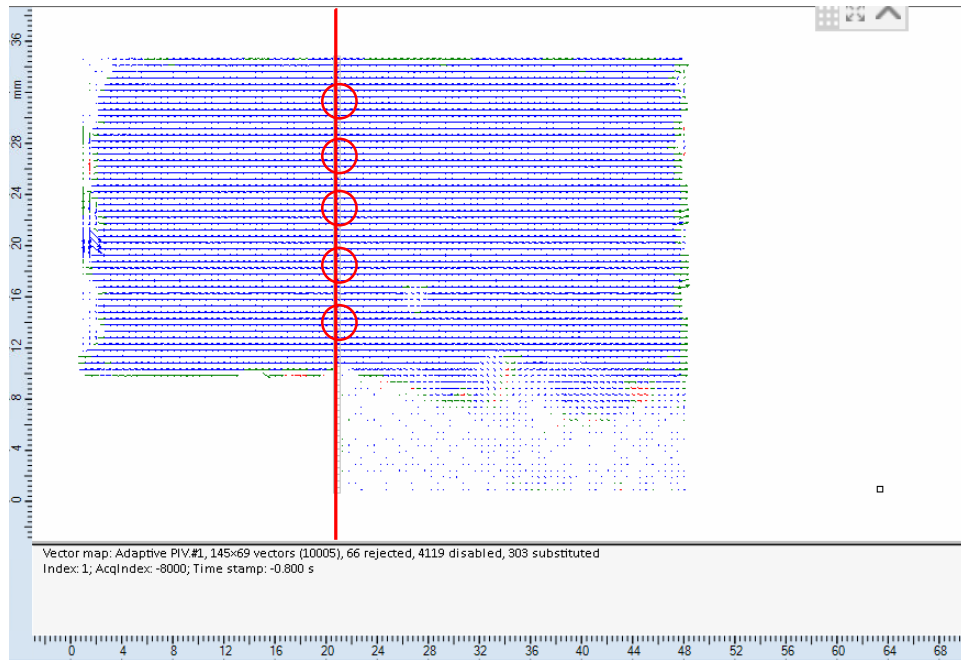


Figure 4.17: Location of the extract points

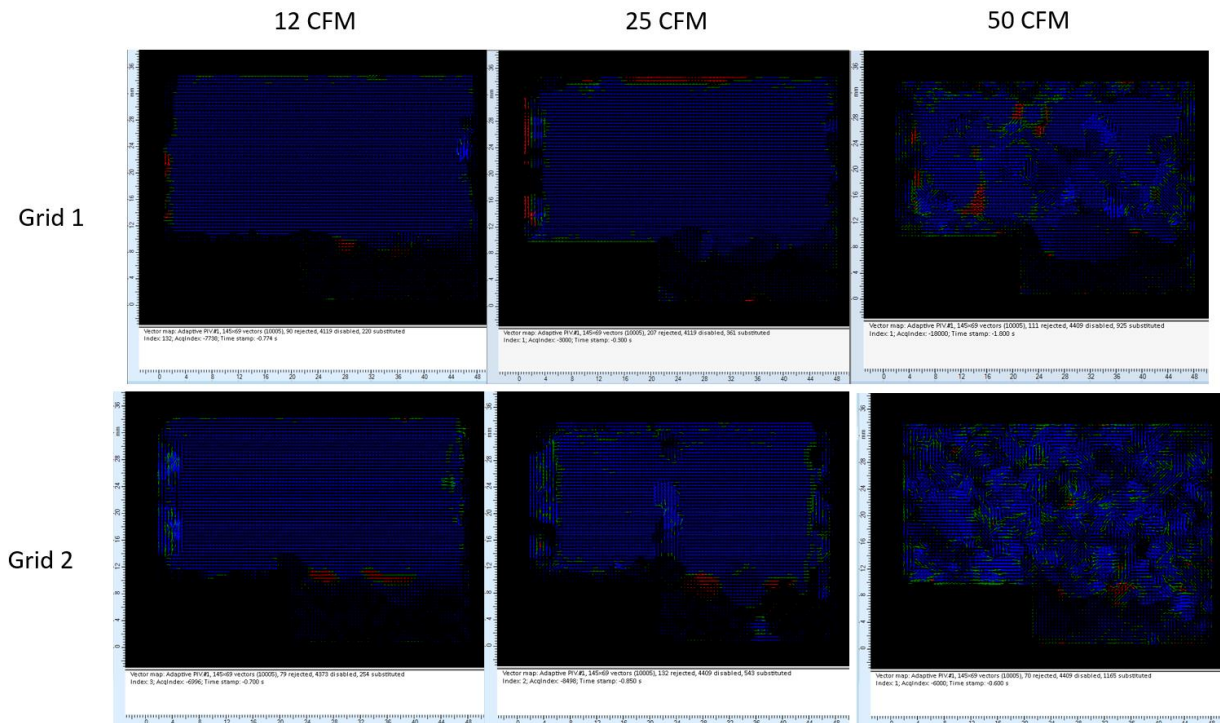
The exact location of the points can be defined thanks to the calibrated nature of the measurement. Taking the bottom of the image as 0 mm the location of the extract points are axially located at 12, 16, 21, 26, and 31 mm along the interrogation line.

The location for the interrogation line was selected based on two principles. First, the data gathered in this work will serve provide boundary conditions for computational models. It is important to interrogate the data where a boundary condition in the computational model could be easily defined. Secondly the boundary condition provided here are located at an area where the air/fuel mixture is still in its unburned conditions. These reasons provide ease of experimentation as the experiment could be carried out without having a flame present.

Chapter 5: Results and Discussion

5.1 Flow Characterization

As discussed in the methodology section, Grid 1 has a blockage ratio of 48% and holes with a 1.6 mm diameter, Grid 2 has a blockage ratio of 46% with 3 mm diameter holes, Grid 3 has a 63% blockage ratio with 1.5 mm diameter holes, and Grid 4 has a 62% blockage ratio and 3 mm diameter holes. The configurations were selected based on the largest, and smallest, machinable blockage ratios, and hole diameters. The grids were tested at 12, 25 and 50 CFM. All statistical calculations were made out of 1000 data samples. In order to be able to evaluate the PIV accuracy, fuel/air mixture velocity traveling through the setup's square channel was calculated to reach a velocity of approximately 10, 20, and 40 m/s at room temperature and atmospheric conditions before hitting the perforated plate at 12, 25, and 50 CFM respectively. Figure 5.1 presents the results acquired from the Adaptive PIV.



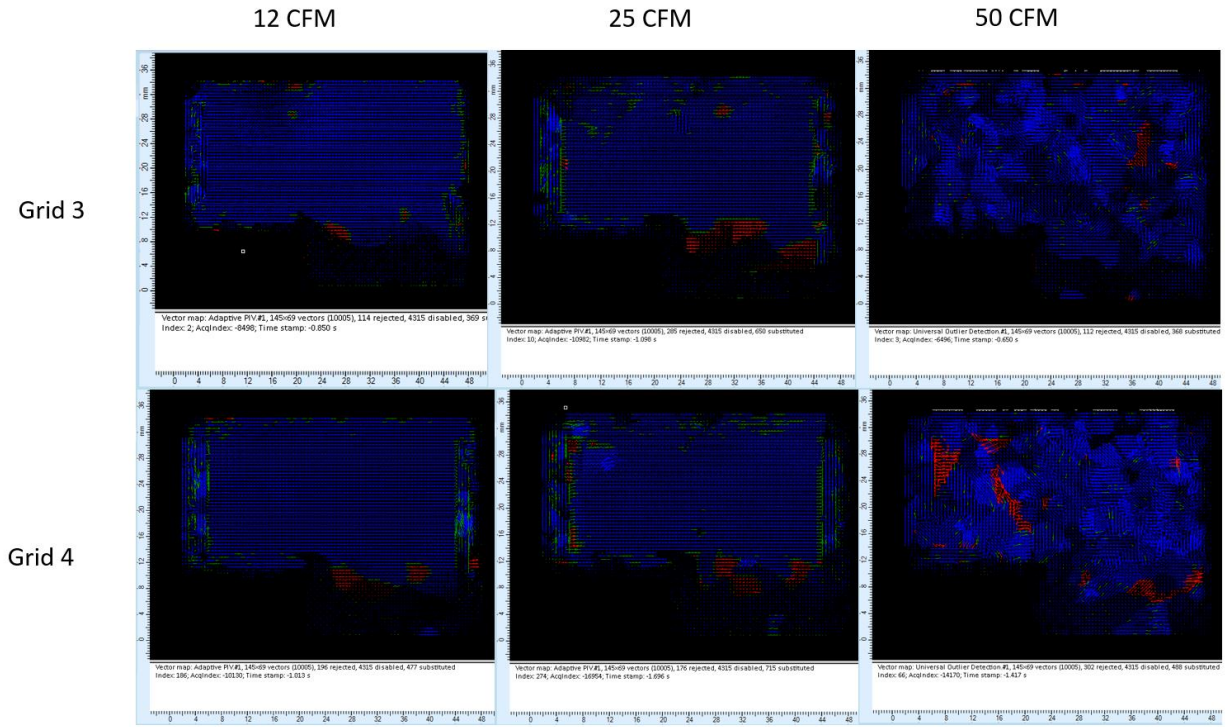


Figure 5.1: Vector map at 12, 25, and 50 CFM

Figure 5.1, presents the Adaptive PIV vector field color coded to display the accuracy of the results acquired. Blue vectors represent normal vectors, green vectors represent substituted vectors, or vectors that have been calculated using the neighboring vectors as input, and red vectors represent rejected vectors, or vectors that are generated with a low confidence level. Red vectors can occur due to low system spatial or temporal resolution, or by having the algorithm unable to track the particle. A solution to the problem, and how to manage to decrease these vectors is addressed in the conclusions chapter of this work.

Based on the color coding of the vector map it can be seen that the Adaptive PIV algorithm does a good job resolving the high velocity gradient areas present in the shear layer, as not many red vectors are present there. The parts above and below the shear layer are fully resolved for 12 and 25 CFM while at 50 CFM a larger presence of red vectors can be seen, this is due to the much higher turbulence intensity present at this condition resulting in more out-of-plane particles. The green and red vectors present on the walls are generated due to vector bias, which was mitigated as much as possible using the Adaptive PIV window function and the masking function.

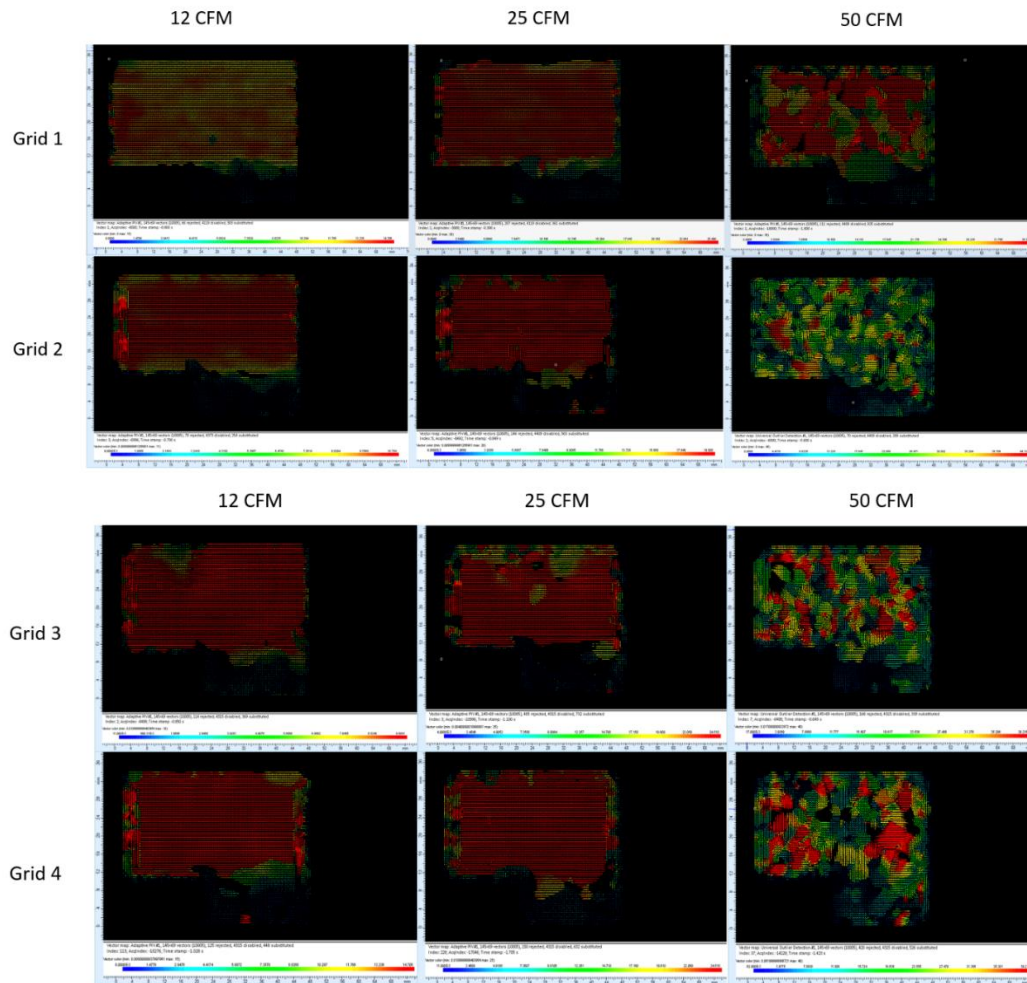


Figure 5.2: Velocity vector field map at 12, 25, and 50 CFM,

The velocity vector field has colored vectors that range from a low velocity of 0 – 1.5 m/s represented with the blue vectors to a high velocity of 13.5 - 15 m/s represented with red colored vectors at 12 CFM. The same color scheme for the other vector field maps applies with velocities from 0 – 2.5 m/s to 23 – 25 m/s at 25 CFM, and 0 – 3.5 to 31 – 35 m/s at 50 CFM. This maximum value and minimum value are based on a post-grid theoretical flow velocity calculation with a measured added acceleration. From Figure 5.2 the flow acceleration can be appreciated due to the presence of the perforated plate, yielding on average a higher velocity upon entry into the step resulting in an increase velocity depicted by a higher red vector density. The lower velocity formed in the recirculation zone of the backward facing step is also well resolved and it is noted as the anchoring point of the flame. The system's resolution is also capable of resolving some of the smaller eddies being generated on the upper part of the flow field as noted by the green-lower velocity vectors spot surrounded by the higher velocity vectors at 12 CFM, Grid 1, and at Grid 3, 25 CFM. It is interesting to note that Grid 3 at 25 CFM developed a lot of eddy formation, not present in the rest of the Grids. It can be noted the volumetric flow rate has a very noticeable effect on the increase turbulence in the flow as well. Not only can we evaluate the turbulence increase effect by the increase in flowrate, but we can also find the flame regime location based on the flow characteristics, and calculated laminar flame values. In order to accomplish this, we need to calculate the u_{RMS} and the v_{RMS} at the boundary condition locations. As previously discussed the vector statistics are usually calculated for the velocity field from a single image out of the whole ensemble, this means that the vector quantities calculated are based off an average ensemble. Figure 5.3 presents the location of the interrogation line in red and the step boundary with respect to it.

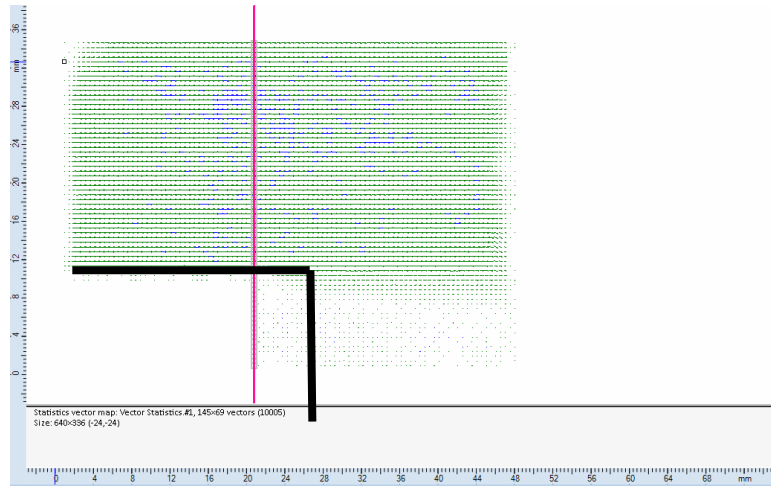


Figure 5.3: Location of the interrogation line where the vector statistics are calculated (12, 25, 50 CFM)

From Figure 5.3, the line distance starts from 0 at the bottom of the line and it ends at 37 mm at the top of the line, traversing the entire length of the interrogation region. Figure 5.4 presents the average values of the u and the v components passing through the interrogation line at different axial positions within the combustor. From Figure 5.4 we can see how the measurement starts with a velocity of 0 m/s due to the line passing through the solid part of the step, where no particles are present. At the 13 mm mark we can see a spike in velocity and how the u component is the main component throughout the velocity field. The lack of a gradual increase in the velocity gradients it is due to the wall window function used. It can also be appreciated how the flow was accelerated on average, about 5 m/s due to the presence of the perforated plate at 12 CFM, and 25 CFM. There is a lot more influence by the turbulence on the velocity acquired at the interrogation line for the 50 CFM with velocities ranging from 25 – 36 m/s when compared to the predicted value of 40 m/s. This result is expected as seen from the results on Figure 5.2.

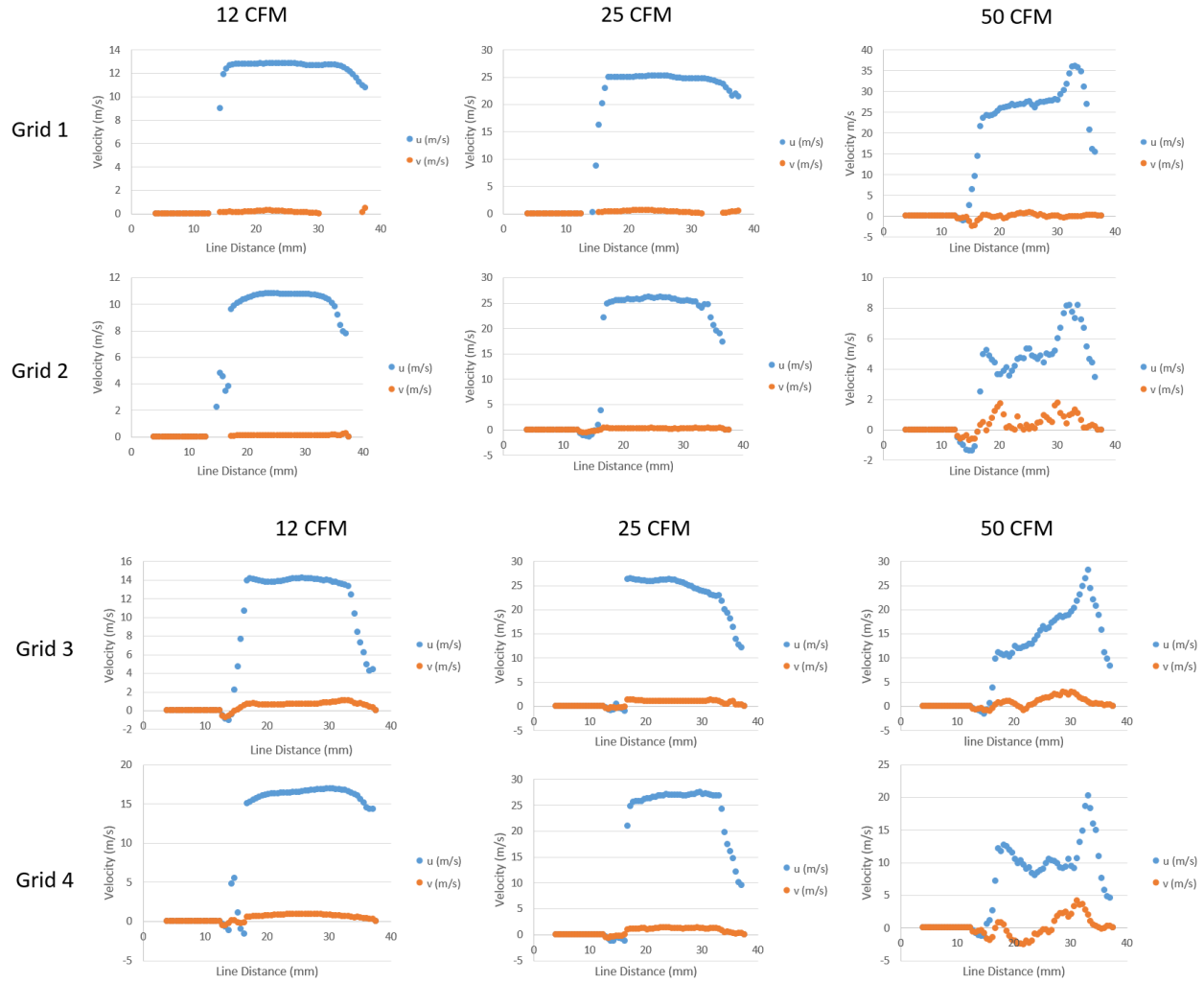


Figure 5.4: Velocity components found along the interrogation line (12, 25, 50 CFM)

As discussed throughout the literature review, a needed component to find the flame regime in the Borghi-Peters diagram is u' which is calculated as defined in equation 5.1

$$u' = \sqrt{\frac{u_{RMS}^2 + 2v_{RMS}^2}{3}} \quad (5.1)$$

Through statistical calculations the u_{RMS} and the v_{RMS} values can be acquired from the velocity vector field map, and are presented in Figure 5.5.

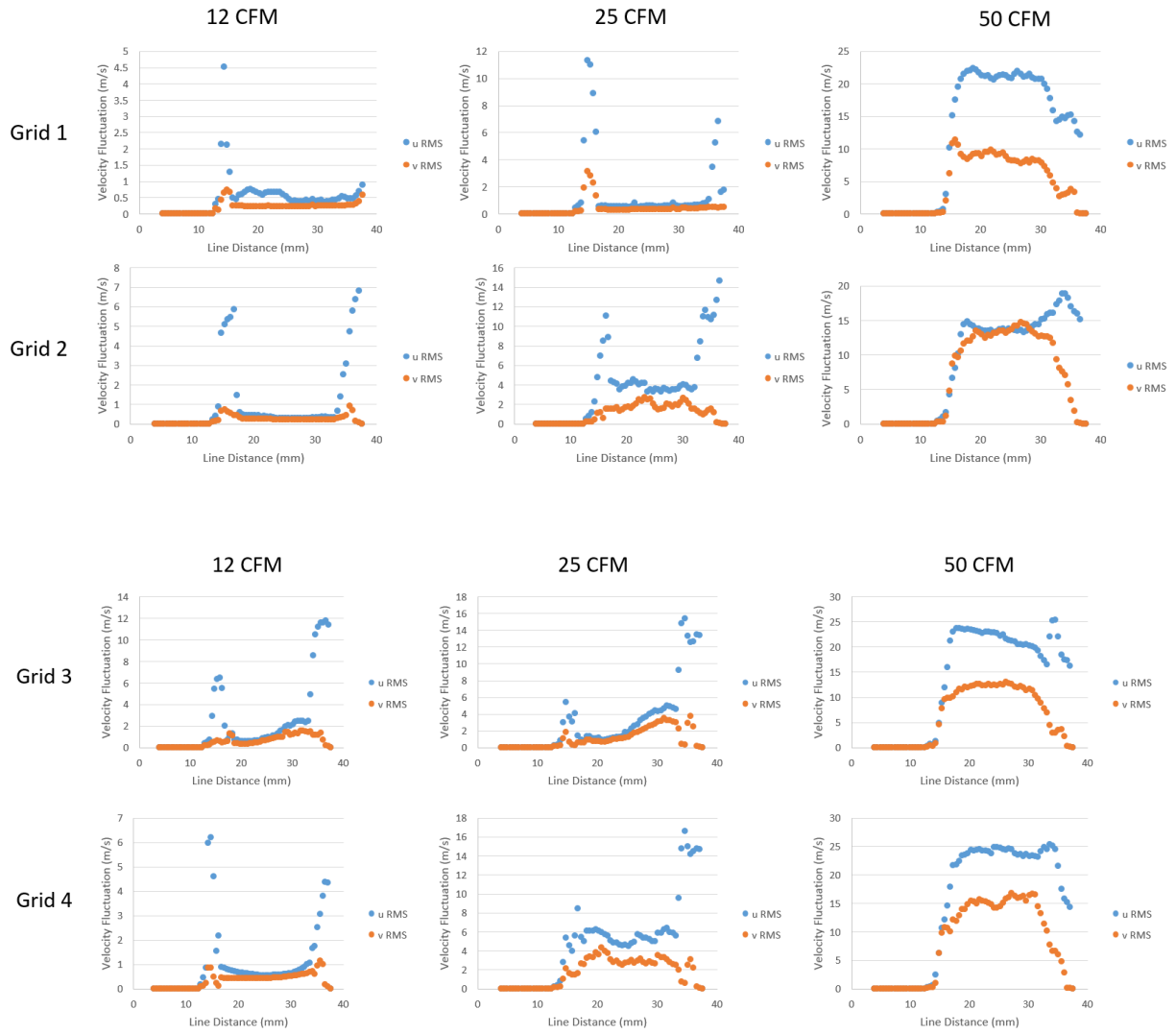


Figure 5.5: u_{RMS} and v_{RMS} components at the interrogation line location (12 CFM)

From figure 5.5 it can be seen that the velocity fluctuations at the interrogation line location appear to be relatively constant at around .5 and .25 m/s for u and v respectively at 12 CMF and 25 CFM. A large difference is noted at 50 CFM where higher turbulence levels in the flow make the v velocity component more prominent than at lower flowrates with values in the 20 and 10 m/s for the u and v components respectively. The presence of the valleys and high values present in Figure 5.5 can be further explained by utilizing a contour plot of the turbulence intensity and observing what the contour is at the interrogation line location, presented in Figure 5.6.

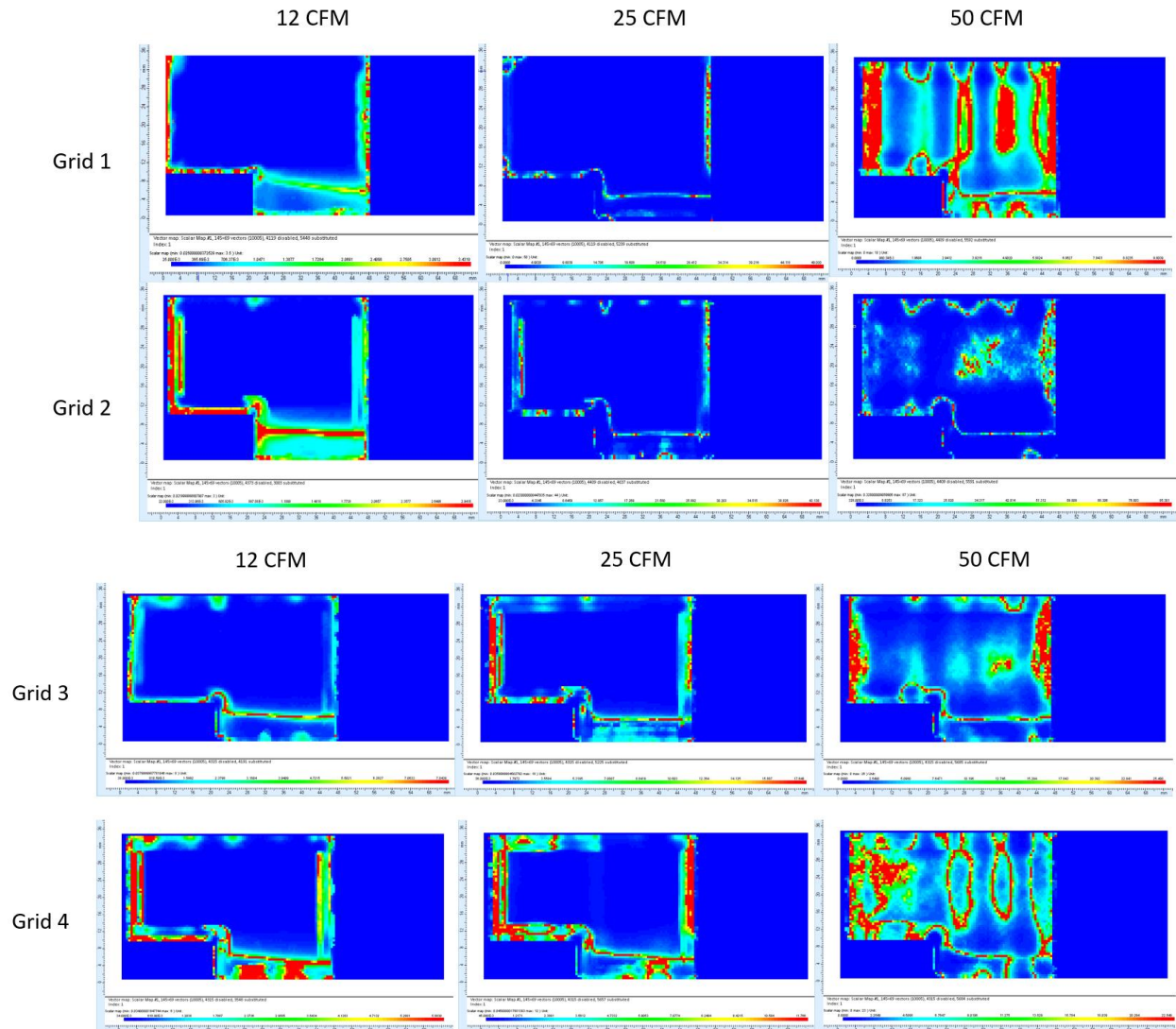


Figure 5.6: Turbulence intensity contour plot (12, 25, 50 CFM)

It can be seen from Figure 5.6 that the line, located at the edge of the step, intersects a small area where the shear layer starts developing and a flow detachment from the step's upper portion is interrogated by the line. It can also be seen how the turbulence intensity is at its highest in the recirculation area of the backward facing step combustor at 12 CFM. At 25 CFM the highest turbulence intensity is being generated at a narrower area of the shear layer and, at the recirculation zone. At 50 CFM the intense turbulent nature of the flow can be better appreciated. By comparing Grid 1 with Grid 2, and Grid 3 with Grid 4, the effect of hole diameter in the flow can be appreciated. Comparing Grid 1 with Grid 3, and Grid 2 with Grid 4, the effect of blockage ratio on the flow can be determined. It can be seen that changing the hole diameter, leads to the generation of larger turbulence intensity regions in the main cross flow area, while also generating a more turbulence intense shear layer. The flow has a similar behavior, when changing the blockage ratio. The changes are more dramatic when comparing the higher flow rate of 50 CFM condition. This is expected as Dynamic Studio calculates the turbulence intensity based off the ratio between the velocity fluctuation and the average velocity as presented in equation 5.2:

$$I = \frac{u'}{\bar{u}} \quad (5.2)$$

With a large amount of velocity fluctuations being generated by the shear layer and the recirculation eddy formed on the onset of the step, the largest turbulence intensity is expected to be located in that area, while higher flowrates, generating intense turbulence, the turbulence intensity can then be located throughout the flow. The large turbulence intensity levels present at the borders of the interrogation area are due to spurious vectors generated during the PIV vector

field processing. It is possible to look at the turbulence intensity distribution at the area right after the grid location of the 12 and 25 CFM measurements by modifying the contour image range as presented in Figure 5.7

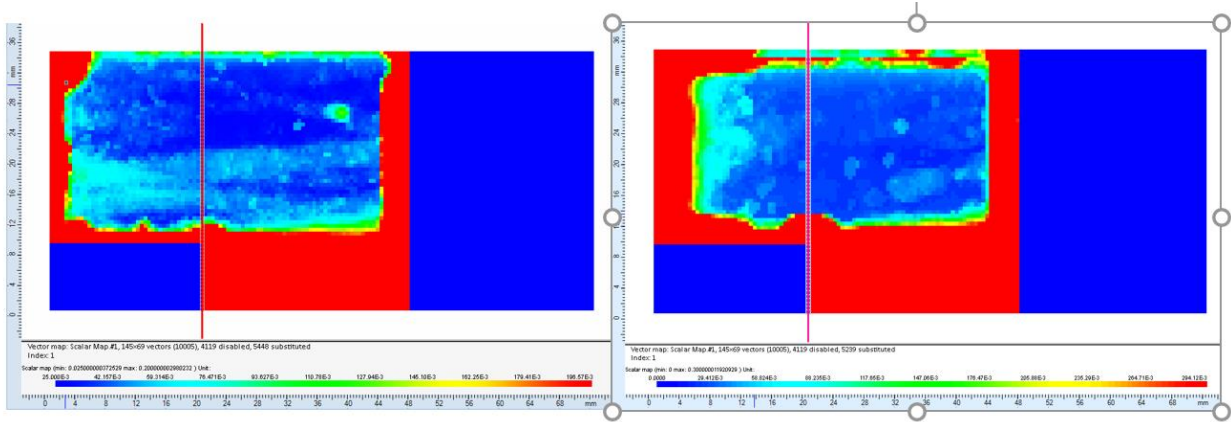


Figure 5.7: Turbulence intensity contour plot with modified scale (12, 25 CFM, Grid 1)

From Figure 5.7 it becomes easier to visualize the 15 – 20 and 20 – 25 mm mark increase in turbulence intensity at 12 CFM. These fluctuations are generated by the recirculation zone. This recirculating eddy affects only the lower part of the main cross flow, and what it is seen in Figure 5.7 is the average location of the shear layer effect on the main cross flow crossing parallel to it. At 25 CFM we can see how the effect seen at 12 CFM is reduced due to the higher momentum carried by the cross flow resulting on high shear energy highly concentrated at the shear layer.

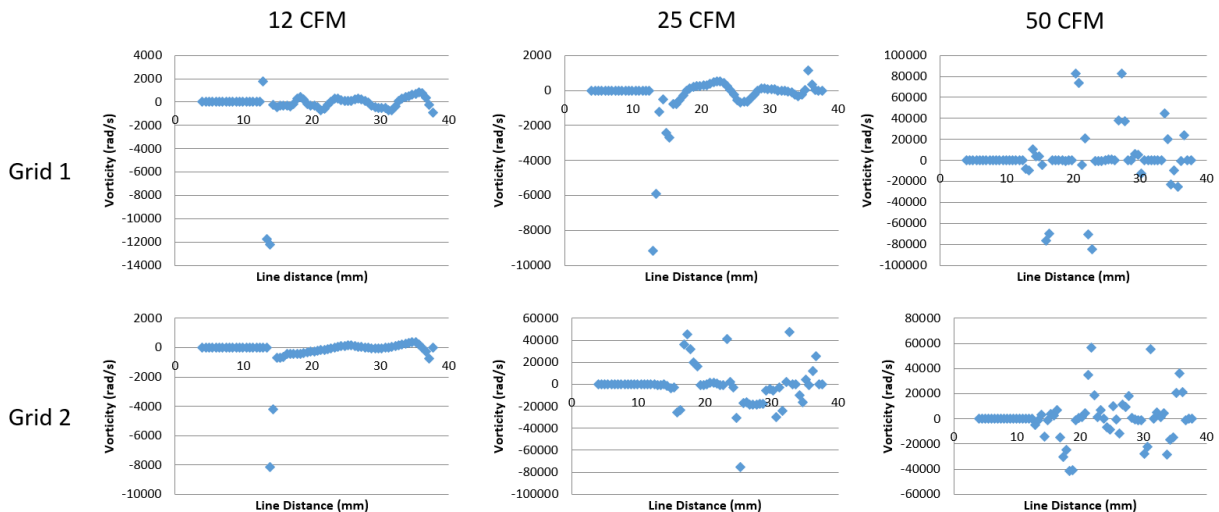
Thanks to the ability of the PIV measurement to resolve not only the velocity, but the direction of the flow at discrete locations, it is possible to conduct scalar derivative calculations. For a fluid flow, the tendency of the fluid flow to spin can be defined as vorticity. In the Dynamic Studio software, the vorticity of the velocity vector field ensemble is calculated by equation 5.3

$$\bar{\omega} = \text{rot}(\bar{U}) = \text{curl}(\bar{U}) = \nabla \times \bar{U} = \left(\frac{\partial W}{\partial y} - \frac{\partial V}{\partial z} \right) \bar{i} + \left(\frac{\partial U}{\partial z} - \frac{\partial W}{\partial x} \right) \bar{j} + \left(\frac{\partial V}{\partial x} - \frac{\partial U}{\partial y} \right) \bar{k} \quad (5.3)$$

Where each term describes the rotation around the x, y, and z axis. For a 2D fluid flow it is reduced to the rotation along the z-axis only as presented in equation 5.4

$$\omega_z = \frac{\partial V}{\partial x} - \frac{\partial U}{\partial y} \quad (5.4)$$

In order to project what the vorticity limits would be according to the values imposed by the interrogation line, simulating the boundary condition inlet, we sample the vorticity values crossing the interrogation line using a line plot function. Figure 5.8 presents the vorticity found across the interrogation line. From Figure 5.8, the maximum and minimum values passing the interrogation line can be found. A contour plot can now be defined with the maxima and minima



present at the interrogation line for the different flow conditions. Figure 5.9 presents the contour plot adjusted for the vorticity maximum and minimum levels found.

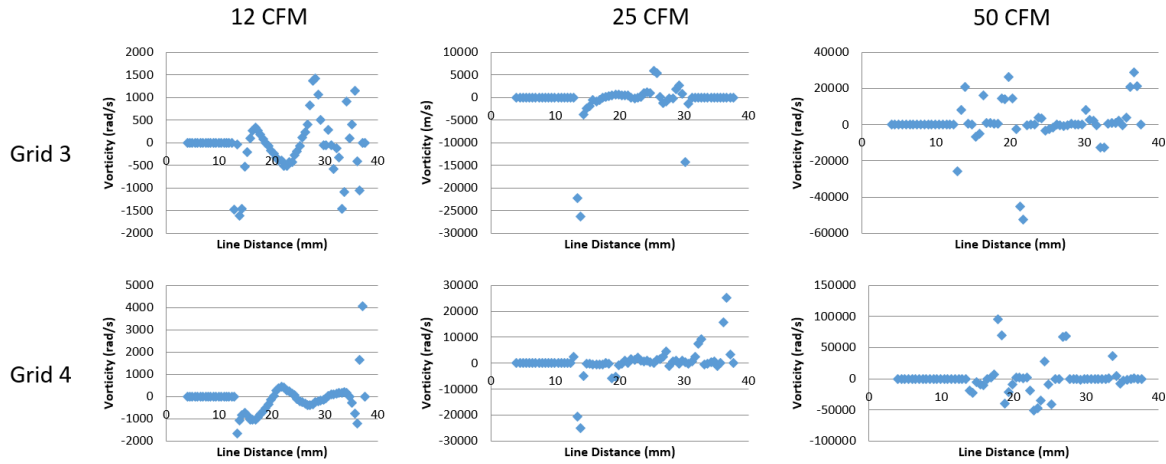


Figure 5.8: Vorticity levels found on the interrogation line at the different flow conditions

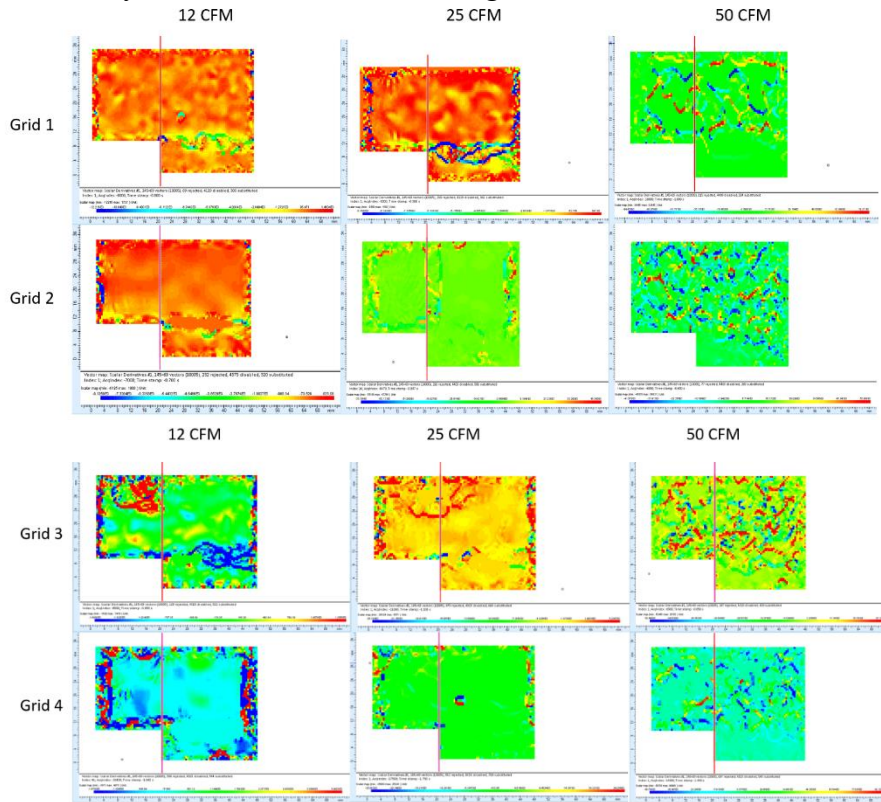


Figure 5.9: Vorticity contour plot and location of interrogation line (12, 25, 50 CFM)

Similar to the turbulence intensity case, we can see that at the 11-12 mm mark for the 12 and 25 CFM conditions there is a big effect felt due to flow detachment on the onset of the step. It can also be seen that the velocity vector field map is capable of resolving vortex pairs presented by the red/blue pairs formed at 12 CFM, as well as the high level of vorticity being generated at the shear layer. We can see the effect of vorticity change dramatically at 50 CFM as the highest vorticity levels are concentrated on the edges of the vortex pairs and are not as spread out, making them appear as lines instead of spots. While the hole diameter has an effect on the vorticity levels of the flow, the blockage ratio has an even higher influence on the vorticity levels in the flow, evident by the vorticity levels present in the contour plot. This tool becomes important at the eddies generated can be tracked down to the location of the flame front. The edges of the interrogation area appear to have a lot of activity due to the presence of spurious vectors generating the vorticity seen along the edges of the 12 and 25 CFM pictures, this was mitigated using the outlier edge detection algorithm along with the wall windowing addition in the adaptive PIV post processing.

As discussed previously, POD is a powerful tool utilized to decompose the flow and identify the flow structures with the highest energy content. Figure 5.10, presents the POD snapshot of the flow at 12 CFM, Grid 1 condition. The plot decomposes the flow into energy modes and ranks them by energy level. In order to find the highest energy containing flow structures in the PIV measurements, these POD snapshots are projected onto the vector field, as presented in Figure 5.11.

Modal Energy Distribution

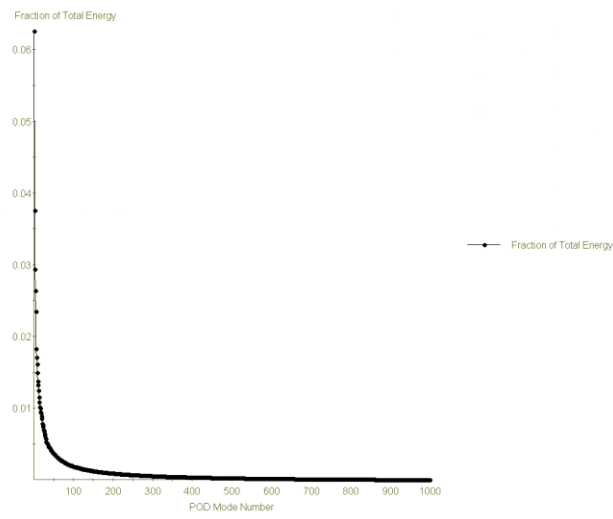
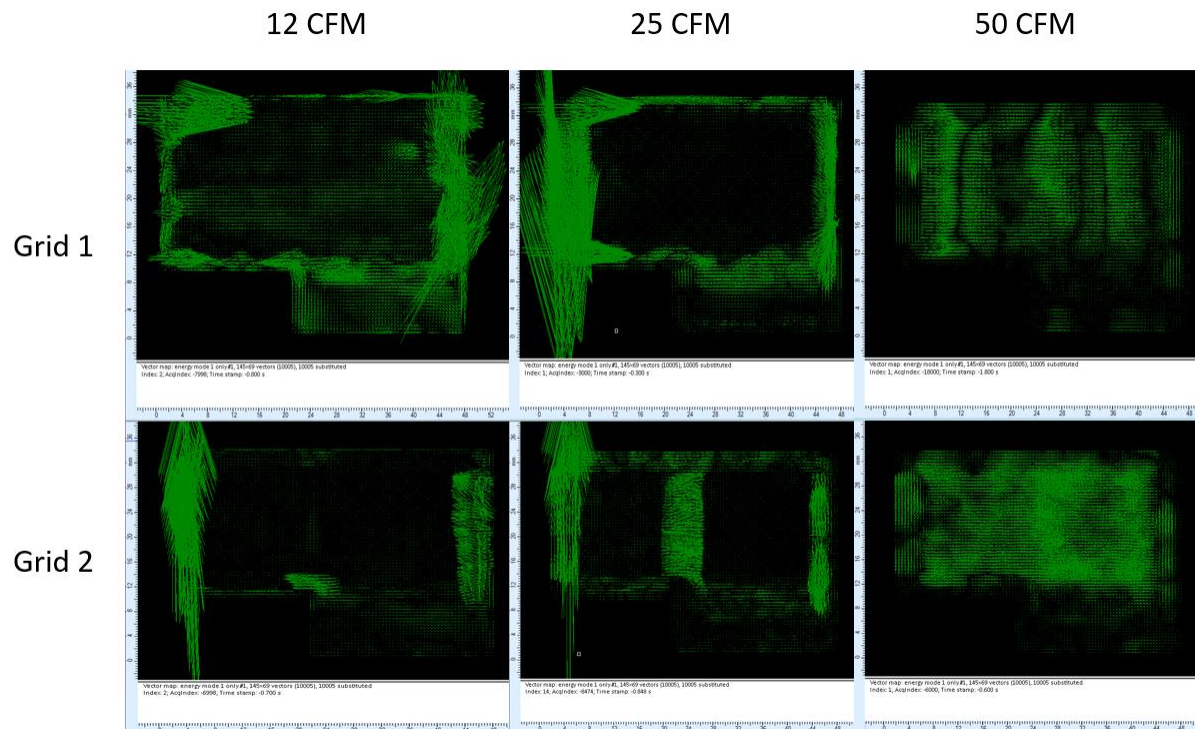


Figure 5.10: POD projection to velocity vector field (12 CFM)



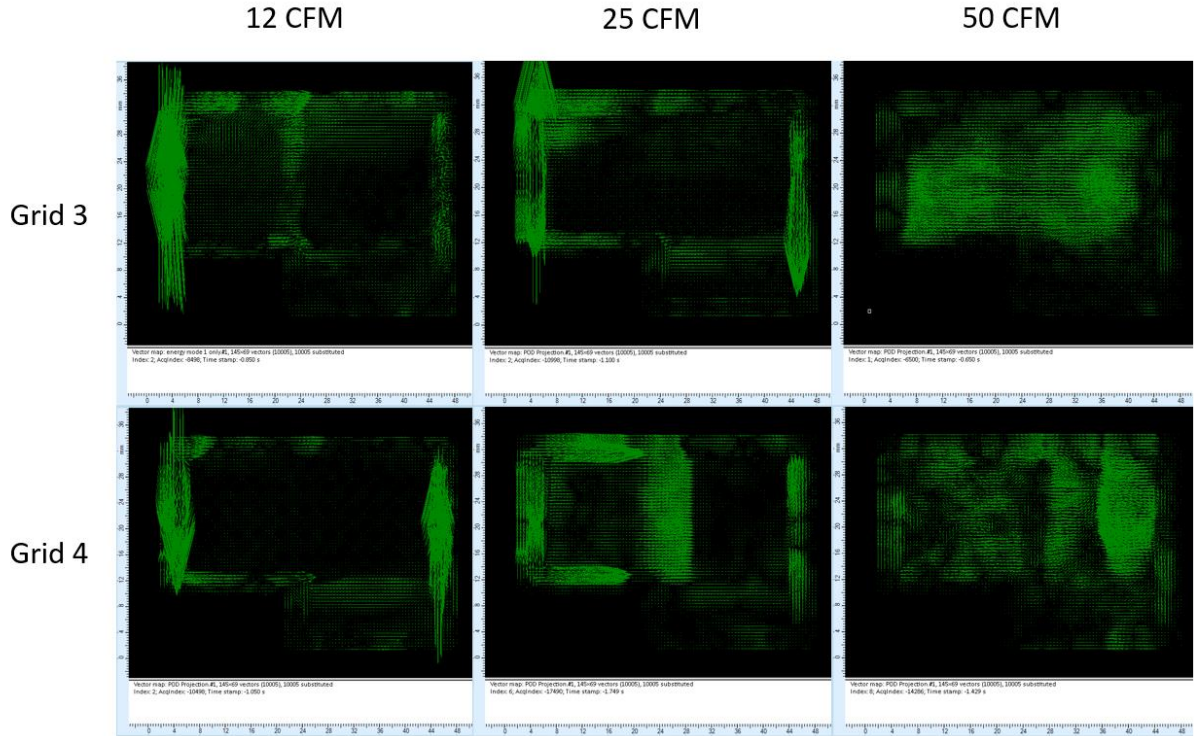


Figure 5.11: POD projection to velocity vector field at the different flow conditions

The highest energy mode used to generate Figures 5.11 reveals the highest energy mode structures in the flow, including a lot of activity on the step edge, also picked up by high turbulence intensity levels, and the high-energy-containing structures generate by the shear of the high and low velocity flow regions. Figure 5.11 shows a considerable amount of noise at the edge of the interrogation area but it does not affect the appearance of the large eddy structures being formed at the shear layer. The figure also shows the location of the highest energy containing structures along the main cross flow, which can be further corroborated using the vorticity map to denote the location of the eddies formed in the flow.

In order to acquire a more representative result of the u_{RMS} and the v_{RMS} components, the presented work here proposes the use of the extract method along the same interrogation line used to generate the results presented in Figure 5.4. Figure 5.12, 13, 14 presents the $u(t)$ and the $v(t)$ extracted from one of the velocity vector field maps ensemble, which can later be further post processed to acquire the u_{RMS} and the v_{RMS} components from the instantaneous velocity, instead of the average velocity. This provides better accuracy of the velocity u_{RMS} and the v_{RMS} values.

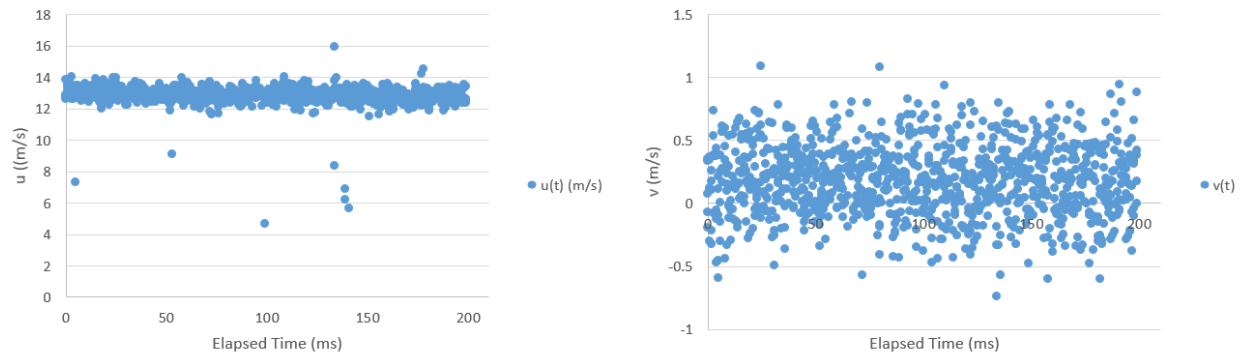


Figure 5.12: $u(t)$ and $v(t)$ at an interrogation point at 12 CFM

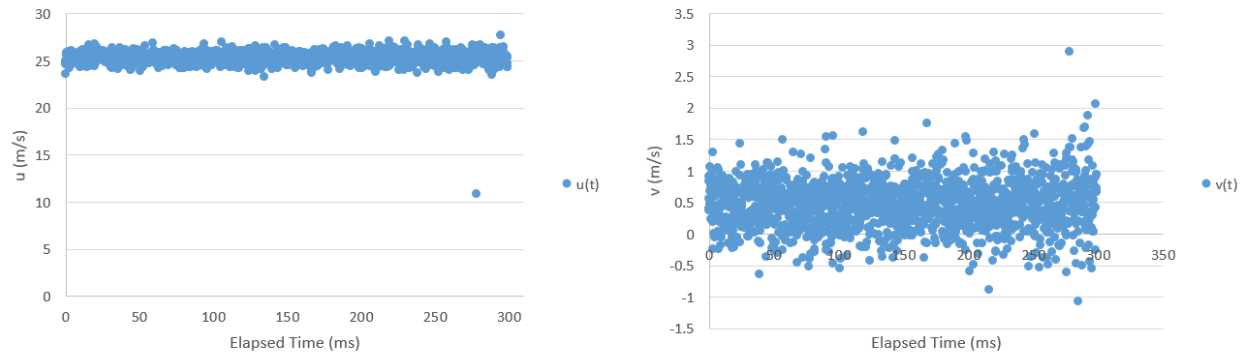


Figure 5.13: $u(t)$ and $v(t)$ at an interrogation point at 25 CFM

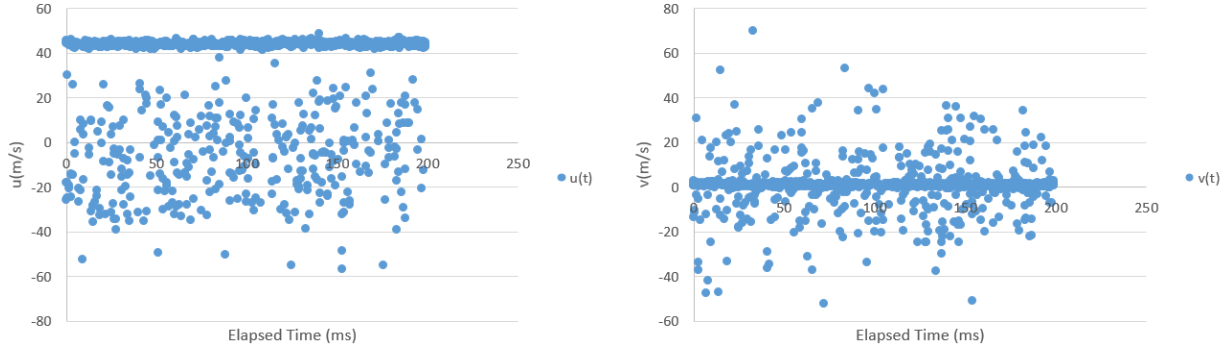


Figure 5.14: $u(t)$ and $v(t)$ at an interrogation point at 50 CFM

The extracted instantaneous velocity values are used to calculate the RMS velocity components as discussed in the methodology section. Because of the nature of the PIV measurement, velocity estimates are made as a spatial average over the interrogation area. Keeping this in mind it can be said that the turbulent kinetic energy, mathematically, is proportional to the sum of the variances of the velocity components. In this case of the u and v components [74]. Figure 5.15 presents the turbulent kinetic energy profile plot at the different flow conditions, and demonstrates how the POD is able to resolve for the most energetic structures based off the TKE energy level.

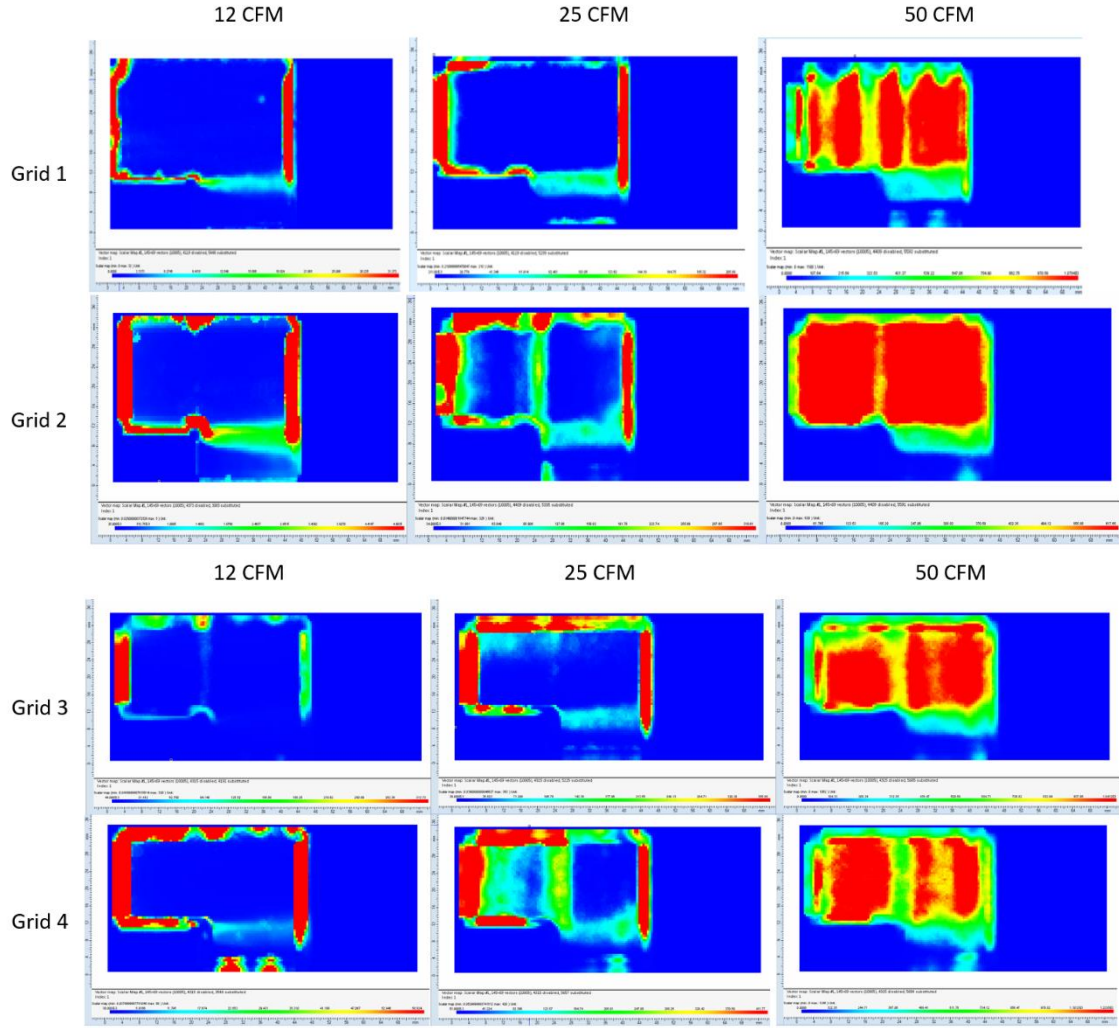


Figure 5.15: TKE contour plots at the different flow conditions

From the TKE profile plots, it can be seen how the larger hole diameter grids generate larger flow structure, which can be corroborated through the POD projections. On the other hand, the stronger influence by the blockage ratio is evident when looking at the TKE contour plots along with the POD projection as a larger blockage ratio generates separated flow structures, while a smaller blockage ratio generates a continuous energetic flow.

Now that the flow has been fully characterized, the location on the Borghi-Peters diagram can be found. Utilizing the laminar flame thickness found in literature from the literature review section along with the laminar flame speed of an atmospheric methane/air flame at room temperature, and equivalence ratio of 1 finish the variables needed to populate the results presented in Table 5.1. This table summarizes the post processed data acquired from the PIV measurements using the different perforated plates, and Table 5.2 presents the location of each Grid and flow condition.

Table 5.1: Summarized flow data. Grid 1 through 4 from top to bottom.

Grid	Re_H	Φ	U_{Bulk} (m/s)	U PIV (m/s)	u' (m/s)	Da	Ka	Re_T	u'/S_L	L_T	L_T/δ_L
48% BR - 1.5 mm dia	15,400	1.0	10	13	1.1	21.3	0.8	147.5	3.0	0.0173	49.4
	32,100	1.0	20	25	3.5	18.8	7.0	458.4	9.3	0.0173	49.4
	64,200	1.0	40	27	23.4	0.9	70.3	3034.6	61.5	0.0173	49.4
46% BR - 3 mm dia	15,400	1.0	10	11	1.7	34.2	1.7	234.2	4.4	0.0186	33.2
	32,100	1.0	20	26	9.8	2.2	18.2	1364.7	25.7	0.0186	33.2
	64,200	1.0	40	8	18.9	1.3	50.2	2647.4	49.8	0.0186	33.2
63% BR - 1.5 mm dia	15400	1.0	10	14	5.5	5.1	10.3	604.5	14.5	0.0146	41.8
	32100	1.0	20	26	7.5	4.3	16.8	824.0	19.7	0.0146	41.8
	64200	1.0	40	28	25.6	0.9	90.2	2814.1	67.4	0.0146	41.8
62% BR - 3mm dia	15400	1.0	10	17	2.5	13.9	3.4	300.5	6.6	0.0160	45.6
	32100	1.0	20	27	11.0	1.8	24.6	1315.9	28.9	0.0160	45.6
	64200	1.0	40	33	27.7	0.8	95.9	3316.9	72.8	0.0160	45.6

Table 5.2: Grid parameters on the Borghi-Peters diagram

	Grid 1		Grid 3	
	L_T/δ_L	u'/S_L	L_T/δ_L	u'/S_L
12 CFM	49.371	2.987	41.77	14.471
25 CFM	49.371	9.285	41.77	19.727
50 CFM	49.371	61.465	41.77	67.37
	Grid 2		Grid 4	
	L_T/δ_L	u'/S_L	L_T/δ_L	u'/S_L
12 CFM	33.171	4.405	45.57	6.594
25 CFM	33.171	25.665	45.57	28.875
50 CFM	33.171	49.97	45.57	72.785

The location on the Borghi-Peters diagram can be found, as presented in Figure 5.16.

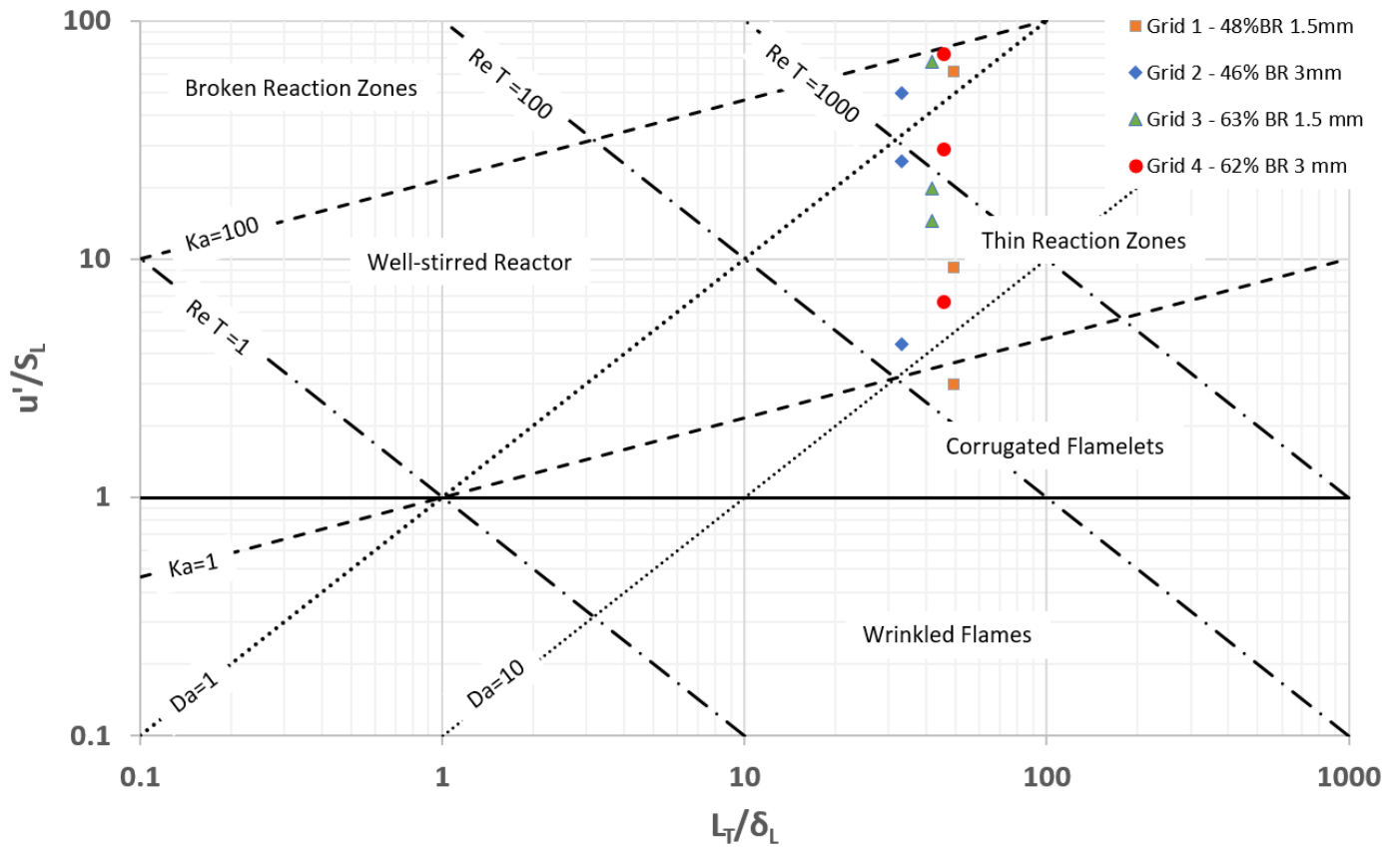


Figure 5.16: Location of the different grids on the Borghi-Peters diagram.

From Figure 5.16 it can be seen that the presented work lands in the desired Thin Reaction Zones, at times crossing to the Corrugated Flamelets Regime, and the Well-stirred Reaction zone. Based on this chart, it can be concluded that in order to land on the desired zone Grid 1 can be used as long as the flowrate is set at 25 CFM. Grid 2, 3, and 4 can be used for 12 and 25 CFM to land in the Thin Reaction Zone. All the grids land in the Well-stirred Reactor zone at the 50 CFM flow rate. In order to bring the measurements down, heated reactants can be used to increase the flame speed generated, bringing down the points to the desired zone.

Chapter 6: Conclusions and Future Investigation

6.1 Concluding Remarks

The presented work has studied the global characteristics of a backward facing step high intensity turbulent flows using Time Resolved Particle Image Velocimetry (TR-PIV), and successfully presented the flame regime zone the experimental setup is capable of reaching when using the presented configuration. The components of turbulence intensity and kinetic energy have been resolved through statistical analysis and the data has been summarized in the form of contour plots at different flow conditions. The effect of bulk velocity parameters, turbulence parameters, and recirculation zone characteristics have been presented. The presented PIV setup and analysis techniques have proven to be able to resolve the high velocity gradients present in the shear layer of the combustor. The PIV results were later post process to find velocity ranges from 0 – 15 m/s, 0 – 25 m/s, and 0 – 35 m/s for the 12, 25, and 50 CFM conditions respectively. The components of turbulence intensity, and kinetic energy have been resolved and presented in the form of contour plots. Utilizing a POD analysis, the highest-energy-containing structures have been identified. The vorticity levels generated by the different perforated plates has also been resolved and presented in the form of contour plots. The bulk flow rate effect was seen to provide a flow acceleration of 5 m/s on average when compared to the calculated values. With the interrogation line flow velocity analysis, it can be seen that a fully developed turbulent flow enters the combustor area when conducting experiments at a Reynolds number of 15,000 and 32,000, while at a Reynolds number of 64,000 the highest turbulence intensity is reached making the v component take a major role, decreasing the u components magnitude by up to 10 m/s on average. It is believed that this can be explained by the grid position with respect to the I.A. location, where at this point, are looking at

the transition region of the turbulent flow. This could be alleviated by moving the grid further upstream on the combustor fuel inlet. The bulk flow has the greatest impact on the u' value.

It was found that altering the characteristic length properties of the combustor has the greatest effect on the u' values, increasing the measured u' values up to 80% on average. It was also found that the system possessed enough resolution to generate reliable vorticity contour plots, when compared to previous studies [75] for the 15,000 to 32,000 Reynolds number conditions. At the 64,000 Reynolds number condition it was found that the PIV system was found to be reaching the upper bounds of its measurement capabilities.

Future work could include the investigation of the z-component on the experimental setup and determine the wall effects on the measurements to compliment the results presented in this work. With the help of a high speed PLIF measurement ran simultaneously, the analysis of what the influence the different grids have on the flame front can also be investigated. Turbulence flame speed studies could be conducted on the backward facing step flame in order to investigate the influence the flame corrugation caused by the different grid configurations. The machinability aspect of the presented blockage ratios could be surpassed by investigating with additive manufactured grids to achieve higher, or lower blockage ratios. The inlet manifold of the combustor can be modified to fit the grids further upstream from the fuel injection point to reduce the presence of the identified large structures in the field where the flame is present.

While the presented experimental setup has successfully resolved the flow, it was noted that the system's resolution was not enough to resolve the higher flow rates than 50 CFM, as more

invalid vectors were present in the PIV vector field maps. In order to mitigate the appearance of these vectors, it is recommended to acquire a high speed camera with higher resolution a 10kHz. This will help the measurement by being able to capture more particles within the interrogation area, increasing resolution. The higher resolution will also allow for a larger scale factor to increase the spatial resolution of the PIV measurements. In order to further provide system flexibility to achieve the desired flame regimes, an air heater could be incorporated to provide a variable flame speed to place the measurements in the desired flame regime region.

References

- [1] Durst, F., and Pereira, J. C. F., 1988, "Time-dependent laminar backward facing step flow in a two-dimensional duct", ASME J. Fluids Eng., 110, pp. 289–296.
- [2] Biswas G., Breuer M., Durst F. "Backward-Facing Step Flows for Various Expansion Ratios at Low and Moderate Reynolds Numbers". Journal of Fluids Engineering MAY 2004, Vol. 126.
- [3] Armaly B.F., Durst F., Pereira JCF, Schönung B. "Experimental and theoretical investigation of backward-facing step flow". J. Fluid Mech. (1983), vol. 127, p p. 473496.
- [4] So R.M.C., Yuan S.P. "Near-wall Two-equation and Reynolds-stress Modeling of Backstep Flow". Int. J. Engng Sci. Vol. 36, No. 3, pp. 283-298, 1998.
- [5] Acosta-Zamora A., Choudhuri A., Hossain M. A., Quiroz M. (2014). "Design of a High Turbulence Intensity Combustion System". Paper presented at the 50th AIAA/ASME/SAE/ASEE Joint Propulsion Conference, Cleveland, Ohio. July 28 – 30.
- [6] Reynolds, O. " An experimental investigation of the circumstances which determine whether the motion of water shell be direct or sinuous, and the law of resistance in parallel channels." Philos. R. Soc. London Ser. A 186, 935-982 .
- [7] Reynolds, O. " On the dynamical theory of incompressible viscous flow and the determination of the criterion." Philos. R. Soc. London Ser. A 123-161
- [8] Pope S.B. " Turbulent Flow ", Cambridge university press, 2000.
- [9] "Basics of turbulent flow", www.mit.edu, accessed 2015
- [10] Kolmogorove, A.N. (1941a), 'Dissipation of energy in locally isotropic turbulence.' Dokl. Akad. Nauk SSSR 32, 19-21

- [11] Comte-Bellot, G. and Corrsin S. (1966), The use of a contraction to improve the isotropy of grid-generated turbulence. *Journal of Fluid Mechanics*, 25, 657-682
- [12] Davidson P. A., 'Turbulence, An Introduction for scientists and engineers' Oxford University Press 2004
- [13] Hoinghaus K.K., Jeffries J.B.. "Applied Combustion Diagnostics", Taylor and Francis, 2002
- [14] Lourenco, L., Krothapalli A., et al. (1989) Particle Image Velocimetry. *Advances in Fluid Mechanics Measurement*. M. Gad-el-Hak, Springer-Verlag: 128-135
- [15] Adrian, R.J. (1991). Particle-Imaging Techniques for Experimental Fluid Mechanics. *Annual Review of Fluid Mechanics* 23: 261-304
- [16] Grant, I. (1997). Particle image velocimetry: a review. *Proc. Instn, Mech Engrs*. 211(C): 55-76
- [17] Crowe, C.T., Sommerfeld, M., and Tsuji, Y. (1998) *Multiphase flows with droplets and particle*, CRC Press, Boca Raton, Fla
- [18] Merzkrich, W. (1987) *Flow visualization*, Academic Press, Orlando
- [19] Raffel, M., Willert, C.E., and Kompenhans, J. (1998) *Particle image velocimetry: a practical guide*, Springer, Berlin; New york
- [20] Santiago, J.G., Wereley, S.T., Meinhart, C.D., Beebe, D.J., and Adrian, R.J (1998) 'Particle Image velocimetry system for microfluidics'. *Experimental in Fluids*. 25(4),316-319
- [21] Epstein A.H. - Quantitative density visualization in a transonic compressor rotor. *J. Energ. Power* 99 (1977) 460-475

- [22] Kychakoff G., Howe R. D., Hanson R. K.- Quantitative flow visualization technique for measurements in combustion gases. *Appl. Opt.* 23 (1982) 704-712.
- [23] Miles R.- Flow-field Diagnostics, *Applied Combustion Diagnostics*. Edited by Katharina Kohse-Höinghaus & Jay Jeffries, Taylor and Francis Publishers (2002).
- [24] Turns S. R., ' An Introduction to Combustion, concept and application ', McGraw Hill, 3rd ed.
- [25] Dixon-Lewis G., Goldsworthy F.A., Greenberg J.B., *Proc. R. Soc. London Ser. A* 346 (1976) 261.
- [26] Gardner Jr. W.C. (Ed.), *Combustion Chemistry*, Springer-Verlag, New York, 1984.
- [27] Frenklach M., Wang H., Rabinowitz J., *Prog. Energy Combust. Sci.* 18 (1992) 47.
- [28] Dagaut P., Reuillon M., Boetner J.C., Cathonnet M., *Proc. Combust. Inst.* 25 (1994) 919.
- [29] Marinov N.M., Pitz W.J., Westbrook C.K., Castaldi M.J., Senkan S.M., *Combust. Sci. Technol.* 116– 117 (1996) 211.
- [30] Curran H.R., Gaffuri P., Pitz W.J., Westbrook C.K., *Combust. Flame* 114 (1998) 149.
- [31] Ranzi E., Dente M., Goldaniga A., Bozzano G., Faravelli T. *Prog. Energy Combust. Sci.* 27 (2001) 99.
- [32] Simmie J.M., *Prog. Energy Combust. Sci.* 29 (2003) 599.
- [33] Petrova M.V., Williams F.A., ' A small detailed chemical-kinetic mechanism for hydrocarbon combustion ', *combustion and flame* 144 (2006) 526- 544
- [34] Friedman, R., and Burke, E., 'Measurement of Temperature Distribution in a Low-Pressure Flat Flame,' *Journal of Chemical Physics*, 22: 824-830 (1954)
- [35] Fristorm, R. M., *Flame structure and Process*, Oxford University Press, New York, 1995

- [36] Vagelopoulos, C.N. and Egolfopoulos, F.N., Twenty-seventh Symposium (International) on Combustion, p.513, 1998.
- [37] Vagelopoulos, C.M., Egolfopoulos, F.N., and Law, C.K., *25th Symp. (Int'l.) on Combust.* p. 1341 (1994);
- [38] Van Maaren, A., Thung, D.S. and de Goey, L.P.H. (1994) Measurement of flame temperature and adiabatic burning velocity of methane/air mixtures. *Combust. Sci. Technol.*, 96, 327.
- [39] Smith G.P., Golden D.M., Frenklach M., Moriarty N.G., Eiteneer B., Goldenberg, M.C., Bowman C., Hanson R.K., Song S., Gardiner W.C., Lissianski V., and Qin Z. http://www.me.berkeley.edu/gri_mech/
- [40] Egolfopoulos F.N., Cho, P. and Law, C.K., " Laminar flame speeds of methane-air mixtures under reduced and elevated pressures *Combust. Flame* 76, 375 (1989)
- [41] Garforth, A.M. and Rallis, C.J., " Laminar burning velocity of stoichiometric methane-air: pressure and temperature dependence *Combust. Flame* 31, 53 (1978).
- [42] Babkin, V.S., Kozachenko, L.S., and Kuznetsov, I.L., *Zh. Prikl. Mekhan. Tekn. Fiz.* 145 (1964);
- [43] Babkin, V.S. and Kozachenko, L.S., *Combust. Explosion and Shock Waves* 2(3), 46 (1966);
- [44] Babkin, V.S., V'yun, A.V. and Kozachenko, L.S., *Combust. Explosion and Shock Waves* 2(2), 32 (1966).
- [45] Andrews G.E. and Bradley D., *Combust. Flame* 19, 275 (1972). Lijima, T. and Takeno, T., *Combust. Flame* 65, 35 (1986).
- [46] Lijima, T. and Takeno, T., *Combustion and Flame* 65, 35(1986)

- [47] Gottgens, J., et al. "ANALYTIC APPROXIMATIONS OF BURNING VELOCITIES AND FLAME THICKNESSES OF LEAN HYDROGEN, METHANE, ETHYLENE, ETHANE, ACETYLENE, AND PROPANE FLAMES." *Twenty-Forth Symposium (International) on Combustion*, pp. 129-35.
- [48] Borghi, R., "On the structure and Morphology of Turbulent Premixed Flames". Recent Advances in Aeronautical Science. Plenum Press, New York. 1985
- [49] Peters, N., "The turbulent burning velocity for small-scale and large-scale turbulence". J. Fluid Mech., 1999. 384: p. 107-132.
- [50] Zimont, V., Theory of turbulent combustion of homogenous fuel mixture at high Reynolds numbers. Fizika Goreniya i Vzryva, 1979. 15: p. 23-32.
- [51] Siewert, P. *Flame front characteristics of turbulent lean premixed methane / air flames at high-pressure*. 2006. SWISS FEDERAL INSTITUTE OF TECHNOLOGY ZURICH, PhD dissertation.
- [51] Peters, N., The turbulent burning velocity for small-scale and large-scale turbulence. J. Fluid Mech., 1999. 384: p. 107-132.
- [53] Tanahashi M., et al. "Simultaneous CH–OH PLIF and stereoscopic PIV measurements of turbulent premixed flames." *Proceedings of the Combustion Institute*, vol. 30, pp. 1665-72.
- [54] Frank J. H., et al. "Measurements of Conditional Velocities in Turbulent Premixed Flames by Simultaneous OH PLIF and PIV." *Department of Mechanical Engineering, The University of Sydney, Sydney, N.S.W.*, 2006.
- [55] Sadanandan, R., et al. "Simultaneous OH-PLIF and PIV measurements in a gas turbine model combustor." *Applied Physics B Lasers and Optics*, vol. 90, 2008, pp. 38-40.

- [56] Petersson P., et. al. "Simultaneous high-speed PIV and OH PLIF measurements and modal analysis for investigating flame-flow interaction in a low swirl flame." *16th Int Symp on Applications of Laser Techniques to Fluid Mechanics*, 2012.
- [57] Trunk, P. J., et. al. "Premixed flame propagation in turbulent flow by means of stereoscopic PIV and dual-plane OH-PLIF at sustained kHz repetition rates." *Proceedings of the Combustion Institute*, vol. 34, 2013, pp. 3565-72.
- [58] Hsu P. S., et. al. "Fiber-coupled, 10 kHz simultaneous OH planar laser-induced fluorescence/particle-image velocimetry." *Optics Letters*, vol. 38, no. 2, 15 Jan. 2013.
- [59] Daniele, S., et. al. "Flame front/turbulence interaction for syngas fuels in the thin reaction zones regime: turbulent and stretched laminar flame speeds at elevated pressures and temperatures." *J. Fluid Mech.*, vol. 724, 2013, pp. 36-68.
- [60] Boxx, I., et. al. "3 kHz PIV/OH-PLIF measurements in a gas turbine combustor at elevated pressure." *Proceedings of the Combustion Institute*, vol. 35, 2015, pp. 3793-802.
- [61] Coriton, B., et. al. "High-speed tomographic PIV and OH PLIF measurements in turbulent reactive flows." *Exp Fluids*, vol. 55, no. 1743, 2014.
- [62] Slabaugh, C., et. al. "Simultaneous 5 kHz OH-PLIF/PIV for the study of turbulent combustion at engine conditions." *Appl. Phys. B*, vol. 118, 2015, pp. 109-30.
- [63] Johchi A., et. al. "Investigation on rapid consumption of fine scale unburned mixture islands in turbulent flame via 10 kHz simultaneous CH-OH PLIF and SPIV." *Proceedings of the Combustion Institute*, vol. 35, 2015, pp. 3663-71.
- [64] Roque Ccacya, A.O., et. al. "Characterization of multi-jet turbulent flames in cross flow using stereo-PIV and OH-PLIF." *Fire Safety Journal*, vol. 78, 2015, pp. 44-54.

- [65] Elbaz, A.M., and Roberts W.L. "Experimental study of the inverse diffusion flame using high repetition rate OH/acetone PLIF and PIV." *Fuel*, vol. 165, 2016, pp. 447-61.
- [66] Choudhuri A. R., "Investigation on the Flame Extinction Limit of Fuel Blends", Combustion and Propulsion Research Laboratory, Mechanical and Industrial Engineering Department, The University of Texas at El Paso
- [67] James J. E. A., "Gas Dynamics", Pearson Prentice Hall, 2006
- [68] Cengel Y. A., "Heat and Mass Transfer", 3rd edition, McGraw Hill, 2006
- [69] "Thermal Expansion", www.rice.edu, accessed 2015
- [70] Melling, A., *Tracer particles and seeding for particle image velocimetry*. Meas. Sci. Technol., 1997. 8: p. 1406–1416.
- [71] Durst, F., Melling, A., Whitelaw, J.H., *Principles and practice of laser-doppler anemometry*. 1981: Academic Press, London.
- [72] Mercer, C., *Optical Metrology for Fluids, Combustion and Solids*. National Aeronautics and Space Administration Glenn Research Center. Kluwer Academic Publishers, 2003
- [73] Anisko, J. "AIAA Conference Paper" 44th AIAA Aerospace Sciences Meeting and Exhibit. Reno, Nevada, 2006
- [74] Dantec Dynamics, "DynamicStudios Manual", 2013
- [75] Hossain M.A. "*Design of a High Intensity Turbulent Combustion System*" 2015. The University of Texas at El Paso, Master of Science Thesis.

Vita

Martin Alejandro de la Torre was born in Cd. Juarez, Chihuahua, Mexico on September 6th 1987. Began enrollment at the University of Texas at El Paso in the Fall of 2006. He completed a Bachelor of Science in Mechanical Engineering in 2011 and a Master of Science in Mechanical Engineering in 2013. Martin has been working at the Center for Space Exploration and Technology Research (cSETR) since 2011 in a variety of projects, mostly regarding the combustion phenomena. He is expected to receive his Ph.D. In Mechanical Engineering from the University of Texas at El Paso in the Fall of 2016 semester. Upon graduation he hopes to continue contributing to the engineering community.

Permanent address: 6752 Brisa del Mar
El Paso, Texas, 79912

This thesis/dissertation was typed by Martin de la Torre.